SISSA/ISAS, International School for Advanced Studies
via Beirut 4 - 34014 Trieste - Italy

Dust and nebular emission in star forming galaxies

Thesis submitted for the degree of
"Doctor Philosophiæ"

In
Astrophysics

CANDIDATE

Pasquale Panuzzo

SUPERVISORS

Prof. L. Danese
Prof. A. Bressan
Prof. G. L. Granato

October 2003

Contents

Chapter 1

Introduction

New light in observational comology

The observational comology and the study of galaxy formation and evolution made a dramatic change in the last decade of the 20th century. The high spatial resolution of the Hubble Space Telescope, combined with the large collecting power of new 8-10 meters class telescopes, have stretched tenfold the redshift domain over which the stellar light of normal galaxies can be analyzed. As a result, nearly 90% of the cosmic time is now accessible to direct observation. Moreover, space missions like IRAS, ISO, Chandra or XMM-Newton (together with new ground-based instruments like SCUBA), enlarged our view to all spectral windows, showing an universe rich of extreme objects and very different from what observed in the optical.

On the other hand, many studies (from CMB measurements to cosmological supernovae) have stongly constrained the geometry of the universe. So, observational cosmology puts increasing emphasis today on the study of the intrinsic properties of galaxies and their evolution with look-back time. These developments pose new challanges to reserchers.

Theories of galaxy formation need not recur exclusively to examining the fossil record in nearby galaxies, but can be directly tested against observations of real galaxies at different cosmological epoch and at different wavelengths.

Resort to multiwavelength information is becoming critical, both to obtain diagnostics on a wide range of physical phenomena and to deal with the redshift displacement and/or dust obscuration of the rest-frame energy distributions of samples observed at different cosmic epochs.

In order to deal with information at all wavelengths, and to compare them with the different galaxy formation schemes, it is necessary to build spectrophotometrics models that can reproduce all the components that concur to the spectral energy distribution (SED) emitted by galaxies.

For this purpose, it was developed the spectrophotometric GRASIL code (Silva et al.,

1998) that accounts for almost all these components in a consistent and realistic way.

GRASIL has been shown to reproduce the UV to radio continuum SEDs of galaxies, at low and high redshift, and in different evolutionary stages (Silva et al., 1998; Franceschini et al., 1998; Rodighiero et al., 2000; Bressan et al., 2002), and to produce important results for galaxy formation (Granato et al., 2000; Granato et al., 2001; Magliocchetti et al., 2001; Granato et al., 2003).

In this work, we will concentrate only on two components of galaxies, namely the interstellar dust and the ionized gas, with more emphasis on the latter that was implemented in GRASIL during the PhD work.

The role of dust

The presence of interstellar dust was found in almost all galaxy types. Its radiative effects on stellar radiation heavely affect our view of galaxies: it absorbs and scatters photons, particularly at wavelength smaller than 1 μm, and returns the subtracted energy in form of infrared (IR) photons. In normal spiral galaxies about 1/3 of the bolometric luminosity is converted by dust in IR emission. The discovery by IRAS of powerful and highly dust enshrouded starbursts (Soifer et al., 1986), has underlined the necessity to model dust reprocessing of stellar radiation.

Growing evidence has been collected in the recent past showing that a physical understanding of dust effects in galaxies requires the inclusion of different environments, arranged in a rather complex geometry. A sophisticated treatment tends to become more and more important as the obscuration gets higher. Since stars are born in denser environments than average (the molecular clouds) and progressively become less obscured, the relative geometrical arrangement of dust and stars depends on the age of the star generation considered. Granato et al. (2000) have shown that this *age dependent extinction* can explain the differences between the observed attenuation law in normal and starburst galaxies.

The recent advances in the infrared and millimetric observational astronomy demand not only the extinction properties of the dust, but also, in a consistent way, its emission at longer wavelengths, to be considered.

Many models where presented in the past (from Guiderdoni & Rocca-Volmerange 1987 on) to compute the spectrophotometric evolution of galaxies in presence of dust. However, the complexity of the radiative transport has prevented many of them to have a comprehensive and coherent treatment of dust absorption, scattering and emission in a realistic geometry.

The main advantage of GRASIL with respect to previous treatments is that it already provides a sound treatment of all the aspects of dust reprocessing, since it makes use of a geometry which is much closer to reality. Dust modeling is thus related to real physical parameters, describing the different distributions of dust and stars in molecular complexes and diffuse components, and their age dependence.

A complete computation of dust reprocessing enable to constrain the dust effects and to derive the correct value of the star formation rate and/or the presence of AGN activity.

The nebular emission

Another important component that emits radiation in galaxies is the ionized gas. Photoionized clouds are ubiquitous and are produced by different mechanisms: star formation activity, SN driven shocks, planetary nebulae and AGNs.

Even if the total energy emitted by gas is small compared to the bolometic luminosity, this energy is concentrated in lines making the observation of such emission much easier. Furthermore, emission lines are present in all the spectral windows, from X-rays (the iron Kα line) to radio (high order hydrogen recombination lines).

The gas essentially converts the photons with $\lambda < 912$ Å into emission lines and continuum. The emission of ionized nebulae depends on two basic things: the physical properties of the gas (chemical composition, density) and the shape and luminosity of the ionizing flux. As a consequence, emission lines can be used to study many different astrophysical processes and media.

Anyhow, since our scientific interest is on the characterization of the star-forming galaxies, we will concentrate on nebular emission arising from massive stars, namely the H II regions. From this point of view, the two most important properties of nebular emission are the link with the star formation activity and the possibility to estimate the dust extinction.

The hydrogen recombination lines have been widely used as tracers of the current star formation rate (SFR), because of the direct proportionality between their intensity and the number of living massive stars. With respect to the other star formation estimators, as the UV luminosity, the radio emission or the dust emission, the nebular emission is a better estimator of the istantaneous SFR because ionizing photons are produced by massive stars with a lifetime shorter than stellar populations probed by other SFR estimators.

The almost constant ratio of Hα to Hβ intensity, predicted by nebular emission models for a large variety of environments (e.g. Osterbrock 1989), is a milestone in the interpretation of the effects of the intervening dust absorption (the Balmer decrement method). The method can be extended to other hydrogen recombination lines and provides a powerful method to estimate the extinction toward the star forming regions.

Emission lines are also excellent diagnostics for the gas properties. The gas density can be measured from the ratio of optical lines in doublets as [O II]3729/[O II]3726 or [S II]6716/[S II]6731 (Osterbrock, 1989), or with mid- and far-infrared lines (Rubin et al., 1994). More important, emission lines were widely used to estimate the abundance of several elements (see McGaugh 1991). The method is based on the ratio between the lines of the most important ions of the given element and an hydrogen recombination line.

The luminosity ratio is proportional to the element abundance, but as the metallicity grows, the temperature fall and the propotionality is no more in place after a critical value, depending on the chosen lines. It is worth noticing that for infrared lines the critical value is higher.

Furthermore, probing the spectral region under the Lyman break, nebular emission provide a unique diagnostic of processes that emit energy in this region, that is almost inaccessible to direct observation. A first simple application is to distinguish between the different ionizing sources. As a simple example, the high effective temperature ionizing flux in an AGN produce an ionized gas whose emission shows the presence of lines from highly ionized elements, like O IV, Ne V etc. that are not produced in nebulae excited by massive stars. Another interesting application, from our point of view, is the possibility to infere the IMF and the age of stellar populations from the ionization degree of suitable elements (see an application in Thornley et al. 2000). Infact, the different ionization thresholds of each element permit to estimate the number of photons with energies larger than these thresholds, constraining the shape of the ionizing flux and the stellar population that produce it.

Finally, the simple property of lines to be emitted at well determined wavelengths makes them a extremely usefull method to determine the redshift of the emitting galaxy or to estimate the velocity field inside it.

In star forming galaxies, nebular emission is produced by massive stars that are embedded in dusty environments, a feature that could limit their practical utility, if not properly treated. Thus, it is a natural goal to develop a method that treats nebular emission and dust reprocessing in the same coherent frame. We have therefore implemented the computation of nebular emission H II regions in the spectrophotometric code GRASIL.

In order to compute the nebular emission in GRASIL, we built a library of H II regions models. This library is indipendent from GRASIL and it was specifically designed to be used also in other population synthesis models. To this purpose we used a new approach that makes the library independent of the assumptions on stellar population spectra. The independence of these assumptions is a big advantage in respect to the few libraries of H II region models are already available in literature (Stasińska, 1990; García-Vargas et al., 1995a; García-Vargas et al., 1995b; Stasińska & Leitherer, 1996; Contini & Viegas, 2001).

The aim of this work

The contestual treatment of the reprocessing of stellar emission by dust and ionized gas allows to better constrain the action of both. In fact, from the dust emission SED is not easy to estimate the dust extinction toward star forming regions, because its luminosity depend mainly on the total amount of stellar radiation absorbed while the Balmer decrement method (possibly extended to near-IR hydrogen lines) provides strong constrains. On the other hand, the Balmer decrement method can be undermined by a different extinction toward different ionizing populations.

Our first aim was to determine the properties the attenuation in star forming galaxies, from normal spirals to UV-bright and IR luminous starbursts. Using our model to simulate optical emission lines, UV and IR luminosities we were able to give the right interpretation of several observations, remarking the importance of age selective extinction.

The possibility to use of different indicators, such as optical, near and mid infrared atomic emission lines, mid-infrared PAH bands, shape of the continuum from the far ultraviolet to the radio wavelengths, allows to obtain a fair picture of the star formation. It was thus possible to deal with several different SFR estimators, namely the UV, the emission lines, the IR and the radio luminosities. The second aim of this work is to provide the appropiate calibration for the above SFR estimators and to discuss their uncertinties rising from the different physical conditions encountered in star forming galaxies. This is particularly important when the SFR estimators are applied to distant galaxies.

Other applications presented here concernes the use of infrared lines to interpret the excitation diagrams of starbusts, to estimate the metallicity and to study high redshift galaxies.

The organization of the thesis

In **Chapter 2** we describe how we modelled the nebular emission produced by H II regions. We start with an introduction on the ionized gas physics and on the basic assumptions of the library. Then we describe of the adopted ionizing sources, the role of the ionizing parameter and the geometry of gas. We also discuss the accuracy and the limitations of the method and compare the results with observed H II galaxies

In **Chapter 3** we firstly summarize the main features of the GRASIL code and how galaxies are schematized in it. Then we introduce the method that we propose to correctly compute the nebular emission for a galaxy using the library described in the previous chapter, and compare the method to other models in literature.

In **Chapter 4** we apply the model to discuss several methods to estimate the attenuation in normal star forming galaxies by considering the UV, optical emission lines and FIR properties. In particular, we compare the attenuation suffered by the ionized gas with the one suffered by the stellar continuum. We show that observations require the extinction of different stellar populations to vary with age.

In **Chapter 5** we study the attenuation in starburst galaxies. In particular we examine the correlation between the FIR/UV ratio and the UV spectral index in the Wu et al. (2002) sample of starbursts. We also discuss the observed attenuation law and, by using our model, we explore its origin, and the effect of the age selective extinction. Furthermore we apply our model to explain some UV, FIR and optical properties of Very

Luminous IR galaxies.

Chapter 6 is dedicated to the measure of the star formation rate. We compare the different SFR estimators, namely the UV luminosity, the dust SED, the emission lines and the radio continuum. In the case of normal spiral galaxies, we provide our best calibrations for them and underline the different robustness of each estimator.

In **Chapter 7** we discuss some applications of IR nebular lines. In particular, we present a method to derive the metallicity of galaxies from IR nitrogen lines and radio emission. We also used the model to interpret the excitation diagram of galactic H II regions and starburst galaxies. Finally, we discuss the possibility to study the formation phase of elliptical galaxies with spectroscopical observations carried with SIRTF.

Appendix A collects some observational data extracted from the Wu et al. (2002) sample of starburst galaxies.

Chapter 2

Modelling nebular emission

In this chapter we describe how we modelled the nebular emission produced by H II regions. After a brief overview of the nebular emission physics in Sect. 2.1, Sect. 2.2 introduces the basic ideas of the model; Sect. 2.3 is dedicated to the adopted ionizing sources, while the role of the ionizing parameter and the geometry of gas is discussed in Sect. 2.4. The accuracy and the limitations of the method are discussed in Sect. 2.5 and Sect. 2.6; then, Sect. 2.7 faces the problem of dust inside H II regions. Sect. 2.8 summarizes how the H II region library was built and Sect. 2.9 compares the results with observed H II galaxies; finally, Sect. 2.10 describes the computation of continuum emission.

2.1 Introduction to nebular emission

Ionized gas emission is common in galaxies and is produced by different mechanisms: star formation activity, SN driven shocks, planetary nebulae and AGNs. In this work we will focus only on ionized gas associated by young massive stars (H II regions) because it is directly related to the star formation activity, while we do not consider broad and narrow line regions in AGNs because produced by accretion disks around massive black holes. We will also neglect nebular emission from:

- Shocks produced by SN explosions, because this contribution is very low (Kewley et al., 2001)
- Planetary nebulae excited by old star evolving toward the white dwarf phase, since their contribution to the total nebular emission is negligible (Binette et al., 1994) in presence of an even very modest star formation activity.
- Photo-dissociation regions and diffuse warm neutral/low-ionized medium, although some fine structure IR lines are efficiently produced in these media. As a consequence, the luminosity of such lines predicted by our model will be only lower limits; this issue is discussed in section 2.6.

The main energy input mechanism in H II regions is the photoionization of hydrogen by the ultraviolet radiation from stars within or near the nebulae. Photons with energy greater than H ionization potential (13.6 eV, corresponding to 911.76 Å) are absorbed and the excess energy is converted into kinetic energy of the photoelectrons. The following collisions between electrons, and between electrons and ions, redistribute this energy and give rise to several radiation emission processes.

When thermal electrons are recaptured by ions, the produced excited atoms (or ions) decay to lower levels via radiative transitions. This process is the origin of H, He I and He II recombination line spectra. The equilibrium between photoionization and recombination determines the degree of ionization of the gas.

Collisions between thermal electrons and ions excite ions from their ground energy levels. The radiative de-excitations from these levels have very small transition probabilities and collisional de-excitation can be efficient. If the density is lower than a critical value, collisional excitations lead to the emission of the so called forbidden lines[1].

Interactions between electrons and ions produce also continuum emission. Relevant processes for this emission are the recombination, the free-free (or bremsstrahlung) and the two-photon decay of Lyα photons. Continuum emission will be discussed in more detail in Sect. 2.10.

The complete treatment of photoionized nebulae is quite complex; the computation of the physical state and the emitted spectra of these objects must take into account the largest possible number of ions and electronic configurations, all the transitions between them, as well as charge transfer reactions, radiative transport and, possibly, molecule reactions and dust physics. To compute the nebular emission of H II regions in this work we used the widely known photoionization code *Cloudy* version 94 (Ferland, 2003). The code is open source and can be retrieved at the URL `http://www.nublado.org/`.

2.2 H II region model

The emission spectrum from a single H II region depends on two main ingredients: the SED of the ionizing star cluster and the properties of the excited gas. For a given stellar evolution scenario, the SED is determined by the IMF and the total mass, age and metallicity of the cluster, as well as by the adopted model atmospheres. On the other hand, the important properties of the excited gas are the density, the chemical composition and the geometry. In a galaxy the situation is more complicated and star forming regions possibly have different ages and different metallicities. In starbursts, star clusters of different ages and metallicities may coexist within the same star forming region.

---

[1] The name is due to the very low transition probability that makes them very difficult to be observed in laboratory experiments. The notation used to indicate these lines is with the ion name between squared brackets (i.e. [O II]3727)

To compute the line emission intensities, one should consider the spectrum of the ionizing source, provided by the recent star formation history, and use a photoionization code with suitable values of the gas parameters. To reduce the computing cost, one can use a pre-built library of line intensities, corresponding to different ages of the ionizing SSP and different metal contents of both the SSP and the gas. This still requires different libraries for different masses of the ionizing SSPs, assumed IMFs and model atmospheres. It becomes particularly time consuming in applications requiring a large number of models.

Our approach has been to pick out the physical parameters which actually affect the emission properties of H II regions. The analysis described in the following section shows that the emission line spectrum of an H II region with fixed gas properties (metallicity, density and geometry) is described with reasonable precision by only three quantities: the number of ionizing photons for H I, He I and O II ($Q_{\rm H}$, $Q_{\rm He}$, and $Q_{\rm O}$, defined in eq. 2.2). This method allows to get rid of the particular SSP model and IMF. In fact, different ionizing sources that provide the same values of $Q_{\rm H}$, $Q_{\rm He}$, and $Q_{\rm O}$, will produce the same emission line spectra, within a reasonable accuracy. The time evolution of these quantities is shown in Fig. 2.1 for SSPs of different metallicities.

Thus, we computed a library of photoionization models as a function of $Q_{\rm H}$, $Q_{\rm He}$, and $Q_{\rm O}$. When estimating the actual line emission due to a given stellar population, the spectrophotometric code computes $Q_{\rm H}$, $Q_{\rm He}$, and $Q_{\rm O}$ from the corresponding SED, and then interpolates the value from the above library.

In the following sections, we will describe in detail the adopted procedure and in sect. 2.5 we will discuss its accuracy.

2.3 Ionizing spectra

In order to have photoionization models as a function of $Q_{\rm H}$, $Q_{\rm He}$, and $Q_{\rm O}$, we used as ionizing SEDs piece-wise blackbodies, instead of SEDs derived from SSP spectra. In this way we can easily cover the space of Q parameters in a uniform way.

The Lyman continuum spectra of typical young stellar populations show two prominent discontinuities (see Fig. 2.2), at 504.1 Å and 227.8 Å , corresponding respectively to the ionizing energies for He I and He II (24.6 eV and 54.4 eV). At wavelengths smaller than 227.8 Å there are very few photons (Fig. 2.1, lower left panel, and Fig. 2.2). Between the Lyman break, He I break, and He II break, spectra can be reasonably well represented by blackbodies. Thus, when computing the libraries, we used the following functional representation of the ionizing SEDs:

$$F_\nu = \begin{cases} 0 & \text{for } \lambda < 227.8\text{Å} \\ A_{\rm He} B_\nu(T_{\rm He}) & \text{for } 227.8\text{Å} < \lambda < 504.1\text{Å} \\ A_{\rm H} B_\nu(T_{\rm H}) & \text{for } 504.1\text{Å} < \lambda < 911.76\text{Å} \\ A_{\rm ni} B_\nu(T_{\rm ni}) & \text{for } 911.76\text{Å} < \lambda \end{cases} \tag{2.1}$$

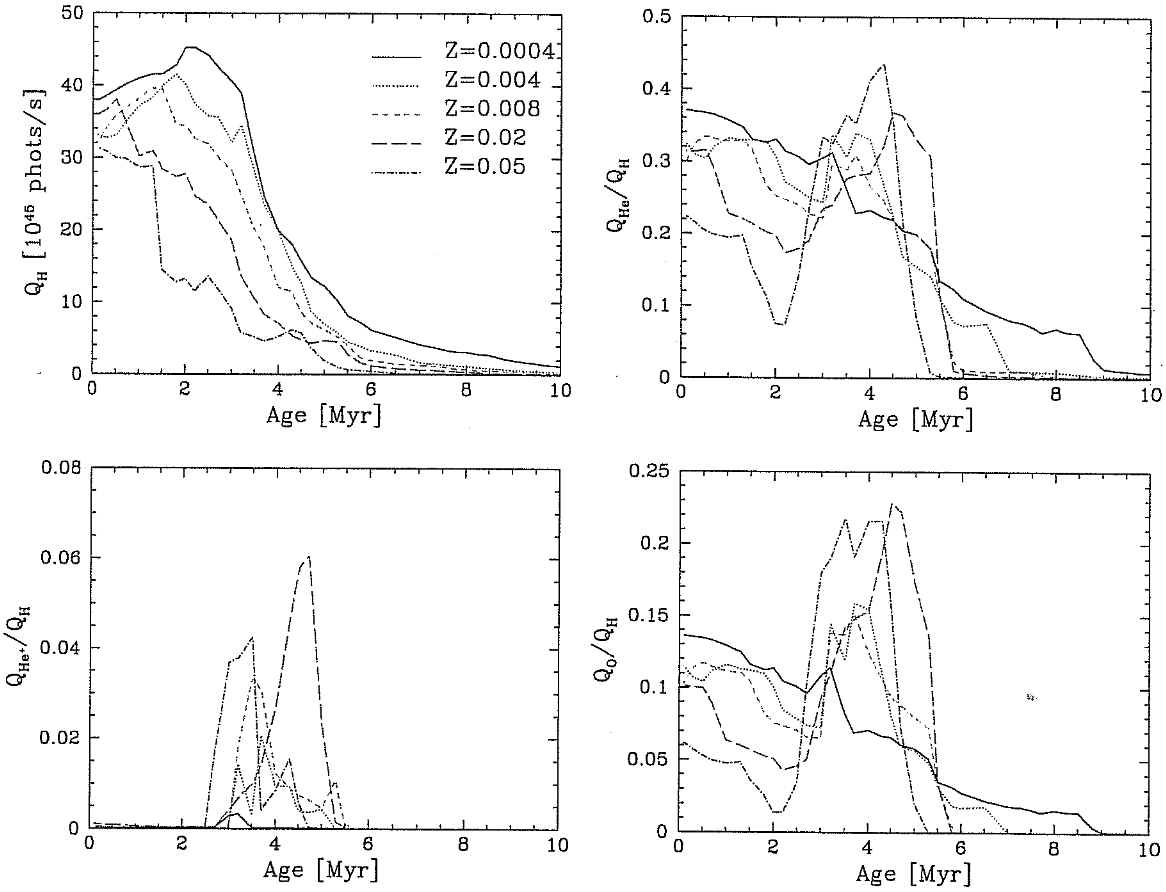

Figure 2.1: Time evolution of $Q_{\rm H}$ and the ratios $Q_{\rm He}/Q_{\rm H}$, $Q_{\rm He^+}/Q_{\rm H}$ and $Q_{\rm O}/Q_{\rm H}$ for SSPs of different metallicity. The assumed IMF is a Salpeter with $m_{\rm inf} = 0.15$ M$_\odot$ and $m_{\rm up} = 120$ M$_\odot$, normalized to 1 M$_\odot$.

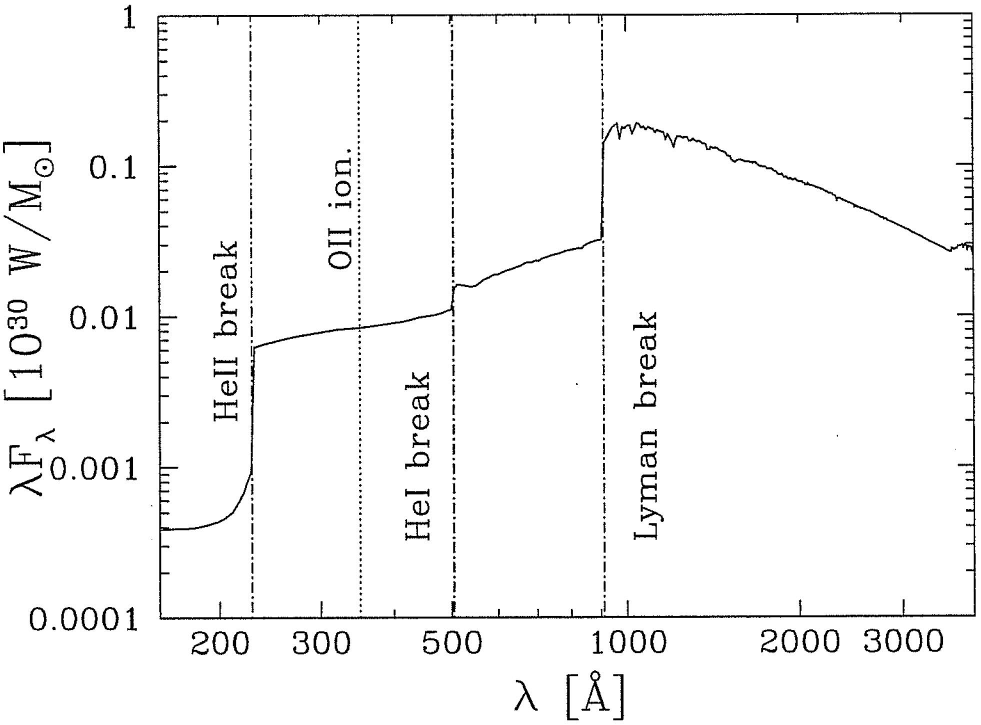

Figure 2.2: The SED of a typical young SSP (5 Myr old and Z=0.008). The dot-dashed vertical lines show the position of spectral discontinuities corresponding to the H, He I and He II ionizing energies (namely Lyman break, He I and He II break). The dotted line shows the position of O II ionizing energy.

where $B_\nu(T)$ is the Planck function at temperature T. This function depends on the 6 quantities $A_{\rm He}$, $T_{\rm He}$, $A_{\rm H}$, $T_{\rm H}$, $A_{\rm ni}$ and $T_{\rm ni}$. However, we found that the SEDs of young stellar populations can be well approximated by writing these 6 quantities in terms of only three parameters. These are the numbers of ionizing photons for H I, He I and O II ($Q_{\rm H}$, $Q_{\rm He}$, and $Q_{\rm O}$):

$$Q_{\rm H} = \int_{\nu_{\rm H}}^{\infty} \frac{F_\nu}{h\nu} d\nu \ , \ Q_{\rm He} = \int_{\nu_{\rm He}}^{\infty} \frac{F_\nu}{h\nu} d\nu \ , \ Q_{\rm O} = \int_{\nu_{\rm O}}^{\infty} \frac{F_\nu}{h\nu} d\nu \tag{2.2}$$

where $\nu_{\rm H}$, $\nu_{\rm He}$ and $\nu_{\rm O}$ are the photoionization threshold frequencies for respectively H I, He I, and O II (the latter corresponding to $\lambda_{\rm O} = 350.7$ Å).

$T_{\rm He}$ is implicitly given by:

$$\frac{\int_{\nu_{\rm O}}^{\infty} F_\nu {\rm d}\nu/h\nu}{\int_{\nu_{\rm He}}^{\infty} F_\nu {\rm d}\nu/h\nu} = \frac{\int_{\nu_{\rm O}}^{\nu_{\rm He^+}} B_\nu(T_{\rm He}) {\rm d}\nu/h\nu}{\int_{\nu_{\rm He}}^{\nu_{\rm He^+}} B_\nu(T_{\rm He}) {\rm d}\nu/h\nu} = \frac{Q_{\rm O}}{Q_{\rm He}} \tag{2.3}$$

where $\nu_{\rm He^+}$ is the photoionization threshold frequency for He II. Once $T_{\rm He}$ is known, $A_{\rm He}$ is obtained from

$$A_{\rm He} \int_{\nu_{\rm He}}^{\nu_{\rm He^+}} \frac{B_\nu(T_{\rm He})}{h\nu} d\nu = Q_{\rm He} \ . \tag{2.4}$$

Furthermore, to compute $T_{\rm H}$, we notice that there exists (for a wide range of age and metallicities) a correlation between $T_{\rm H}$ and $Q_{\rm He}/Q_{\rm H}$ of the SSP spectra, (Fig. 2.3):

$$T_{\rm H} = \begin{cases} 3 \cdot 10^4 + 4 \cdot 10^4 \frac{Q_{\rm He}}{Q_H} & \text{for } \frac{Q_{\rm He}}{Q_H} > 0.005 \\ 4 \cdot 10^4 + 0.5 \cdot 10^4 \cdot \log\left(\frac{Q_{\rm He}}{Q_{\rm H}}\right) & \text{for } \frac{Q_{\rm He}}{Q_{\rm H}} < 0.005 \end{cases} \tag{2.5}$$

We use this equation to derive $T_{\rm H}$ for given values of $Q_{\rm He}/Q_{\rm H}$. Then $A_{\rm H}$ follows from

$$A_{\rm H} \int_{\nu_{\rm H}}^{\nu_{\rm He}} \frac{B_\nu(T_{\rm H})}{h\nu} d\nu = Q_{\rm H} - Q_{\rm He} \ . \tag{2.6}$$

As for the values of $A_{\rm ni}$ and of the temperature $T_{\rm ni}$, it can be noted that the head of the Lyman region becomes important only for relatively low ionizing fluxes. We thus simply obtained their values after minimization of the differences between the lines computed with full SSPs spectra and analytical spectra:

$$T_{\rm ni} = \begin{cases} {\rm Max}(T_{\rm H}, 40000 \text{ K}) & \text{for } Q_{\rm He}/Q_{\rm H} > 0.005 \\ 30000 \text{ K} & \text{for } Q_{\rm He}/Q_{\rm H} < 0.005 \end{cases} \tag{2.7}$$

$$A_{\rm ni} = \begin{cases} 2.5 A_{\rm H} & \text{for } Q_{\rm He}/Q_{\rm H} > 0.005 \\ 3.5 A_{\rm H} & \text{for } Q_{\rm He}/Q_{\rm H} < 0.005 \end{cases} \tag{2.8}$$

In Fig. 2.4 we compare some SSP spectra with the corresponding analytical spectra. These comparisons suggest that analytical spectra can represent the Lyman continuum with reasonable precision. However, we stress that the goal is to get line emissions computed with analytical spectra which are as similar as possible to the ones computed with SSP. The accuracy of this method will be discussed in sec. 2.5.

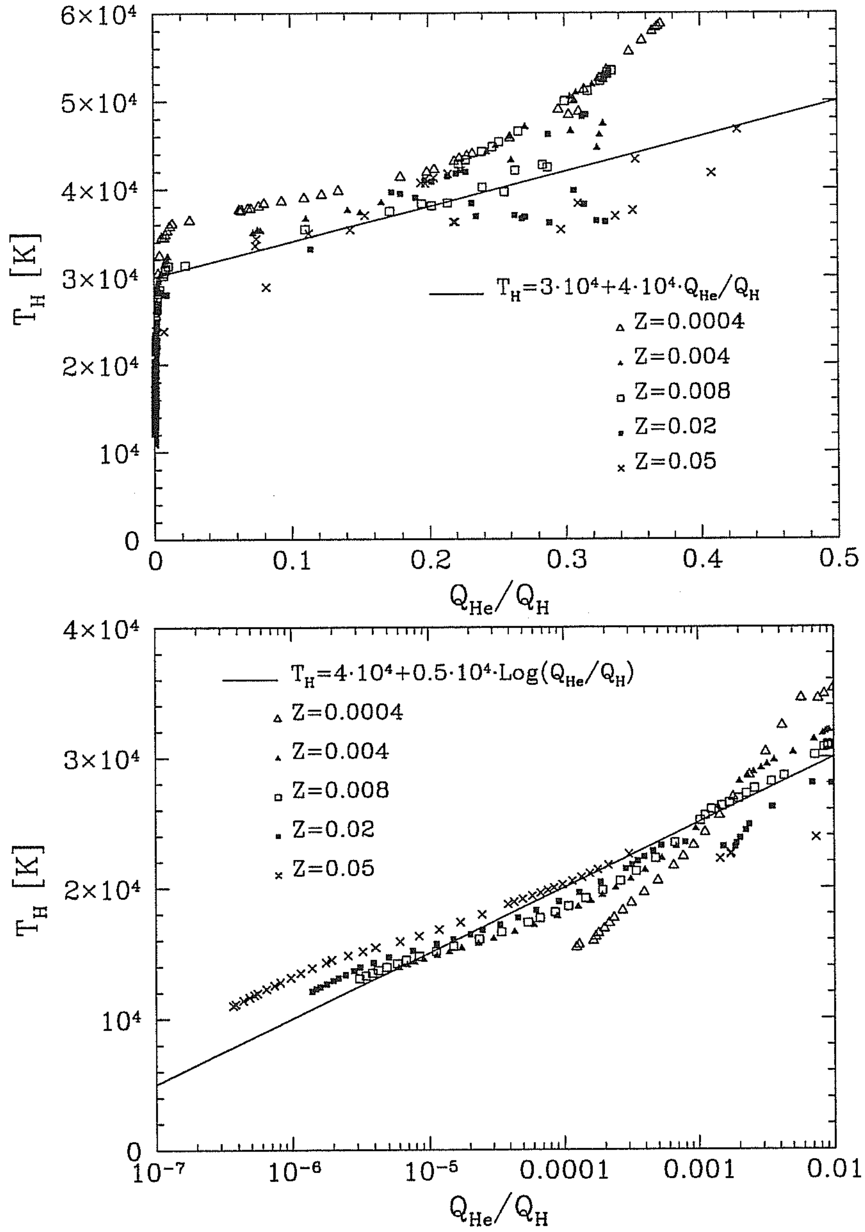

Figure 2.3: Temperature of ionizing continuum $T_{\rm H}$ as a function of $Q_{\rm He}/Q_{\rm H}$ for young SSPs of different ages (from 0.1 to 30 Myr) and metallicity (points). The lines refer to the analytical fit (eq. 2.5).

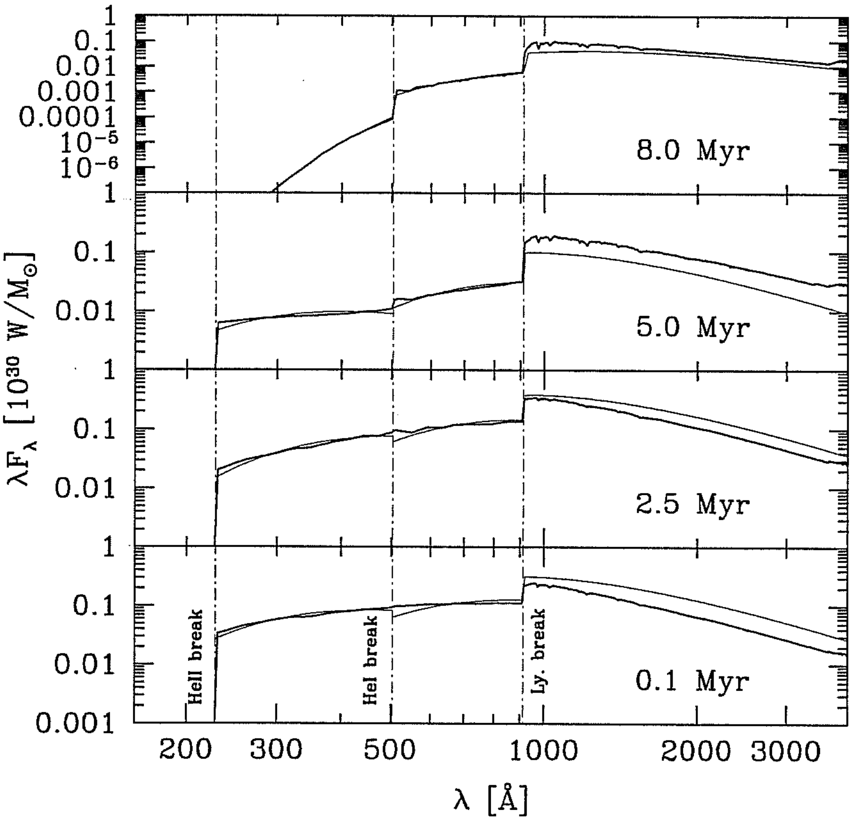

Figure 2.4: UV and ionizing spectra for SSPs (Z=0.008) of different ages (thick lines) compared with the corresponding analytical spectra (thin lines) that have the same Q values of the SSP spectra.

2.4 Geometry and the role of the ionization parameter

In our model, H II regions are assumed to be spherical and ionization bounded[2], with a constant density along the radius, and with a covering factor of 1. We considered different values of the filling factor (ϵ); when the filling factor is different from 1, the gas in the H II region is supposed to be divided in small clumps, and ϵ is defined as the ratio between the volume occupied by the clumps and the total volume of the H II region. The gas density is expressed in terms of hydrogen density (n_{H}) inside the clumps; note that n_{H} refers to atomic and ionized hydrogen (i.e. $n_{\mathrm{H}} = n_{\mathrm{H}^0} + n_{\mathrm{H}^+}$).

2.4.1 The definition of ionization parameter

It was shown that the emission properties of the ionized gas (i.e. the ratio of different line intensities) at a fixed chemical composition depends mainly on the number of ionizing photons that is available for each particle. In fact, the ionization equilibrium between different ionization states of an element is determined by the number of recombinations, that is proportional to the square of the density, and the number of photoionizations, that is proportional to the gas density and the number of photons. So, the ratio between photoionizations and recombinations is proportional to the number of photons per particle. This quantity is called ionization parameter U and is defined as:

$$U \equiv \frac{\#\text{ of photons in unit of volume}}{n_{\mathrm{H}}} \qquad (2.9)$$

It is easy to find that for a thin spherical shell at distance R from a central ionizing source emitting Q_{H} photons per second, the ionization parameter is $U = Q_{\mathrm{H}}/(4\pi R^2 c n_{\mathrm{H}})$, where c is the speed of light.

It is worth noticing that the emission do not depend directly on the geometrical configuration of the gas respect to the source, in the sense that two different geometries that have the same ionization parameter will produce emission properties very similar.

2.4.2 The volume averaged ionization parameter

It is convenient to define an volume averaged ionization parameter when considering a gas geometry in which U varies from point to point. This is needed to compare the emission properties of complex geometries in an effective way. Here we will define the appropriate

---

[2] The notation "ionization bounded" (or also radiation bounded) is commonly used refering to models in which the outer limit of the emission-line region is defined by the hydrogen ionization front. The opposite geometry in which the outer limit of the H II region correspond to the edge of the cloud is called "density bounded" or matter bounded.

ionization parameter for a spherical geometry, that is the shape of our simulated H II regions.

In the spherical geometry, the volume average $\langle U \rangle$ of ionization parameter is defined as:

$$\langle U \rangle = \int_0^{R_\mathrm{S}} \frac{U(r) 4\pi r^2 \mathrm{d}r}{\frac{4\pi}{3} R_\mathrm{S}^3} , \tag{2.10}$$

where R_S is the Strömgren radius and $U(r)$ is the ionization parameter of the gas at the distance r from the source. $U(r)$ is defined by:

$$U(r) = \frac{Q(r)}{4\pi r^2 n_\mathrm{H} c} , \tag{2.11}$$

with $Q(r)$ the number of ionizing photons per unit time that hit on the gas at the distance r. The variation of $Q(r)$ with the radius is given by the ionization/recombination equilibrium:

$$\frac{\mathrm{d}Q}{\mathrm{d}r} = -4\pi r^2 n_\mathrm{H}^2 \alpha_\mathrm{B}(\mathrm{H}) \epsilon , \tag{2.12}$$

where $\alpha_B(\mathrm{H})$ is the recombination coefficient of hydrogen in the case B. In the case B approximation one assumes that every photon produced by the direct recombination of H to its ground level (so that these photons have $\nu > \nu_\mathrm{H}$) is absorbed near the emission point (also called "on-the-spot" approximation). Integrating the previous equation we get:

$$Q(r) = Q_\mathrm{H} - \frac{4\pi}{3} r^3 n_\mathrm{H}^2 \alpha_\mathrm{B}(\mathrm{H}) \epsilon . \tag{2.13}$$

The Strömgren radius is defined as:

$$R_\mathrm{S} = \left(\frac{3 Q_\mathrm{H}}{4\pi n_\mathrm{H}^2 \alpha_\mathrm{B}(\mathrm{H}) \epsilon} \right)^{\frac{1}{3}} . \tag{2.14}$$

By substituting eqs. 2.13 and 2.14 in eq. 2.10, we get:

$$\begin{aligned} \langle U \rangle &= \int_0^{R_\mathrm{S}} \left(\frac{Q_\mathrm{H}}{4\pi r^2 n_\mathrm{H} c} - \frac{r n_\mathrm{H} \alpha_\mathrm{B}(\mathrm{H}) \epsilon}{3c} \right) \frac{3r^2 \mathrm{d}r}{R_\mathrm{S}^3} = \\ &= \frac{3Q_\mathrm{H}}{4\pi n_\mathrm{H} c} \left(\frac{4\pi n_\mathrm{H}^2 \alpha_\mathrm{B}(\mathrm{H}) \epsilon}{3 Q_\mathrm{H}} \right)^{\frac{2}{3}} - \frac{n_\mathrm{H} \alpha_\mathrm{B}(\mathrm{H}) \epsilon}{4c} \left(\frac{3 Q_\mathrm{H}}{4\pi n_\mathrm{H}^2 \alpha_\mathrm{B}(\mathrm{H}) \epsilon} \right)^{\frac{1}{3}} = \\ &= \frac{3}{4c} \left(\frac{3 Q_\mathrm{H} \alpha_\mathrm{B}^2(\mathrm{H}) n_\mathrm{H} \epsilon^2}{4\pi} \right)^{\frac{1}{3}} . \end{aligned} \tag{2.15}$$

Thus, in our geometry $\langle U \rangle$ is proportional to $(Q_\mathrm{H} n_\mathrm{H} \epsilon^2)^{1/3}$ while for the plane parallel geometry $U \propto Q_\mathrm{H}/n_\mathrm{H}$.

As said before, the results obtained assuming a spherical geometry remain also valid for different geometries and/or filling factors, provided the same value of $\langle U \rangle$ is maintained. To verify the validity of this assertion with an example, we compared the results

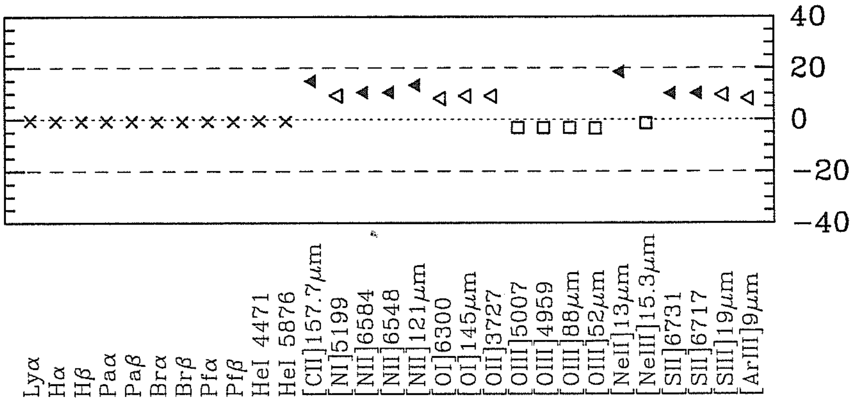

Figure 2.5: Differences between H II region models excited by a SSP spectrum with different geometries but same ionization parameter. Crosses are for difference smaller than 1%, empty squares for difference between 1% and 5%, empty triangles represent differences between 5% and 10%, and filled triangles represent differences greater than 10%. Gas and star metallicity is 0.008.

from a H II region with spherical geometry and one with in plane parallel geometry having the same ionization parameter.
We saw (Sect. 2.4.1) that for such shell shaped H II region the ionization parameter is given by $U = Q_{\mathrm{H}}/(4\pi R^2 n_{\mathrm{H}} c)$, where R is the radius of the shell. Imposing $U(R) = \langle U \rangle$, one can get the radius R of such equivalent shell shaped H II region that have the same ionization parameter of a spherical region. After some algebra:

$$R = \left(\frac{Q_{\mathrm{H}}}{9\pi n_{\mathrm{H}}^{2} \alpha_{\mathrm{B}} \epsilon} \right)^{\frac{1}{3}} \tag{2.16}$$

So, we computed the line spectra of a spherical H II region excited by a SSP of 0.1 Myr and with a stellar mass of 30000 $\mathrm{M}_{\odot}$, providing a ionizing flux $Q_{\mathrm{H}} = 9.567 \cdot 10^{50}$ photons/s, with a gas density $n_{\mathrm{H}} = 10$ cm^{-3} and a filling factor of one. Then, we compared its emission with the corresponding shell shaped H II region; which radius R is 164.55 pc (assuming a temperature of 10^4 K). The per cent differences in some line luminosities are reported in Fig. 2.5, and show that equation 2.15 gives a good estimation of the ionization parameter, and that H II regions with different geometries have a similar nebular emission if their ionization parameter is the same.

2.5 Accuracy

Before proceeding further we need to analyze the errors introduced by adopting the analytic SEDs (equation 2.1) instead of the SSP SEDs with the same Q values.

A first problem is that the analytical spectra neglect photons with energy higher than the He II ionization threshold (hereafter we will refer to these photons as high energy photons). This does not allow a realistic evaluation of the luminosity of the He II lines. However, nebular He II lines are superimposed to the generally more intense photospheric lines, emitted in the stellar atmospheres of WR stars (Conti, 1991; Schaerer et al., 1999). It is not possible to compute line intensities of highly ionized elements, such as O IV or Ne IV. These lines are typically either not observed, or very faint in pure star forming galaxies, so that they are often interpreted as a signature of AGN activity. The impact on other lines of neglecting high energy photons is quantified by comparing the calculated emission of H II regions excited by SSP spectra with and without high energy photons, normalized in order to have the same $Q_{\rm H}$. The results (for some ages and metallicities) are shown in Fig. 2.6 for a Salpeter IMF between 0.15 and 120 $M_\odot$. The difference in the two cases is always $< 10\%$, and typically $< 1\%$; the highest difference appears at SSP ages at which the WR stars produce their maximum flux in high energy photons. We conclude that the lack of high energy photons is not very important, at least for the lines considered here.

The comparison between line intensities of H II region models excited by an SSP spectrum and those excited by a parametric spectrum with the same values of $Q_{\rm H}$, $Q_{\rm He}$, and $Q_{\rm O}$ is shown in Fig. 2.7. Typical differences in the emission lines are lower than 10%, with the larger ones arising at lower values of $Q_{\rm H}$, i.e. older ages. Most of them are due to discrepancies between the SSP and parametric SEDs at wavelengths longer than the Lyman break. Indeed, photons with wavelengths corresponding to Lyman series lines can be efficiently absorbed and re-emitted in optical lines. When the ionizing flux decreases with respect to the non-ionizing one, this effect can be important. Notice however that, when computing the lines emitted by a combination of H II regions excited by clusters with different ages, the most important contribution arises from the youngest populations.

As noticed in previous works (see e.g. Stasińska et al. 2001 or Rubin et al. 2001), the photo-ionization models cannot be accurate when the gas metallicity exceeds the solar value, for several reasons. As the metallicity increases, fine structure infrared lines of metals (that depend little on temperature) dominate the cooling processes, but their transition probabilities have not yet been well determined. On the other hand, optical collisionally excited lines, that depend strongly on the electronic temperature, become uncertain because the temperature is regulated by infrared lines. Furthermore, the thermal instability of the gas affects the line intensity when the temperature is low and the metallicity is high. Finally, a further source of uncertainty at high metallicity is due to the poorly known depletion of metals onto dust grains. To minimize this problem, we used a set of abundances measured by McGaugh (1991) in the gas phase.

In order to check the flexibility of our procedure, we compared in Fig. 2.8 the results obtained by repeating the above test when adopting a very different IMF, namely a top heavy modified Kennicutt's IMF ($d\log N/d\log m = -0.4$ for 0.15 $M_\odot < m < 1$ $M_\odot$ and $d\log N/d\log m = -1$ for 1 $M_\odot < m <$ 120 $M_\odot$). The differences between H II region models excited by SSP spectra and analytical ones with the same Q values are not larger than in the case of the Salpeter IMF, despite the very different slope of the IMF.

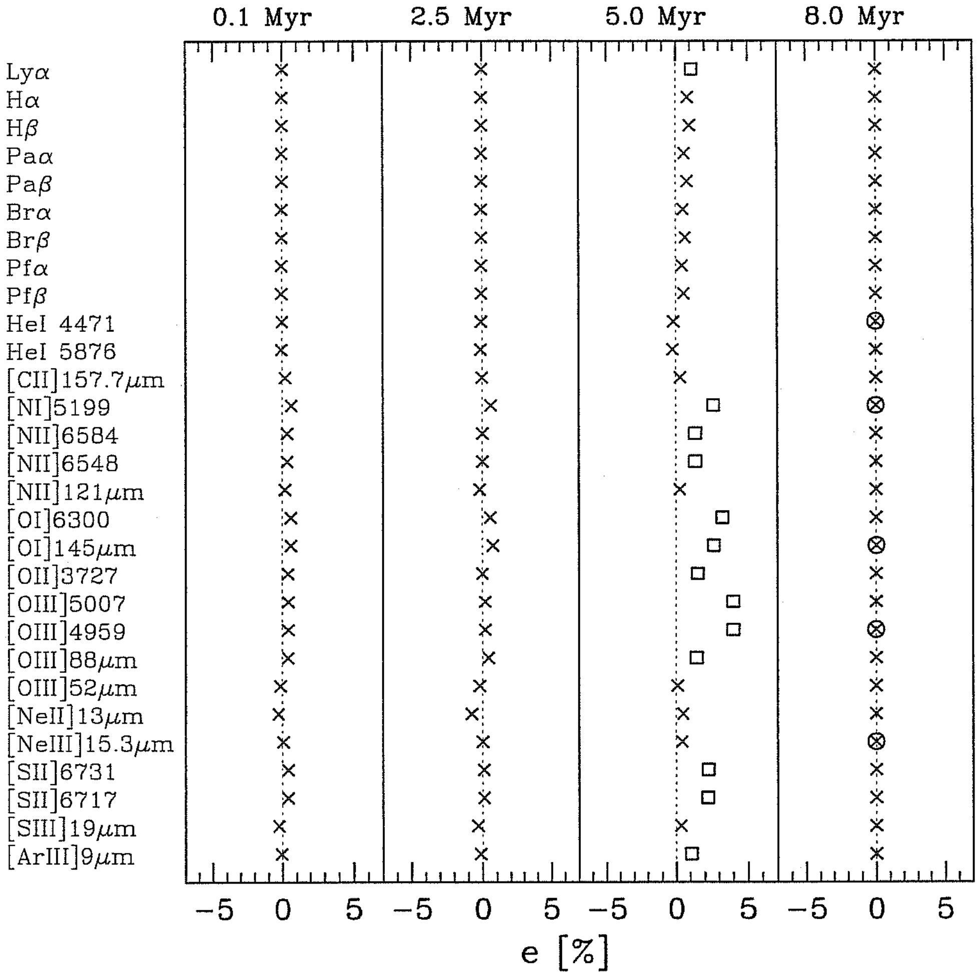

Figure 2.6: Differences between H II region models excited by SSP spectra with and without high energy photons. Crosses are for difference smaller than 1%, empty squares for difference between 1% and 5%; circled symbols refer to very low luminosity lines. Gas and star metallicity is 0.008.

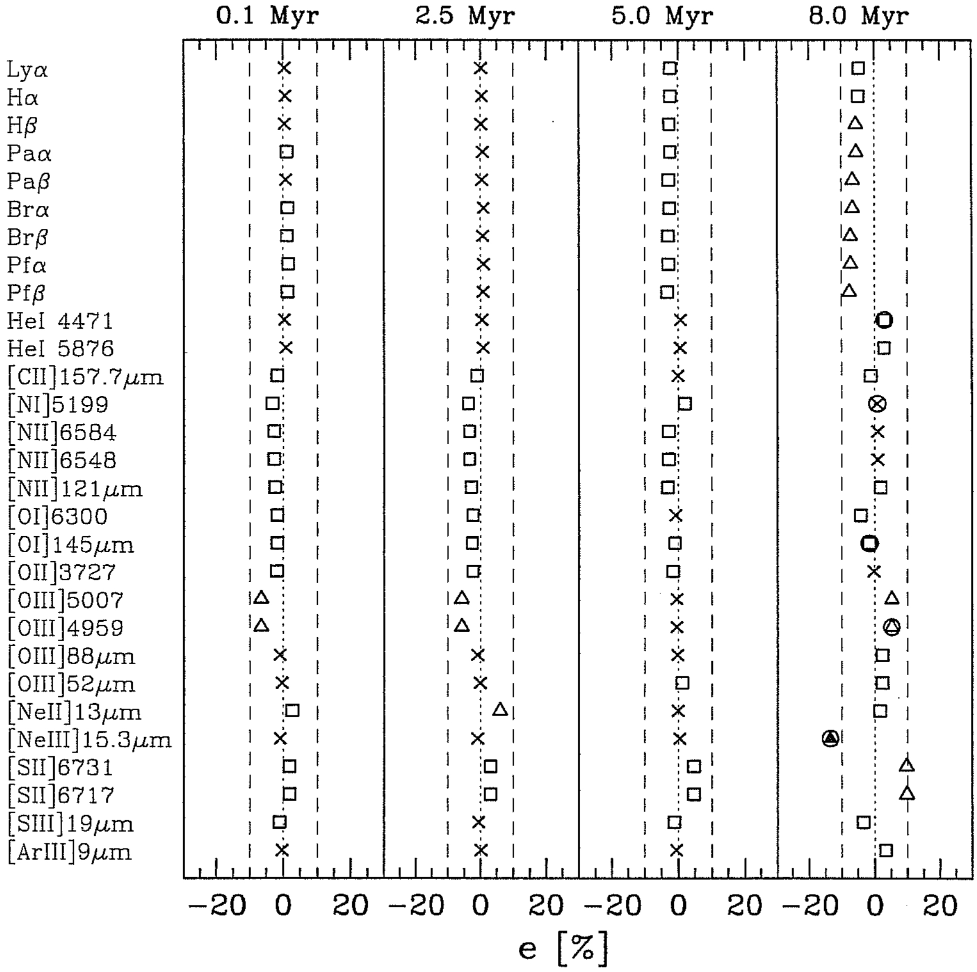

Figure 2.7: Differences between H II region models excited by SSP spectra and parametric spectra with the same Qs. Empty triangles represent differences between 5% and 10%, filled triangles represent differences greater than 10%.

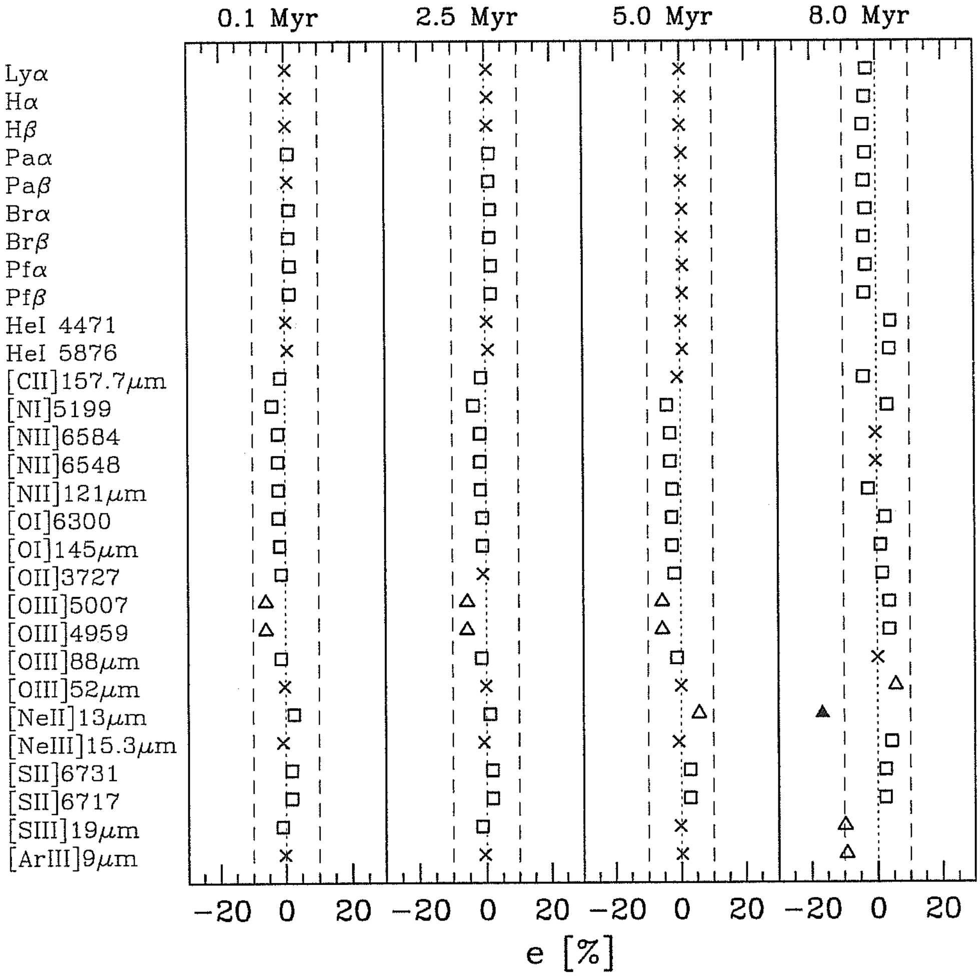

Figure 2.8: As Fig. 2.7, but with SSPs with a top heavy modified Kennicutt's IMF.

In conclusion, the presented analytical spectra can reproduce with a good accuracy the nebular emission properties of H II regions excited by star clusters with different IMF, age and metallicity by only making use of the three quantities $Q_{\rm H}$, $Q_{\rm He}$, and $Q_{\rm O}$. Obviously this accuracy could be improved by adding some other quantity to describe the SED with more details, but this would dramatically increase the number of H II region models used for the library.

2.6 C and O infrared lines

C I, C II and O I fine structure infrared lines are produced not only in H II regions, but also in diffuse warm neutral/low-ionized interstellar medium and photodissociation regions (PDR). The energy difference between the ground level and the collisionally excited level are quite low. For instance, these energies correspond to temperatures of 228 K, 326 K, 62.5 K and 23.6 K ($1.96 \cdot 10^{-2}$ eV, $2.81 \cdot 10^{-2}$ eV, $5.38 \cdot 10^{-3}$ eV and $2.03 \cdot 10^{-3}$ eV), respectively for [O I] 63.2μm and 145.5μm, [C I]369μm and 610μm (Kaufman et al., 1999). Such temperatures are smaller than the typical one of the neutral medium, so that these lines can easily be produced in the neutral ISM.

Because carbon has a ionization potential (11.26 eV) which is lower than H, the C II ion is present in PDR and in neutral medium illuminated by far UV stellar radiation. Indeed, the [C II]157.7μm line is the most important coolant of warm neutral medium. The relative contribution of different media to these lines is still a matter of debate (Heiles, 1994; Malhotra et al., 2001). Since our model does not include PDR or neutral gas emission, the luminosities predicted for these lines must be taken as a lower limit.

2.7 Dust inside H II regions

The presence of dust inside H II regions is established as a fact but the characteristics of dust and its effects on the emerging emission are still poorly known.

Dust can be destroyed by the intense UV radiation in this environment, but the survived fraction is inevitably important. Dust is involved in many processes inside the ionized gas (electric charge and thermal energy exchange with gas; molecular reactions in the outer regions), however the main effect is its interaction with the radiation field.

In fact, dust can absorb a fraction of the ionizing flux so that the total nebular emission of the H II region is smaller than in the dust-free case. DeGioia-Eastwood (1992) estimated that the typical fraction of ionizing photons absorbed by dust is around 30%. However, it is clear that this fraction depends on the optical properties of dust grains, on their distribution inside the region and in respect to the ionized gas. Furthermore, the intense UV field and the shocks change their distribution of dimensions by sublimation of smaller grains and collisions between them. Th above effects render our knowledge of physical properties of dust in this environments very uncertain.

Though *Cloudy* gives the possibility to account for the presence of internal dust, the choice of a dust model is arbitrary. This will:

- Introduce new free parameters (the distribution of grain dimension, the grain composition etc.).
- The computed models could be coherently used only in some specific cases.
- The independence of results from the gas geometry discussed in sect.2.4 would not be valid anymore.

An approximate solution to this problem is to compute models without internal dust and to decrease the obtained nebular emission by the fraction $f_{\rm d}$ of ionizing photons absorbed by dust. This solution is crude and does not take in to account the wavelength dependence of dust absorption but greatly simplify the problem while a more detailed solution would introduce many uncertainties. Thus, absorption by internal dust has not been considered in the H II region models presented here and the obtained emission must be multiplied by a factor $1 - f_{\rm d}$.

2.7.1 The resonant Lyα line

For the Lyα line, the situation is different since its photons can be efficiently absorbed by hydrogen atoms in the ground energy level. The absorbed photons are promptly re-emitted at the same wavelength (but in an random direction) or can decay via the emission of two photons (that provides a continuum emission). Thus, Lyα photons follow a random walk through the nebulae to escape, considerably increasing their probability to be degraded in two-photon continuum emission or to be absorbed by dust. In galaxies with normal dust content, almost all the photons in the resonant Lyα line are reprocessed via two-photon decay and dust absorption (with the consequent thermal re-emission) (Osterbrock, 1989). The contribution to the IR luminosity by absorbed Lyα photons is at most $\leq 7\%$ of the bolometric luminosity. It is worth noticing that, in the case of very low dust content, this can constitute a significant fraction of the total IR luminosity. However, winds and outflows strongly reduce the resonant scattering and a detailed treatment of the Lyα transfer in presence of these processes.

The H II region library presented in this work provides a luminosity of Lyα which do not account for the above described processes and we do not further consider this line in our applications.

2.8 The library

With the relationships described in Sect. 2.3, we built a library for a grid of values of $Q_{\rm H}$, $Q_{\rm He}$, and $Q_{\rm O}$, and for different assumptions on the gas density, metallicity and

Table 2.1: Adopted abundances, from McGaugh (1991). a) For $Z/Z_\odot < 0.1175$ b) For $Z/Z_\odot > 0.1175$.

El.	Abundance	El.	Abundance
He	$0.0772{+}0.012765 \cdot Z/Z_\odot$	Al	$3.40\text{e-}6 \cdot Z/Z_\odot$
C^a	$6.59\text{e-}6 \cdot (Z/Z_\odot)^{0.3}$	Si	$4.43\text{e-}6 \cdot Z/Z_\odot$
C^b	$3.70\text{e-}4 \cdot (Z/Z_\odot)^{2.17}$	S	$2.13\text{e-}5 \cdot Z/Z_\odot$
N	$6.21\text{e-}5 \cdot (Z/Z_\odot)^{1.5}$	Ar	$5.96\text{e-}6 \cdot Z/Z_\odot$
O	$8.51\text{e-}4 \cdot Z/Z_\odot$	Fe^a	$1.88\text{e-}6 \cdot (Z/Z_\odot)^{1.35}$
Ne	$1.70\text{e-}4 \cdot Z/Z_\odot$	Fe^b	$1.09\text{e-}5 \cdot (Z/Z_\odot)^{2.17}$
Mg	$4.25\text{e-}5 \cdot Z/Z_\odot$		

Table 2.2: Values of parameters used in the H II regions library.

Z_{gas}	0.0008, 0.004, 0.008, 0.015, 0.02, 0.03, 0.04, 0.05
n_H	10, 30, 100, 300, 1000, 3000, 10^4 cm^{-3}
ϵ	0.001, 0.01, 0.1, 1.0
Q_H	10^{46} — 10^{52} phot/s in 31 logarithmic steps
Q_{He}/Q_H (grid 1)	0.05, 0.10625, 0.1625, 0.21875, 0.275, 0.33125, 0.3875, 0.44375, 0.5
Q_O/Q_{He} (grid 1)	0.13, 0.23, 0.33, 0.43, 0.53, 0.63
Q_{He}/Q_H (grid 2)	0.05, 0.025, 0.01, 0.005, 0.0025, 0.0001, 0.
Q_O/Q_{He} (grid 2)	0.0, 0.1, 0.2, 0.3, 0.4

filling factor (ϵ). H II regions are assumed to be spherical and ionization bounded, with a constant density along the radius, and with a covering factor of 1. The abundance of elements respect to H are from McGaugh (1991) and are shown in Table 2.1. These abundances are relative to gas phase, thus they already account for the fraction stored in dust (depletion).

The space of Qs parameter is divided into two grids, identified by a grid index, to follow better the broad correlation between Q_{He}/Q_H and Q_O/Q_{He}. In the first grid, with index number equal 1, $Q_{He}/Q_H > 0.05$; in the second (grid index = 2) $Q_{He}/Q_H < 0.05$. The space of parameters covered by the models is shown in Table 2.2.

We computed 48 H recombination lines, 6 He recombination lines and 60 lines of other elements; the complete list is reported in Table 2.3 and 2.4.

The total number of computed H II region models is 463512, that needed around 3 year of CPU time. The H II region library can be freely retrieved through the web at the URL `http://www.sissa.it/~panuzzo/hii/`.

Our library was specifically designed to be used in population synthesis models. To this purpose we device a new approach that makes the library independent of assumptions on SSP spectra. In fact, with our parametrization in terms of Q_H, Q_{He} and Q_O the method presented is independent of the IMF, the stellar atmosphere models and stellar evolutionary tracks.

Table 2.3: Hydrogen recombination lines computed in the library and their wavelengths. Line wavelengths are taken from the Atomic Line List by P. van Hoof at University of Kentucky (URL: `http://www.pa.uky.edu/~peter/atomic/`).

Name	λ [Å]	Name	λ [Å]	Name	λ [Å]	Name	λ [Å]
Lyα	1215.67	Lyβ	1025.72	Lyγ	972.54	Lyδ	949.74
Lyϵ	937.80	Lyζ	930.75	Lyη	926.23	Lyθ	923.15
Hα	6564.61	Hβ	4862.68	Hγ	4341.68	Hδ	4102.89
Hϵ	3971.20	Hζ	3890.15	Hη	3836.47	Hθ	3798.98
Paα	18756.13	Paβ	12821.59	Paγ	10941.09	Paδ	10052.13
Paϵ	9548.59	Paζ	9231.55	Paη	9017.38	Paθ	8865.22
Brα	40522.62	Brβ	26258.67	Brγ	21661.20	Brδ	19450.87
Brϵ	18179.08	Brζ	17366.85	Brη	16811.11	Brθ	16411.67
Pfα	74598.58	Pfβ	46537.78	Pfγ	37405.57	Pfδ	32969.92
Pfϵ	30392.02	Pfζ	28729.96	Pfη	27582.68	Pfθ	26751.31
Huα	123718.98	Huβ	75024.93	Huγ	59082.13	Huδ	51286.57
Huϵ	46725.09	Huζ	43764.54	Huη	41707.94	Huθ	40208.67

The independence of these assumptions is a big advantage in respect to the few libraries of H II region models are already available in existing literature (Stasińska, 1990; García-Vargas et al., 1995a; García-Vargas et al., 1995b; Stasińska & Leitherer, 1996; Contini & Viegas, 2001). In fact, the stellar atmosphere models have still room to be improved, and the IMF is still a poorly known issue.

2.9 Comparison with observed H II galaxies

We compare the H II library with observations of a sample of H II galaxies (crosses) from Dessauges-Zavadsky et al. (2000), a revision of the Terlevich's catalog (Terlevich et al., 1991). H II galaxies have spectra very similar to those of H II regions because usually dominated by a large central H II region and are interpreted as bursting dwarf galaxies. Furthermore, these objects span a wide range in metallicity and other parameters. This make the sample very convenient for the comparison with the models. In figure 2.9 we show a typical diagnostic diagram (Log([O III]/Hβ) vs. Log([S II]/Hα)) used to analyze the excitation of H II galaxies. We reported on it the position of observed H II galaxies (crosses) from Dessauges-Zavadsky et al. (2000) and the separation line between the region occupied by H II galaxies (on the left) from the AGN region, as empirically defined by Veilleux & Osterbrock (1987) (thick long dashed line); the thick dot-dashed line delineates the same separation computed by Kewley et al. (2001).

We show in the same figure the separate dependence of models on $\langle U \rangle$ (or $Q_{\rm H}$ via the equation 2.15) and on the hardness of the ionizing SED, expressed by $Q_{\rm He}/Q_{\rm H}$ and $Q_{\rm O}/Q_{\rm He}$.

We notice that the library covers the region of diagnostic diagrams populated by

Table 2.4: Helium and heavier element lines computed in the library. Lines with an * are multipets for which the library provides the total luminosity; a mean reference wavelength is reported for these lines.

Name	λ [Å]	Name	λ [Å]
He I4472	4472.75*	He I5877	5877.3*
He I6680	6680.00	He I10833	10833.0*
He I3889	3889.74*	He I7065	7067.3*
[C I]9850	9852.96	[C I]8727	8729.52
[C I]4621	4622.86	[C I]610μm	610.0μm
[C I]370μm	370.4μm	[C II]157.7μm	157.68μm
C II]2326	2326.0*	[N I]5200	5200.35*
[N I]3467	3467.51*	[N I]10405	10405.51*
[N II]6585	6585.28	[N II]6549	6549.85
[N II]5756	5756.24	[N II]122μm	121.76μm
[N II]205μm	205.5μm	N II]2141	2141
[N III]57μm	57.34μm	[O I]6302	6302.05
[O I]6365	6365.54	[O I]5578	5578.89
[O I]63μm	63.185μm	[O I]145μm	145.535μm
[O II]3727	3728.5*	[O II]7327	7326.8*
[O II]2471	2471.0*	O III]1663	1663.0*
[O III]5007	5008.24	[O III]4960	4960.29
[O III]4364	4364.44	[O III]2321	2321.66
[O III]88μm	88.356μm	[O III]52μm	51.814μm
[Ne II]12.8μm	12.814μm	[Ne III]15.5μm	15.555μm
[Ne III]36μm	36.013μm	[Ne III]3870	3870.16
[Ne III]3968	3968.91	[Ne III]3343	3343.50
[Ne III]1815	1814.73	Mg II2800	2800.0
[Si II]35μm	34.815μm	[S II]10331	10331.4*
[S II]6732	6732.67	[S II]6717	6718.29
[S II]4070	4069.75	[S II]4078	4077.50
[S III]18.7μm	18.713μm	[S III]33.5μm	33.481μm
[S III]9533	9533.2	[S III]9071	9071.1
[S III]6314	6313.8	[S III]3723	3722.69
[S IV]10.5μm	10.510μm	[Ar II]7μm	6.985μm
[Ar III]7138	7137.8	[Ar III]7753	7753.2
[Ar III]5193	5193.27	[Ar III]3110	3110.08
[Ar III]22μm	21.829μm	[Ar III]9μm	8.991μm

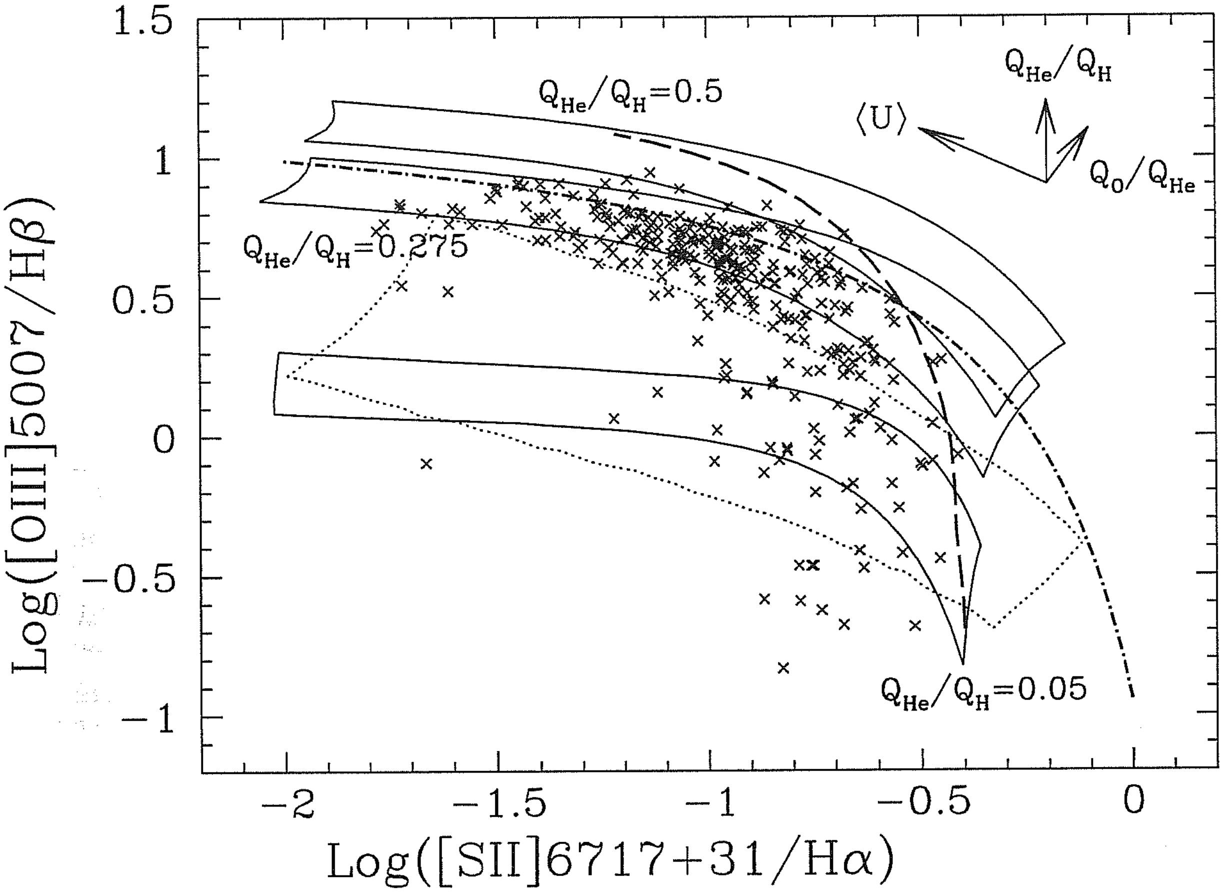

Figure 2.9: Diagnostic diagram Log([O III]/Hβ) vs. Log([S II]/Hα). Crosses are observed H II galaxies from Dessauges-Zavadsky et al. (2000). The three solid closed lines show the regions occupied by H II region models from our library with three values of $Q_{\rm He}/Q_{\rm H}$ (0.5, 0.275 and 0.05). The arrows show shifts at increasing $\langle U \rangle$, $Q_{\rm He}/Q_{\rm H}$, or $Q_{\rm O}/Q_{\rm He}$. Log($\langle U \rangle$) ranges from -0.867 to -3.534, and $Q_{\rm O}/Q_{\rm He}$ from 0.13 to 0.63. The models have a gas metallicity of 0.004, while the closed dotted line shows the position of models with solar metallicity and $Q_{\rm He}/Q_{\rm H}$ = 0.275. All the models have a hydrogen density of 10 cm^{-3}. The thick long dashed line separates the region occupied by H II galaxies (on the left) from the AGN region as defined by Veilleux & Osterbrock (1987) while the thick dot-dashed line delineates the same separation computed by Kewley et al. (2001).

observed H II galaxies. Some our models fall in the region of the diagnostic diagrams occupied by AGNs; these models are produced by the hardest spectra in the library ($Q_{\mathrm{He}}/Q_{\mathrm{H}} \simeq 0.5$) that are harder than the spectra that can be built with true SSP.

2.10 Nebular continuum emission

We have evaluated the nebular continuum emission using the Strömgren theory for the case B approximation (see Osterbrock, 1989) and added to the emerging spectrum.

To this purpose we consider the H II region as composed by hydrogen and helium only. Furthermore, since massive stars produce very few photons with $h\nu > 54.4$ eV, we consider neutral and singly ionized helium.

Photons with energies 13.6 eV $< h\nu <$ 24.6 eV can only ionize hydrogen, while photons with higher energies can ionize both H and He. Thus, the ionization structure of an H II region consists of a central H^+, He^+ zone surrounded by a H^+, He^0 region. As the ratio $Q_{\mathrm{He}}/Q_{\mathrm{H}}$ of the ionizing source increases, the outer boundary of the central zone increases and eventually the He^0 region becomes very thin.

To obtain the ionization structure of the nebula we use the ionization equations (obtained imposing the equilibrium between photoionizations and recombinations) for the H and He. Even adopting the on-the-spot approximation (or case B approx.), we must consider explicitly the coupling of H and He ionization in the spectral region above 24.6 eV, and that the recombinations to the ground level of He can ionize either H or He. To proceed, let us call y the fraction of photons emitted by He recombining to the ground level that are absorbed by hydrogen, and p the probability that a He recombination produce an ionizing photon. The ionization equations become (Osterbrock, 1989) (in the on-the-spot approximation):

$$\begin{aligned} \frac{n_{\mathrm{H}^0}}{4\pi r^2}\int_{\nu_{\mathrm{H}}}^{\infty}\frac{F_\nu}{h\nu}a_\nu(\mathrm{H})\mathrm{e}^{-\tau_\nu}\mathrm{d}\nu + y n_{\mathrm{He}^+} n_{\mathrm{e}}\alpha_1(\mathrm{He},T) & + \\ + p n_{\mathrm{He}^+} n_{\mathrm{e}}\alpha_{\mathrm{B}}(\mathrm{He},T) & = n_{\mathrm{H}^+} n_{\mathrm{e}}\alpha_{\mathrm{B}}(\mathrm{H},T) \end{aligned} \tag{2.17}$$

and

$$\frac{n_{\mathrm{He}^0}}{4\pi r^2}\int_{\nu_{\mathrm{He}}}^{\infty}\frac{F_\nu}{h\nu}a_\nu(\mathrm{He}^0)\mathrm{e}^{-\tau_\nu}\mathrm{d}\nu + (1-y) n_{\mathrm{He}^+} n_{\mathrm{e}}\alpha_1(\mathrm{He},T) = n_{\mathrm{He}^+} n_{\mathrm{e}}\alpha_{\mathrm{B}}(\mathrm{H},T) \tag{2.18}$$

where $a_\nu(\mathrm{H})$ and $a_\nu(\mathrm{He})$ are the photoionization absorption cross section of H and He respectively. τ_ν is the optical depth for photoionization absorption and it is given by the equation

$$\frac{\mathrm{d}\tau_\nu}{\mathrm{d}r} = \begin{cases} n_{\mathrm{H}^0}a_\nu(\mathrm{H}) & \text{for} \quad \nu_{\mathrm{H}} < \nu < \nu_{\mathrm{He}} \\ n_{\mathrm{H}^0}a_\nu(\mathrm{H}) + n_{\mathrm{He}^0}a_\nu(\mathrm{He}) & \text{for} \quad \nu_{\mathrm{He}} < \nu \end{cases} \tag{2.19}$$

Finally, we impose that $n_{\mathrm{e}} = n_{\mathrm{H}^+} + n_{\mathrm{He}^+}$.

The previous equations could be solved numerically to compute the size of H^+ and He^+ zones, but the approximate dimension can be found by ignoring the absorption by H in the He^+ zone. This corresponds to setting $y = 0$ in equation 2.17 and 2.18 and $n_{H^0} = 0$ in the second case of equation 2.19. Integrating eq. 2.18 over the radius and using eq. 2.19, after some algebra, it can be found:

$$Q_{\rm He} = \frac{4\pi}{3} R_{\rm He}^3 n_{\rm He^+} n_{\rm e} \alpha_{\rm B}({\rm He}, T) \tag{2.20}$$

where $R_{\rm He}$ is the radius of the He^+ zone. Furthermore, p can be assumed to be 1 (for low density this is a good approximation) and eq. 2.17 becomes:

$$Q_{\rm H} = \frac{4\pi}{3} R_{\rm S}^3 n_{\rm H^+} n_{\rm e} \alpha_{\rm B}({\rm H}, T) \tag{2.21}$$

Now that we have an estimate of the amount of ionized hydrogen and helium, we can compute the continuum emission of the nebula. The most important continuum emission processes are recombination, free-free emission of H II and He II and the Lyα two-photons decay emission.

The emission coefficients for unit volume for these processes can be written as:

$$\begin{aligned} j_\nu({\rm HI}) &= n_{\rm H^+} n_{\rm e} \left(\gamma_\nu^{\rm ff}({\rm H}^+, T) + \gamma_\nu^{\rm rec}({\rm H}^0, T) + \gamma_\nu^{\rm 2q}({\rm H}^0, T)\right) \qquad (2.22) \\ j_\nu({\rm HeI}) &= n_{\rm He^+} n_{\rm e} \left(\gamma_\nu^{\rm ff}({\rm He}^+, T) + \gamma_\nu^{\rm rec}({\rm He}^0, T)\right) \qquad (2.23) \end{aligned}$$

thus the total emission is:

$$E_\nu = \frac{4\pi}{3} R_{\rm S}^3 j_\nu({\rm HI}) + \frac{4\pi}{3} R_{\rm He}^3 j_\nu({\rm HeI}) \tag{2.24}$$

The total volume of emitting gas (for hydrogen and helium) can be computed by equations 2.21 and 2.20 so that we get:

$$E_\nu = Q_{\rm H} \frac{\gamma_\nu^{\rm ff}({\rm H}^+, T) + \gamma_\nu^{\rm rec}({\rm H}^0, T) + \gamma_\nu^{\rm 2q}({\rm H}^0, T)}{\alpha_{\rm B}({\rm H}, T)} + Q_{\rm He} \frac{\gamma_\nu^{\rm ff}({\rm He}^+, T) + \gamma_\nu^{\rm rec}({\rm He}^0, T)}{\alpha_{\rm B}({\rm He}, T)} \, . \tag{2.25}$$

Free-free emission is computed as described in Bressan et al. (2002), while other coefficients are from Burgess & Summers (1976), Aller (1984), Osterbrock (1989), Ferland (1980) and Nussbaumer & Schmutz (1984). The He III contribution to the nebular emission is very small and can be neglected.

Fig. 2.10 shows the emission coefficients for free-bound transitions of H, He I and He II, for two-photons decay and for free-free emission (at electron temperature 10^4 K).

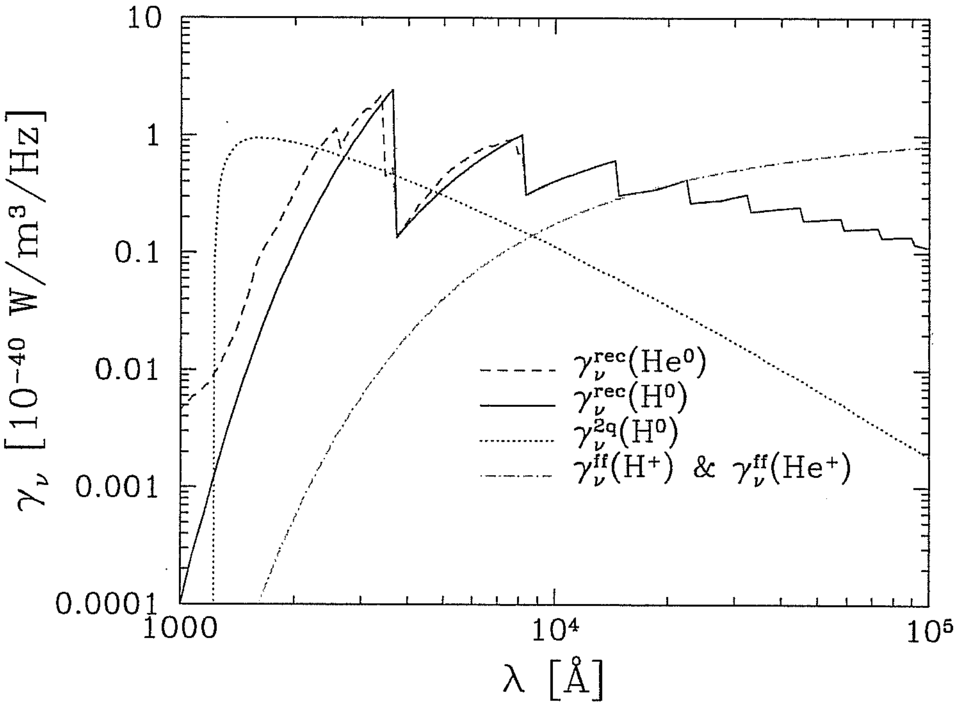

Figure 2.10: Emission coefficients for hydrogen (long-dashed: free-free; solid line:recombination; dotted: two photon decay) and helium (long-dashed: free-free; short-dashed: recobination).

Chapter 3

Nebular emission in dusty galaxies

This chapter is dedicated to the integration of nebular emission calculations in a dusty galaxy. In Sect. 3.1 we will briefly introduce the issue population synthesis of dusty galaxies, while Sect. 3.2 summarize the description of galaxies used in GRASIL code. Sect. 3.3 generalises the method in order to compute the total nebular emission of a galaxy. In Sect. 3.4 we will compare the method with similar works in literature. Finally, in Sect. 3.5 we applied the model to the M82 galaxy and discuss which new constrains are introduced by nebular emission computations.

3.1 Introduction

The discovery by the InfraRed Astronomical Satellite (IRAS) that an important fraction of bolometric luminosity of galaxies is provided by the interstellar dust have clearly dimostrated, in the following years, that the dust is one of the most important component of the interstellar medium.

Dust is involved in many physical processes of the interstellar medium (such as the production of molecular hydrogen on dust grain surphace) but the most important effect (from our point of view) is its influence on the tranfer of radiation produced by stellar systems. In fact, the dust absorbes and scatters effectively the radiation at wavelengths smaller than 1 μm, and return the absorbed energy in the form of IR photons. So, the resulting spectral energy distribution of a galaxy is in many cases radically modified.

It is worth noticing that dust repocessing of stellar radiation is more severe in galaxies with ongoing massive star formation activity. Then, the computation of the spectral energy distribution of star forming galaxies requires an adeguate treatment of the transfer of radiation through a dusty medium. Moreover, the prediction of the infrared SED needs the the modelling of thermal emission of dust grains, eventually accounting for their thermal fluctuation.

Many models where presented in the past to compute the spectrophotometric evolution of galaxies in presence of dust (starting from Guiderdoni & Rocca-Volmerange 1987), but often without a comprehensive and coherent treatment of the radiative transport and the dust emission in a realistic geometry.

Silva et al. (1998) proposed a model (the GRASIL code) for spectro-photometric evolution of galaxies which computes the stellar radiation transport as well as the thermal emission of dust in deep detail, and with a fairly realistic geometry.

However, in star forming galaxies the stellar radiation is also reprocessed by gas that convert the ionizing flux of massive stars in nebular emission lines and continuum.

The direct link between massive stars and emission lines makes the latter an important estimator of the star formation rate. Anyhow, also emission lines suffer for dust extinction, but the almost constant intrinsic ratio of Hα to Hβ intensity, predicted by nebular emission models for a large variety of environments (e.g. Osterbrock 1989), is a milestone in the interpretation of the effects of the intervening dust absorption (the Balmer decrement method).

The above arguments point toward the necessity to build a model that treats the nebular emission in a consistent way with the dust reprocessing.

In the following, we present the spectro-photometric model GRASIL and how we implemented in the model the computation of nebular emission using the H II regions library described in the previous chapter.

3.2 Population synthesis with dust

In this section we summarise the main features of the population synthesis code GRASIL; more details can be found in Silva et al. (1998), Silva (1999, PhD thesis), and Granato et al. (2000).

The code was mainly developed by L. Silva and G. L. Granato and can be retrieved from the web[1]; its source is available on request from the authors.

3.2.1 The radiative model

The effect of dust on radiative transfer depends on the optical and physical properties of grains as well as on the geometrical distribution of dust and stars.

Geometry

GRASIL represents galaxies by means of two main components characterised by different shapes: a spheroidal component (the bulge) and a disky component (see Fig. 3.1). Dust, that may be present in both components, is divided in two phases: i) dense molecular clouds (MCs), where star formation is active, and ii) diffuse medium (or cirrus). Single

---

[1] URL: `http://web.pd.astro.it/granato/grasil/grasil.html`

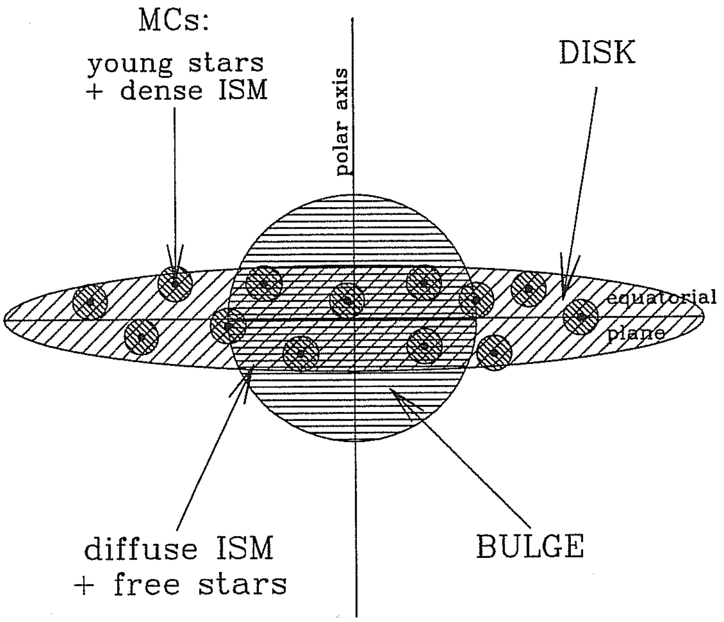

Figure 3.1: A schematic view of GRASIL representation of galaxies.

molecular clouds are modeled as thick spherical shells of dense gas (and dust) illuminated by central point sources, representing all the stellar content of the cloud.

Young stars are assumed to be born into MCs, and to leave them progressively as their age increases. As a consequence, the fraction of light of young simple stellar populations (SSPs) radiated inside MCs is a decreasing function of SSPs age, parameterised by the "escape time" ($\tau_{\rm esc}$). The analytical form of this function is (see Fig. 3.2):

$$\phi(t) = \begin{cases} 1 & \text{for } t < \tau_{\rm esc} \\ 2 - t/\tau_{\rm esc} & \text{for } \tau_{\rm esc} < t < 2\tau_{\rm esc} \\ 0 & \text{for } 2\tau_{\rm esc} < t \end{cases} \tag{3.1}$$

The time dependence of the escape fraction gives rise to an *age-selective extinction* because younger stellar generations are more attenuated than older ones.

The above schematization is also compatible with a scenario in which young stars destroy (with winds or SN explosions) the parent clouds. In this case $\tau_{\rm esc}$ would be a "destruction time", but the mathematical representation would be the same.

The light of older stars already escaped from MCs and the light eventually escaped from MCs is transferred througth the diffuse medium.

GRASIL can use several distributions for stars and dust; we refer the reader to Silva (1999) for a detailed description of all possible choices. Among the others, it is possible to choose a spheroidal configuration with a King profile in which the density ρ is given

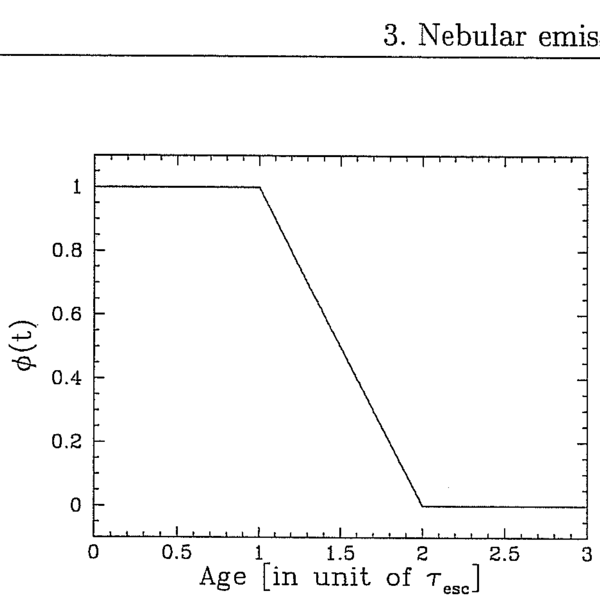

Figure 3.2: The fraction ($\phi(t)$) of light of young SSPs radiated inside MCs as a function of SSPs age.

by

$$\rho = \rho_0 \left(1 + \left(\frac{r}{r_{\rm c}}\right)^2\right)^{-\gamma} \tag{3.2}$$

where the parameters $r_{\rm c}$ (the core radius) and γ can be choosen for stars and dust separatelly. The other important configuration is the disk-like one in which an exponential profile is assumed:

$$\rho = \rho_0 \exp\left(-\frac{R}{R_{\rm d}}\right) \exp\left(-\frac{|z|}{z_{\rm d}}\right) \tag{3.3}$$

where the parameters $R_{\rm d}$ and $z_{\rm d}$ are the scalelength of the exponential disk. Also in this case it is possible to use different value for star and dust. Finally, it is possible to have a configuration with a spheroidal bulge plus a exponential disk.

Dust properties

GRASIL adopts a modified version of the "classical" description of dust from Draine & Lee (1984), consisting of two populations of grains (composed by graphite and silicate respectively), with spherical shape and a distribution of radii given by two power-law for each population:

$$\frac{{\rm d}n_i(a)}{{\rm d}a} = \begin{cases} A_i a^{\beta_1} & \text{if } a_{\rm b} < a < a_{\rm max} \\ A_i a_{\rm b}^{\beta_1-\beta_2} a^{\beta_2} & \text{if } a_{\rm b} > a > a_{\rm min} \end{cases} \tag{3.4}$$

where β_1, β_2, $a_{\rm b}$, $a_{\rm min}$, and $a_{\rm max}$ can be choosen for each of the two population, while A_i are derived from dust to gas ratio δ.

In addition, GRASIL includes also a population of PAH (Polyciclic Aromatic Hydrocarbons).

In this work we choose for graphite grains $a_{\rm min} = 8$ Å, $a_{\rm max} = 0.25$ μm, $a_{\rm b} = 50$ Å, $\beta_1 = -3.5$, $\beta_2 = -4$, while for the silicate grains $a_{\rm min} = a_{\rm b} = 50$ Å, $a_{\rm max} = 0.25$ μ and

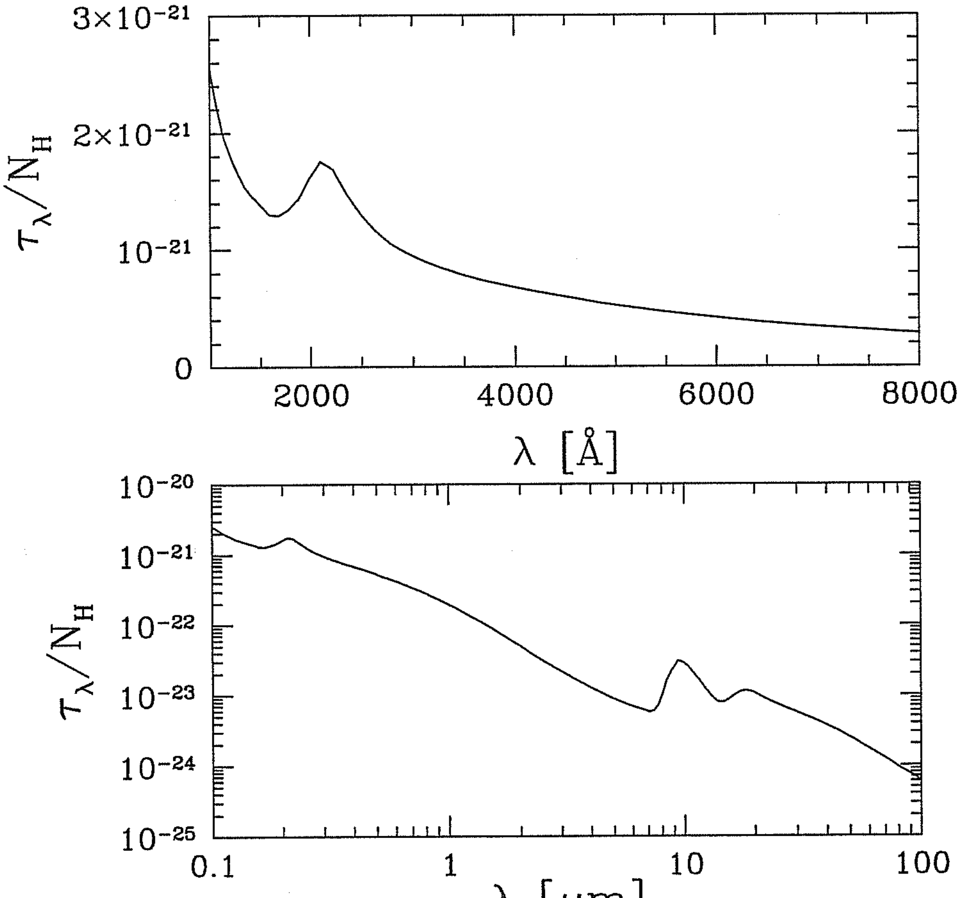

Figure 3.3: Extinction law for the dust misture that we adopted in this work. The misture adopted give rise to an extinction law very similar to the galactic one.

$\beta_1 = -3.5$. This choice produces an extinction law (see fig. 3.3) and emission properties that agree with the observed one in the Galaxy.

The code accounts also for the thermal emission of dust (and PAH molecules), both from big grains in thermal equilibrium, and from thermally fluctuating small grains (the stotactic heating) (Guhathakurta & Draine, 1989).

Radiation transport inside molecular clouds is computed using the model by Granato & Danese (1994). The optical thickness in these object can be high enough that dust absorbs its own thermal emission. In the most simple configuration, molecular clouds are modelled all equal to each other; however, it was introduced the possibility to account for two or more MC populations with different masses, radii and escape time. It is worth noticing that the optical thickness of molecular clouds is proportional to the ratio $m_{\rm MC}/r^2_{\rm MC}$, where $m_{\rm MC}$ and $r_{\rm MC}$ are the mass and the radius of molecular clouds, respectively.

Finally, the radiation transfer problem through the diffuse medium (taking into account emission from MCs) is solved and the volume emissivity is computed and integrated to provide the luminosity of the galaxy (from far UV to Sub-mm), at different inclination angles. Surface brightness maps are also possible but not computed.

Radio and molecular emission

Radio emission from simple stellar population completes the prediction of the continuum emissivity beyond the sub-millimetric regime. It is assumed to be the sum of free-free emission from electrons within HII regions and synchrotron emission from relativistic electrons accelerated in the interaction processes of ejecta of core collapse supernovae (CCSN) and the environment (Bressan et al., 2002). Non-thermal radio emission is set proportional to the CCSN rate, with a scaling law obtained from our Galaxy (Condon, 1992). Additional effects, such as synchrotron emission from young SN remnants, are roughly evaluated and are found to contribute not more than a few percent to the non-thermal emission. Radio emission combined with sub-millimetric and FIR ($\lambda \geq 100\mu$m) probes to be fundamental to disentangle the starburst and AGN contribution in obscured infrared luminous galaxies (LIRGs) and it is possible the only method to analyse the star formation processes occurring in luminous high redshift galaxies.

In collaboration with Olga Vega (INAOE, Mex) we have considered the emission from molecules (eg ^{12}CO and ^{13}CO) at several sub and millimetric transitions. A large velocity gradient code has been added and can now be used to predict line emissivity of several other molecules. The interface may make use of the parameters derived for the molecular clouds (metallicity, radius, density) in order to maintain consistency with the global fit of the galaxy SED. Currently the kinetic temperature of the gas is given as a parameter.

3.2.2 Chemical evolution

A fundamental input for GRASIL code is the star formation history which is provided by an external code. In this thesis, the star formation history is provided by a chemical code written by L. Silva and G. L. Granato. The code uses a one-zone description (i.e. with no dependence on space of SFR and chemical composition) of galaxies. The variation of the gas mass is given by three contribution: the consumption due to the star formation, the injection of processed gas by dying stars, and the infall of primordial gas.

The former term is computed by assuming a SFR $\Psi(t)$ that follows a Schmidt-type law (Schmidt, 1959), so that $\Psi(t) = \nu_{\rm sch} M_{\rm gas}^k$ plus (eventually) an analytical function (for example to simulate starbursts). We always assumed $k = 1$ in this work.
The processed gas returned from stars to ISM is computed by estimating the rate of death of stars and assuming an instantaneous recycling of ejected gas. The stellar ejecta are from Portinari et al. (1998).
Finally, the in-falling of primordial gas into the galaxies is assumed to be exponential ($\propto \exp(-t/\tau_{\rm inf})$).

3.2.3 Stellar Radiation

SEDs of stellar generations (SSP, simple stellar populations) have been computed by A. Bressan by following the prescriptions outlined in Bressan et al. (1994) and in Silva et al. (1998). These SEDs cover a wide range in age and metal content. They can be computed for an arbitrary initial mass function (IMF) and allow the use of different atmosphere models, from the low resolution (but wide parameter space coverage) Kurucz-Lejeune models (Kurucz, 1993; Lejeune et al., 1998), to the intermediate resolution models of Pickles (1998) and Jacoby et al. (1984). In the latter two cases, which are derived from observed stars, the corresponding fluxes have been extended into the unobserved region by means of the Lejeune et al. (1998) models. The use of higher resolution models is particularly useful when dealing with emission lines superimposed to absorption features of the intermediate age populations. As for the most massive stars, we have adopted the atmospheric models by Schaerer et al. (1996) for mass-losing blue supergiants, and the models by Schmutz, Leitherer & Gruenwald (1992) in the Wolf Rayet (WR) phase.

3.3 Total line emission from a galaxy

When a star cluster (or an OB association[2]) forms, the most massive stars in the cluster start to ionize the surrounding gas producing a H II region. This process halts the in-falling of the gas and inhibits a further continuation of the star formation in the cluster. Thus, in a simple description, once a H II region is produced its stellar content evolves in

---

[2] hereafter, we will not distinguish between OB associations and clusters, using "star cluster" to indicate both.

a passive way. In this case, the following time evolution of the H II region is determined by the ageing of the ionizing cluster, until the latter is no more able to produce enough Lyman photons to excite the gas.

When considering a star-forming galaxy as a whole, one must take into account different (in age) populations of star clusters, each one ionizing its own H II region. Thus, the total nebular emission of a galaxy is the integration of the emission from different populations of H II regions. Each population would be characterised by a different ionizing flux, hardness of the input spectra and ionization parameter. For these reasons, we consider in the model the emission of each different population. Thus, we split the recent (age < 30 Myr to be safe) star formation history in subsequent episodes of suitable duration, and then we compute their separate contributions to the total nebular emission.

It is worth stressing that this procedure is mainly dictated by the rapid variation of the intensity and shape of the ionizing continuum with the age, and, as a consequence, of the resulting nebular emission. Conversely, integrating the stellar emission over the time and computing the nebular emission from the resulting total spectrum would provide unrealistic results.

3.3.1 The method

Each population is supposed to be composed by identical H II regions whose nebular emission is computed from the ionizing photon fluxes Q_{H}, Q_{He}, and Q_{O}, by interpolating on the library.

The total emission in the line l (E_l) at the epoch of observation T, can be written as

$$E_l = \sum_j N_{\mathrm{HII},j} E_l^* (Q^*_{\mathrm{H},j}, Q^*_{\mathrm{He},j}, Q^*_{\mathrm{O},j}, Z_{\mathrm{gas}}) \tag{3.5}$$

where $N_{\mathrm{HII},j}$ is the number of H II regions that have formed in the galaxy in the time interval $[T - t_{j+1}, T - t_j]$, $Q^*_{\mathrm{H,He,O},j}$ are the corresponding ionizing photon fluxes, Z_{gas} is the current metallicity of the gas and E_l^* is the emission from the single H II region. The summation must be done until the star cluster of age t_j produce enough ionizing photons to excite a H II region.

$N_{\mathrm{HII},j}$ is obtained by assuming that each H II region is illuminated by a single cluster of total mass M^*, so that

$$N_{\mathrm{HII},j} = \frac{\int_{t_j}^{t_{j+1}} \Psi(T-t)dt}{M^*} \tag{3.6}$$

where Ψ is the SFR as a function of time. $Q^*_{\mathrm{H},j}$ for the single H II region at different ages can be obtained by

$$Q^*_{\mathrm{H},j} = \int_{\nu_{\mathrm{H}}}^{\infty} \frac{L^*_{\nu,j}}{h\nu} d\nu = \frac{\int_{\nu_{\mathrm{H}}}^{\infty} \int_{t_j}^{t_{j+1}} \Psi(T-t)(S_\nu(t, Z(T-t))/h\nu)dtd\nu}{N_{\mathrm{HII},j}} \tag{3.7}$$

where $S_\nu(t,Z)$ is the SSP SED. We have also emphasised the dependence on the metallicity of the ionizing spectrum $L^*_{\nu,j}$ of the single star cluster. Similar expressions hold for $Q^*_{\mathrm{He},j}$, and $Q^*_{\mathrm{O},j}$.

The emission properties of the j population depend on the ratios $Q^*_{\mathrm{He},j}/Q^*_{\mathrm{H},j}$ and $Q^*_{\mathrm{O},j}/Q^*_{\mathrm{He},j}$, that are constrained by the age of the j population, and on the average ionization parameter of the H II regions $\langle U\rangle^*_j$. The correspondence between the integrated Lyman continuum of the population j (expressed by $N_{\mathrm{HII},j}\times Q^*_{\mathrm{H},j}$) and $\langle U\rangle^*_j$ is determined by the stellar mass M^* of ionizing clusters through equations 3.6, 3.7 and

$$\langle U\rangle^*_j = \frac{3\alpha_B^{2/3}}{4c}\left(\frac{3Q^*_{\mathrm{H},j}n_{\mathrm{H}}\epsilon^2}{4\pi}\right)^{1/3} . \tag{3.8}$$

As shown in Fig. 2.9, H II galaxies exhibit a big variation of the ionization parameter value, which means that the value of stellar mass M^* and/or of the filling factor are subject to substantial variations. Observations (e.g. Kennicutt 1984) suggest that M^* varies approximately from 1000 to 10^6 $\mathrm{M}_\odot$ and ϵ from 0.1 to 0.001.

The duration of the subsequent episodes in which we split the SF history should be chosen by considering the evolution of the shape of the ionizing spectra. A lower limit is set by considering that each H II region will be illuminated by all the stars formed within the finite formation time of a typical star cluster, that we assume to be 1 Myr (see e.g. Fuente et al. 2001).

As remarked in Sect. 2.7, the presence of dust inside H II regions can be important. Thus one can multiply the nebular emission obtained from eq. 3.5 by a factor $1 - f_{\mathrm{d}}$.

The above method to compute nebular emission in galaxies is quite general, and can be easily implemented in all population synthesis models.

3.3.2 The implementation in GRASIL code

We implemented the method described above in the spectro-photometric code GRASIL.

The nebular emission is produced in H II regions that are just around the massive stars that excite them, so that nebular emission is extinguished as the stellar population that produce them (see Fig. 3.4). Ionizing stars have a short lifetime, so nebular emission in emitted prevalently when these stars are still inside parental molecular clouds. However, when the escape time is short enough, a significant number of ionizing photons can arise from star generations outside MCs and, consequently, we need to consider also H II regions extinguished only by the cirrus component. It is worth noticing that also nebular emission, as stars, suffer a age selective extinction.

The total energy in emission lines is quite small compared to the bolometric luminosity of young stellar populations, being always less than 20%. For this reason, the contribution of emission line energy absorbed by dust is neglected in computing the dust energetics. As discussed in Sect. 2.7, in the case of very small dust containt, the Lyα

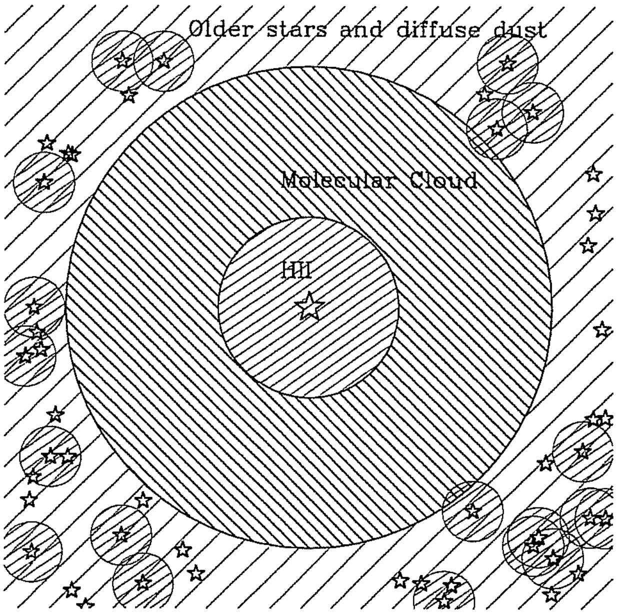

Figure 3.4: Simple schematization of geometrical arrangement of ionized gas in the GRASIL model. Youngest stars ionize the gas inside MCs, so that their nebular emission is extincted by parental MCs. Young stars that already escaped from MCs can produce nebular emission that only suffers the cirrus extinction.

photons can produce an important fraction of the dust luminosity. We will introduce the computation of absorbed line energy in the future releases of GRASIL.

The final output of the model is a complete and detailed spectrum of star-forming galaxies, from far-UV to the radio wavelengths (an extension to X-ray band is in progress, Silva et al. in preparation), including stellar absorption features, nebular emission, dust and PAH emission. A first application is shown in Sect. 3.5 in which it can be appreciated the detail of GRASIL simulated SEDs.

3.4 Comparison with other models

A first attempt to build a population synthesis model that includes the nebular emission was done by Guidardoni & Rocca-Volmerange (1987). In this model, the luminosity of several UV and optical lines were computed assuming a fixed ratio between the specified line and Hβ. The luminosity of the latter was assumed to be proportional to the ionizing photon flux.

A very similar approach was presented by Fioc & Rocca-Volmerange (1997, the PEGASE code). The work was improvement by extending the spectral window and the inclusion of different metallicities of stars. However, nebular emission is are always computed by constant scaling with the ionizing photon flux, regardless of the metallicity, the ionization parameter and the density.

Moy et al. (2001) have improved upon the previous model by coupling the total spectrum resulting from the synthesis, with *Cloudy*. While this approach can be correct in the case of a burst of short duration, it can not be used in the case of continuos star-formation as we already discussed.

A recent analysis of emission properties in star forming galaxies is by Charlot & Longhetti (2001). These authors obtained the emission from the galaxy by summing the line intensities of separate SSPs of given constant average metallicity, weighted by the corresponding SFR. Charlot & Longhetti also have a more detailed model for dust absorption (from Charlot & Fall 2000) than Moy et al. (2001), that accounts for an age selective extinction.

Among the models exsisting in literature, the approach of Charlot & Longhetti (2001) is the most similar to our one. However, they can not compute the spectral distribution of dust emission. A clear improvement of our model respect to other one is that we can now make a consinstent comparison between emission lines and the continuum at all wavelength, from UV to radio.

The main difference in the line emission computation between Charlot & Longhetti's method and ours is that we are able to compute the emission lines for many different choices of density, filling factor and stellar mass in a single run of GRASIL in a very small computational time. Also, we relax the hypothesis that the metallicities of the excited gas and of the ionizing stellar population are the same (even if a non-negligible difference is expected only in extreme situations).

3.5 Fitting the SED of a nearby galaxy: M82

As a first application, we used the code to reproduce the observed SEDs of the nearby galaxy M82. This study is useful to test the validity of code results and to show the capability of the code at reproducing the details in the spectral energy distribution of a galaxy, at all wavelengths. Moreover, we will show that emission lines provide new constrains on the parameters of GRASIL code.

M82 (NGC 3034) is one of the most studied galaxies and it is considered a prototype of starbursts galaxies. Due to the proximity of this object (3.25 Mpc), it appeares as the most luminous IR source in the sky, and its SED can be studied in detail. Moreover, using HST it is also possible to observe the single star clusters.

The starburst activity in M82 is a consequence of the interaction with M81 and NGC 3077. Observations (for example, see de Grijs et al., 2001) pointed out that this interaction caused different starburst episodes. The major one was around 0.6-1 Gyr ago and suppressed the following star formation activity until some 10^7 yr ago, when the present starburst switched on. The presence of the deep stellar features of Balmer series in the optical spectrum by Kennicutt (1992) is a confirm of an old burst.

M82 is morphologically classified as an Irr galaxy; however, a deeper analysis (Achtermann & Lacy, 1995) shows the presence of a spiral-like structure, nearly edge-on (inclination 80°) with the possible presence of a bar.

3.5.1 The simulations

Using these informations, we simulated a star formation history with two bursts, the older one between 0.8 and 0.6 Gyr (see fig. 3.5). The SFR during the burst is given by an esponential (SFR $\propto \exp(-t/t_\mathrm{b})$)

A first model (model A) was built to give a good reproduction of the photometric data, especially taking into account that some data can suffer for aperture corrections. The assumed parameters are reported in table 3.1 and the resulting SED is reported in figure 3.6, upper panel, compared with photometric data form literature. The mass of the galaxy is constrained by the optical and NIR data, while the IR and radio emission constrain the strength of the recent burst and the e-folding time t_b. Furtermore, the total baryonic mass ($1.8 \cdot 10^{10} M_\odot$) and the SNe rate (0.1 yr^{-1}) are in agreement with observations (McLeod et al., 1993; Doane & Mathews, 1993).

However, the optical depth of molecular clouds provided by the best fit of the photometric data (model A) is so high (τ_MC = 25 mag at 1 μm) that optical emission lines can not emerge from such model. Furthermore, the ionizing flux produced is too small to provide the observed Brα flux, also in the dust-free hypothesis.

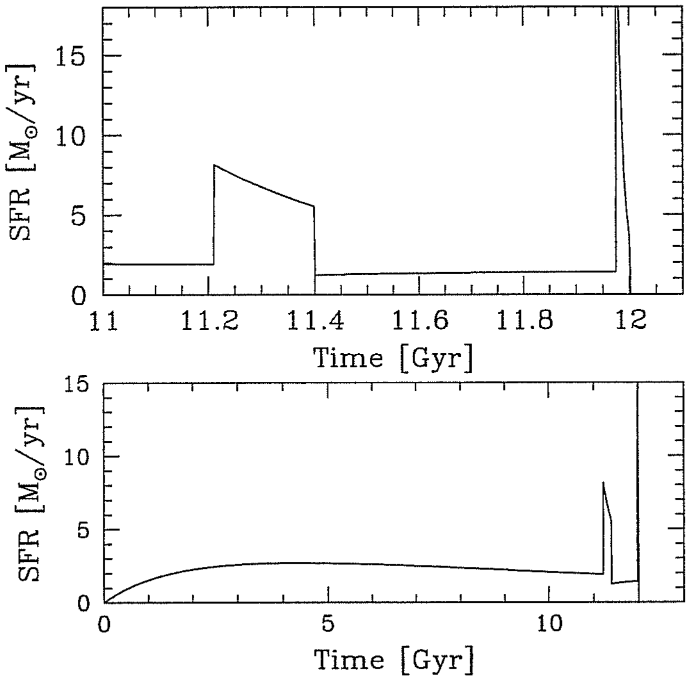

Figure 3.5: The simulated star formation history for M82. The upper panel shows the last Gyr.

Table 3.1: Parameters for M82 models.

Parameter	Model A	Model B	Comments
ν_{sch}	0.9 Gyr^{-1}	0.9 Gyr^{-1}	Efficiency of schmidt law
τ_{inf}	12. Gyr	12. Gyr	Infall timescale
M_{G}	$1.8 \cdot 10^{10} M_\odot$	$1.2 \cdot 10^{10} M_\odot$	Baryonic galaxy mass
t_{b}	10 Myr	15 Myr	e-folding time of the actual burst
M_{burst}	$2.3 \cdot 10^{8} M_\odot$	$2.6 \cdot 10^{8} M_\odot$	Mass converted in stars in the burst
τ_{MC}	25	1.5	Optical thickness of MCs at 1 μm
τ_{esc}	70 Myr	70 Myr	Escape time
θ	80°	80°	Inclination
n_{H}	100 cm^{-3}	100 cm^{-3}	H II region density
$(M^{*}\epsilon^{2})^{1/3}$	0.17 $M_\odot$	0.17 $M_\odot$	Normalization constant
R_{d}	1.3 kpc	1.3 kpc	Radial scalelength of the galactic disk
z_{d}	0.25 kpc	0.25 kpc	Vertical scalelength of the galactic disk

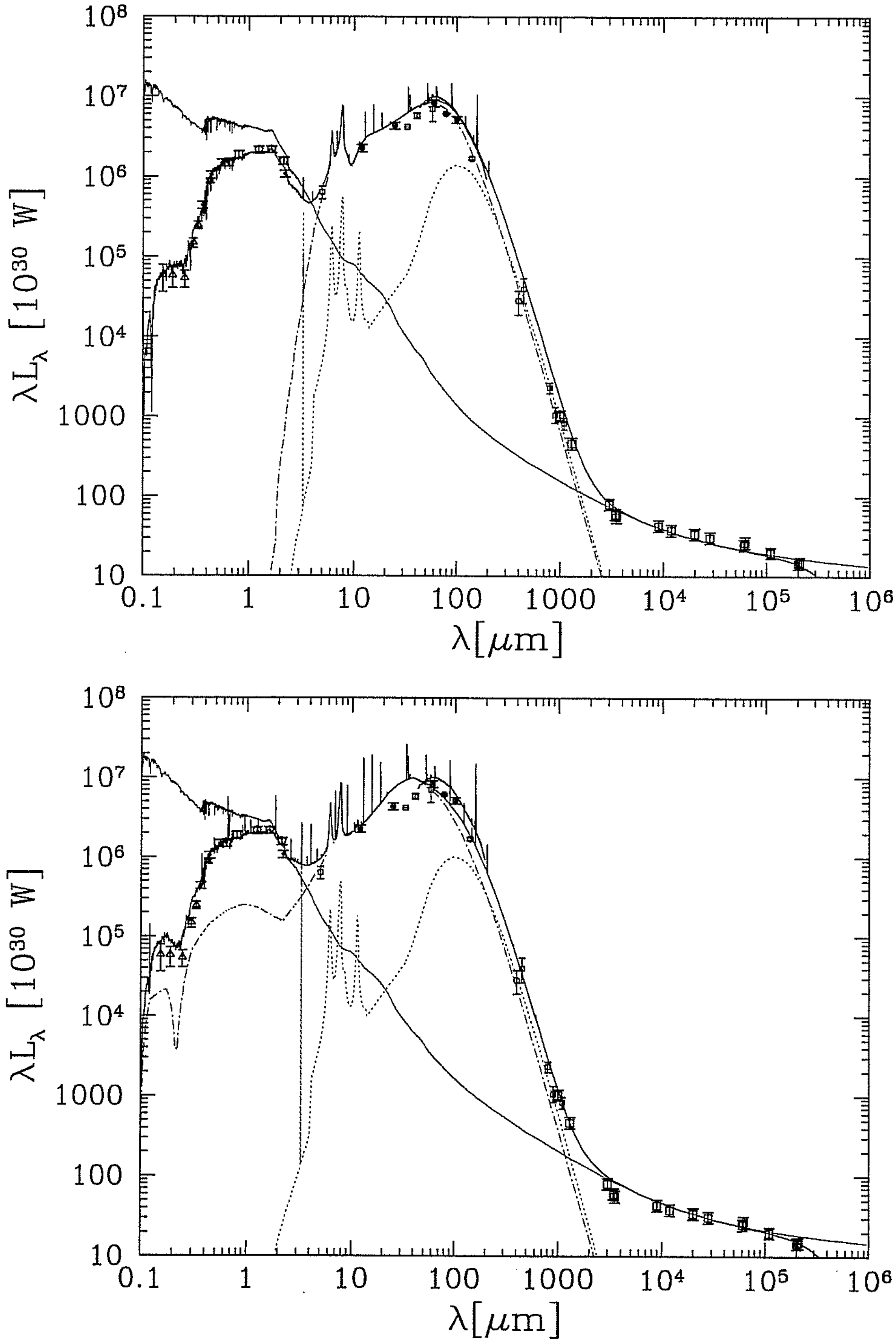

Figure 3.6: The global spectral energy distribution of M82, for the model A (upper panel) and model B (lower panel). Photometric data are from: UV: Code & Welch 1982 (1982) (open triangles); NIR: 2MASS (Jarrett et al., 2003); FIR spectrum: Colbert et al. (1999); IRAS: Soifer et al. (1989); Sub-mm and other IR data: Telesco & Harper (1980), Jaffe et al 1984, Hughes et al 1990, Radio: Huang et al. (1994). The different lines represent: the unextincted continuum (thin solid), the emission of cirrus (dotted), the radiation emerging from molecular clouds (dot-dashed), and the final SED (thick solid).

Moreover, the predicted final metallicity is around $2Z_{\odot}$. This value would produce an emitted ratio [O II]/H$\alpha \sim 0.05$, much lower than the observed one (0.115). The high value of final metallicity is a consequence of the assumption on the IMF to be a Salpeter one. As noted by Portinari et al. (2003) and Chabrier (2003), the Salpeter IMF tends to produce too many metals and to have a high mass over luminosity ratio. Investigation on the more appropriate IMF will be done in future works.

In model B we fitted together the SED and the emission lines. In order to reproduce [O II] and [O III] optical lines we assumed the gas and star metallicity during the last Gyr to be solar. We also changed the e-folding time $t_{\rm b}$ of the present burst and its strength in order to get the necessary ionizing flux to reproduce the observed hydrogen emission lines. The other nebular line also depend on the ionization parameter. The latter is a function of the mass of ionizing clusters M^*, and of the filling factor ϵ through eq. 3.8 and scale linearly with the quantity $m \equiv (M^*\epsilon^2)^{1/3}$. The appropriate value of m is constrained in M82 from the luminosity of [O III]51.8μm and [O III]88.36μm, while the gas density $n_{\rm H}$ is derived from the ratios [O III]51.8μm/[O III]88.36μm and [N II]205μm/[N II]121.9μm. The fit (shown in fig. 3.6) to the observed photometric data is good, although the simulated dust emission seems to be warmer with respect to observations. The comparison of some observed line luminosities with the computed ones is reported in table 3.2. An acceptable or even very good agreement between observed values and simulated ones can be noted for most of the lines.

In fig. 3.7 we show the comparison between the simulated SED with the optical spectrum given by Kennicutt (1992); it can be noted that the model is able to reproduce the absorption stellar features quite well.

3.5.2 Discussion

Even if we restricted the fitting of SEDs to one example, it is possible to withdraw some more general conclusions.

The GRASIL code is now able to reproduce the complete SED together with emission lines. The inclusion of emission lines introduces two new parameters ($M^*\epsilon^2$ and $n_{\rm H}$), however their value can be fixed from the luminosity of different lines. On the other hand, nebular emission provides new important constrains.

It is now possible to constrain the optical depth $\tau_{\rm MC}$ of molecular clouds. It resulted that optical lines impose much smaller optical depths than what typically used (20 mag or more) in previous works with GRASIL. As a consequence, it was necessary to take into account the thermal fluctuations of dust grains also inside MCs. It is worth noticing that the SED of dust emission of a thick molecular cloud is not very different from the one of a thin MC.

This result does not exclude that a fraction of molecular clouds have a much higher thickness. However, the total IR luminosity and the shape of radio emission are able to constrain the SFR and, as a consequence, to fix the number of ionizing photons avaible

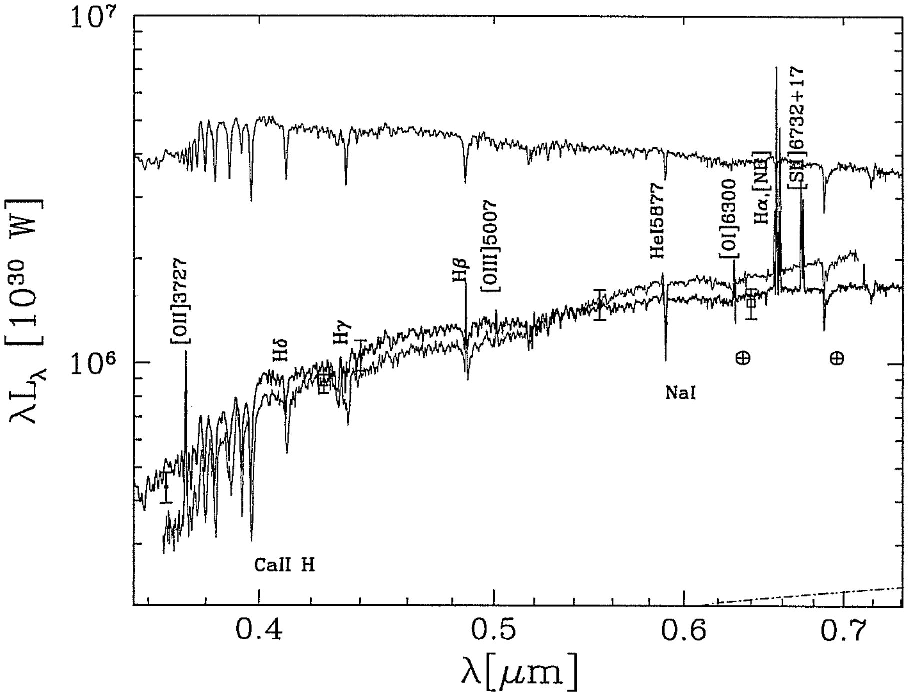

Figure 3.7: Optical SED of M82. The simulated SED (thick line) is compared to a spectrum from Kennicutt (1992), the latter normalised to have a flux $2.19 \cdot 10^{32}$ W/Å at 5500 Å. Some emission lines are highlighted, as well as the stellar absorption doublet Ca II H, the interstellar absorption of Na I and two telluric features. The resolution power $\lambda/\Delta\lambda$ used (1000) is very similar to the one in the observed spectrum.

Table 3.2: Comparison between some calculated and observed emission lines for M82 galaxy. Luminosities are given in 10^{33} W. Observed values are taken from: (1) McCarthy et al. (1987), (2) Willner et al. (1977), (3) Satyapal et al. (1995), (4) Colbert et al. (1999), (5) Petuchowski (1994), (6) Houck et al. (1984), (7) Lord et al. (1996), (8) dervived from the spectrum by Kennicutt (1992).

Line	Model B	Observed	Uncert.	Reference
Hα	4.60	5.40	—	1
Brα	1.86	2.01	—	2
Brγ	0.40	0.67	—	3
[CII]157.74μm	14.3	16.9	0.16	4
[NII]121.9μm	2.31	2.1	0.4	4
[NII]205μm	0.84	0.88	0.13	5
[NIII]57.32μm	2.07	4.3	0.63	4
[OI]63.18μm	7.1	22.2	0.63	4
[OI]145.5μm	0.66	1.52	0.13	4
[OII]3726-29	0.58	0.62	—	8
[OIII]5007	0.19	0.40	—	8
[OIII]51.8μm	11.5	13.0	0.6	4
[OIII]88.36μm	12.6	10.8	0.5	4
[NeII]12.8μm	15.7	15.8	4.5	7
[SiII]34.8μm	9.8	15.2	0.3	7
[SII]6717-31	3.3	2.5	—	8
[SIII]18.7μm	11.4	6.56	2.15	7
[SIII]33.4μm	17.6	14.7	2.0	6

for nebular emission. The possible presence of a population of molecular clouds with higher thickness would show a enanched IR emission with respect to the Hα luminosity corrected for extinction. This effect is not commonly observed in normal galaxies, but there is some claim (Poggianti & Wu, 2000) that it is present in Luminous IR galaxies.

Another consequence of the small optical depth of MCs is that the feature at 10 μm, commonly attributed to the silicate absorption, is actually due, in our models, to the PAH emission at the edge of the feature.

The results on M82 show also that metallic lines give important constraints on the metallicity estimations. As expected, on the basis of photometric data only it is not easy to break the degeneracy between age, metallicity and dust attenuation. On the contrary, the emission lines are good metallicity diagnostics.

Chapter 4

Dust attenuation in normal star-forming galaxies

In this chapter we will discuss several methods to estimate the attenuation in star forming galaxies by considering the UV, optical emission lines and FIR properties. After the introduction (Sect. 4.1), in Sect. 4.2 we summarize some methods to extimate the dust attenuation in normal[1] galaxies. In Sect. 4.3 we compare the observed attenuation in UV and Hα for a sample of spiral galaxies with our models. We show that observations require the extinction of different stellar populations to vary with age. In Sect. 4.4 we discuss the importance of the results.

4.1 Introduction

In star forming galaxies, the intrinsic UV and Hα luminosities are directly related to the star formation activity. On the other hand, the main difficulty in estimating the star formation rate is the presence of dust.

In the past, several methods were proposed for the measure of dust effects on stellar radiation. However, different methods give results that are often in disagreement with each other due to the complexity of dust distribution with respect to stars.

The treatment of radiation transport in a realistic distribution of dust and stars in GRASIL allows us to compare these different methods. Furthermore, we can underline the role of age-dependent (or age selective) extinction.

Notice that we will use the term *extinction* when it refers to the loss of light along the line of sight of a structureless source (as a stars) due to dust in between the sorce and the observer. The extinction is defined as the difference in magnitude between the emitted and the observed flux. In this case, the extinction is the result of absorption plus

---

[1] In this work, we will use the name "normal star-forming galaxies" as synonymous of spiral galaxies without starburst activity.

the scattering of light outside the light of sight. When dealing with complex sources as galaxies, stars and dust are mixed. In this case, the light radiated toward the observer is extincted, but some light emitted in other directions can be scattered into the line of sight. The resulting total decreament of flux into the line of sight is referred as *attenuation.* It is worth noticing that extinction and attenuation are not equivalent and we will distinguish between the extinction law (the extinction as a function of wavelength) and attenuation law.

4.2 Estimation of UV and Hα attenuation

Attenuation in local star forming galaxies can be derived in several ways. A common method is to relate the UV attenuation to the attenuation in Hα. The gas attenuation at Hα is derived from the ratio between the luminosity of Hβ and Hα (currently called Balmer decrement). This ratio is given by:

$$\frac{L_{\mathrm{H}\alpha}}{L_{\mathrm{H}\beta}} = \frac{j_{\mathrm{H}\alpha}}{j_{\mathrm{H}\beta}} e^{(\tau_{\mathrm{H}\beta} - \tau_{\mathrm{H}\alpha})} \tag{4.1}$$

where $j_{\mathrm{H}\beta}/j_{\mathrm{H}\alpha}$ is the ratio of Hβ and Hα emission coefficients (typically assumed 2.87 at an electronic temperature of 10^4 K, see Osterbrock 1989) and $\tau_{\mathrm{H}\alpha}$ and $\tau_{\mathrm{H}\beta}$ are the optical depth at the two wavelengths. Then:

$$\tau_{\mathrm{H}\alpha} - \tau_{\mathrm{H}\beta} = -\ln\left(\frac{j_{\mathrm{H}\beta}}{j_{\mathrm{H}\alpha}}\frac{L_{\mathrm{H}\alpha}}{L_{\mathrm{H}\beta}}\right) \quad \Rightarrow \quad \tau_{\mathrm{H}\alpha} = \frac{1}{e_{\beta\alpha} - 1}\ln\left(\frac{j_{\mathrm{H}\beta}}{j_{\mathrm{H}\alpha}}\frac{L_{\mathrm{H}\alpha}}{L_{\mathrm{H}\beta}}\right) \tag{4.2}$$

$$A_{\mathrm{H}\alpha} = 1.086\frac{1}{e_{\beta\alpha} - 1}\ln\left(\frac{j_{\mathrm{H}\beta}}{j_{\mathrm{H}\alpha}}\frac{L_{\mathrm{H}\alpha}}{L_{\mathrm{H}\beta}}\right), \tag{4.3}$$

where $e_{\beta\alpha} = \tau_{\mathrm{H}\beta}/\tau_{\mathrm{H}\alpha}$ and can be derived from the adopted extinction law. For the galactic extinction law $e_{\beta\alpha} = 1.47$.

Calzetti (1997) suggested that the attenuation of the stellar continuum is only a fraction (~ 0.44) of the attenuation of the ionized gas. By extending this assumption to the UV while adopting the galactic extinction law, it is straightforward to obtain (at $\lambda_{\mathrm{UV}} = 2000$ Å, e.g. Buat et al. 2002)

$$A_{2000} = 1.6 A_{\mathrm{H}\alpha}\,. \tag{4.4}$$

An alternative method to derive the UV attenuation is to consider the reprocessing of star light into the infrared emission. Following Meurer et al. (1999) (see also Calzetti et al. 2000), the ratio between the FIR and UV fluxes (now $\lambda = 1600$ Å) can be written as:

$$\frac{F_{\mathrm{FIR}}}{F_{1600}} = \frac{F_{\mathrm{Ly}\alpha} + \int_{912}^{\infty} f_{\lambda,0}(1 - 10^{-0.4A_\lambda})\mathrm{d}\lambda}{F_{1600,0}10^{-0.4A_\lambda}}\frac{F_{\mathrm{FIR}}}{F_{\mathrm{dust}}} \tag{4.5}$$

where the infrared flux $F_{\rm FIR}$ is defined as the flux in the [40–120] μm interval derived from the 60 and 100 μm IRAS bands (Helou et al., 1988), and $F_{1600} = 1600 \cdot f_{1600}$ (in W cm^{-2}). The first term of the above equation is the ratio between the energy absorbed by dust and the observed UV flux, while the second is the fraction of energy emitted by dust in the FIR window.

Assuming that the energy re-emitted by dust in a galaxy is provided primarily by the UV flux of young star populations and that the fraction of the bolometric stellar flux absorbed is equal to the fraction of flux absorbed in the UV, Meurer et al. obtained

$$\frac{F_{\rm FIR}}{F_{1600}} \simeq (10^{0.4A_{1600}} - 1)\frac{F_{\rm Ly\alpha} + \int_{912\mathring{A}}^{\infty} f_{\lambda,0} {\rm d}\lambda}{F_{1600,0}} \frac{F_{\rm FIR}}{F_{\rm dust}} \tag{4.6}$$

where the second term is essentially a bolometric correction for the UV flux. Using population models by Leitherer & Heckman (1995) they obtain that for a burst $\int f_{\lambda,0} {\rm d}\lambda / F_{1600,0} \simeq 1.66$. Then, from the SEDs of some ultraluminous infrared galaxies observed by Rigopoulou et al (1996), they derive $F_{\rm dust}/F_{\rm FIR} \simeq 1.37$. Finally, solving eq. 4.6 as a function of A_{1600} we get:

$$A_{1600} = 2.5 \log\left(\frac{F_{\rm FIR}}{0.84 F_{1600}} + 1\right) . \tag{4.7}$$

Note that the latter was derived for starburst galaxies.

In the same framework, Buat et al. (1999) proposed a relation between the UV attenuation and the $F_{\rm FIR}/F_{\rm UV}$ ratio ($\lambda_{\rm UV} = 2000$Å), which is suited for normal star forming galaxies:

$$A_{2000} = 0.466 + \log\left(\frac{F_{\rm FIR}}{F_{2000}}\right) + 0.433 \left[\log\left(\frac{F_{\rm FIR}}{F_{2000}}\right)\right]^2 . \tag{4.8}$$

4.3 $A_{\rm UV}$ and $A_{\rm H\alpha}$ in normal star-forming galaxies

Buat et al. (2002, hereafter B02) compared the $A_{\rm UV}$ derived from the ratio $F_{\rm FIR}/F_{\rm UV}$ (eq. 4.8) with the attenuation suffered by Hα in a sample (called SFG sample) of normal star forming galaxies. The SFG sample consists of 47 spiral and irregular galaxies in nearby clusters. They were observed in the UV ($\lambda_{\rm UV} = 2000$ Å) with the SCAP, FOCA and FAUST instruments (Boselli et al., 2001), in the optical (Gavazzi et al., 2002), and in the FIR by IRAS. The galaxies were selected to have EW(Hα)> 6 Å in order to minimize the errors in Hα and Hβ fluxes. Galaxies with Seyfert activity were excluded from the sample. Metallicity of the galaxies in the sample ranges from $\sim Z_\odot/4$ to $\sim 2Z_\odot$.

In Fig. 4.1 we report the attenuation in Hα versus the value of $A_{\rm UV}$ derived from the ratio $F_{\rm FIR}/F_{\rm UV}$ for the SFG sample, as in Fig. 2 of their paper. As pointed out by Buat and collaborators, the two quantities show a lack of correlation, contrary to what is expected from eq. 4.4.

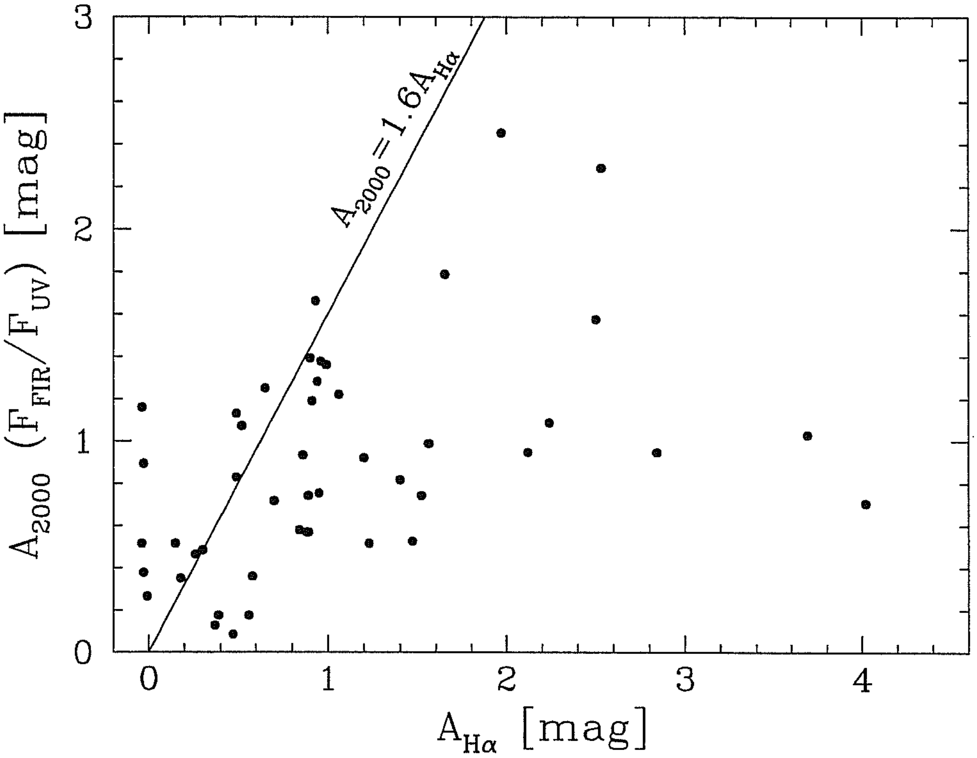

Figure 4.1: A_{2000} derived from the ratio $F_{\rm FIR}/F_{2000}$ (using eq. 4.8) versus the $A_{\rm H\alpha}$ from Balmer decrement for SFG sample data (filled circles).

4.3.1 Simulated disk galaxies

In order to give an interpretation of this observational problem, we simulated a set of disk galaxies by exploring the space of parameters appropriate for normal star forming galaxies. The star formation history, gas fraction and metal enrichment was computed with the chemical evolution code described in Sect.3.2.2. In order to point out the dependence of the results on metallicity, we considered different values for the metallicity of stars and gas from what obtained by the chemical code.

The parameters that regulate the star formation history in our models are the baryonic mass of the galaxy ($M_{\rm G}$), the gas infall time scale ($\tau_{\rm inf}$), and the star formation efficiency $\nu_{\rm sch}$ of the assumed linear Schmidt law. The age of the galaxies has been set to 10 Gyr. The star formation histories of some models are plotted in fig. 4.2.

The parameters that regulate the attenuation are the escape time $\tau_{\rm esc}$, the optical thickness of MC at 1 μm ($\tau_{\rm MC}$), and the orientation θ of the disk galaxy with respect to the celestial plane ($\theta = 0°$ means face-on models). The dust (extinction and emission) properties are similar to the galactic one (see fig. 3.3). The dust/gas ratio is assumed to be proportional to the metallicity. Emission lines are computed for different gas densities $n_{\rm H}$, filling factors ϵ and stellar masses of clusters M^*; however we concentrate on H recombination lines that do not depend on $n_{\rm H}$, M^* or ϵ. Table 4.1 summarizes the values of the parameters used in our computations.

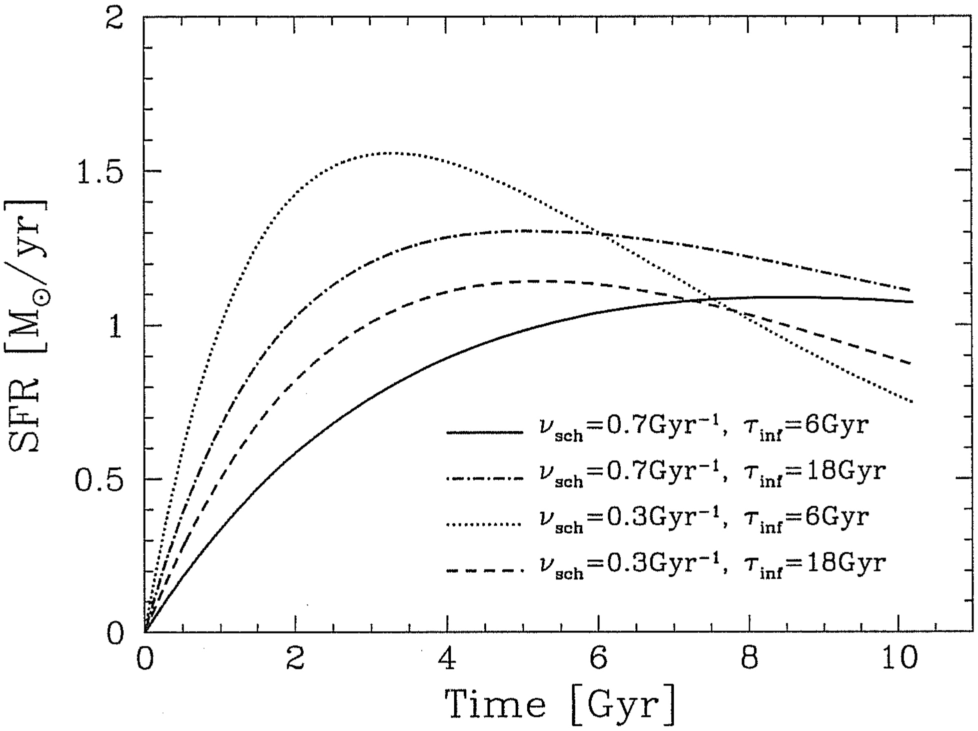

Figure 4.2: Star formation histories for some models with $M_{\mathrm{G}} = 10^{10}$ M$_\odot$.

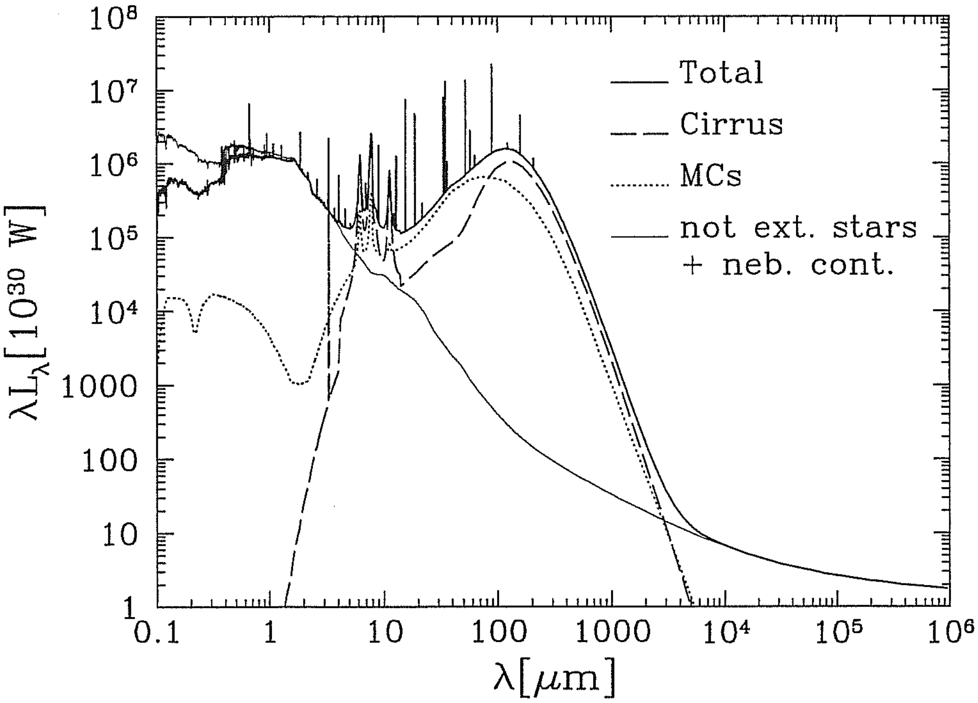

Figure 4.3: The global spectral energy distribution of the reference model () with inclination $\theta = 45°$. Different lines show different contributions.

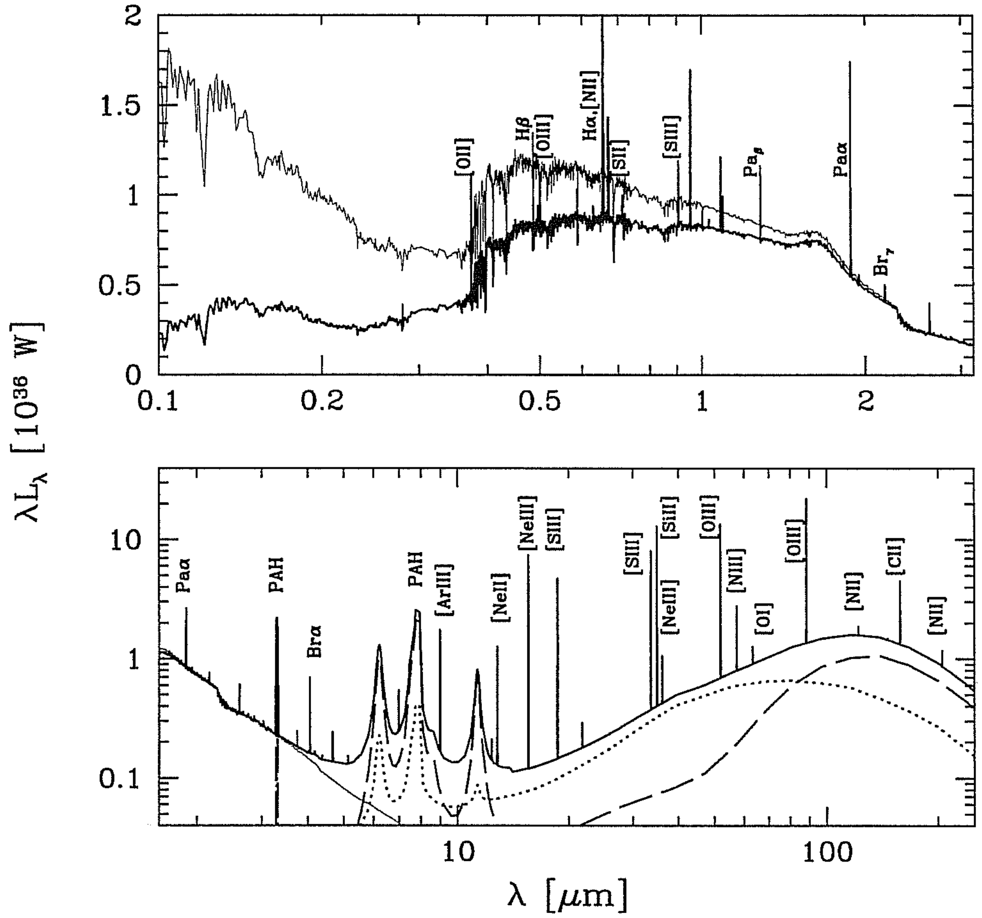

Figure 4.4: As fig. 4.3 but for two spectral regions. Top: UV-optical. Botton: Infrared. Some important emission line are identified.

Table 4.1: Values of the relevant parameters used to model normal star forming galaxies. Ref. model: see Sect. 6.

Param.	All models	Ref. model
$\tau_{\rm inf}$	6 – 18 Gyr	12 Gyr
$\nu_{\rm sch}$	0.3 – 0.7 Gyr^{-1}	0.3 Gyr^{-1}
$M_{\rm G}$	10^{10} – 10^{11} M$_\odot$	10^{10} M$_\odot$
Z	0.004 – 0.04	0.02
$\tau_{\rm esc}$	1 – 9 Myr	3 Myr
$\tau_{\rm MC}$	0.1 – 1.25	0.5
θ	0° – 90°	
$f_{\rm d}$	0.3	0.3

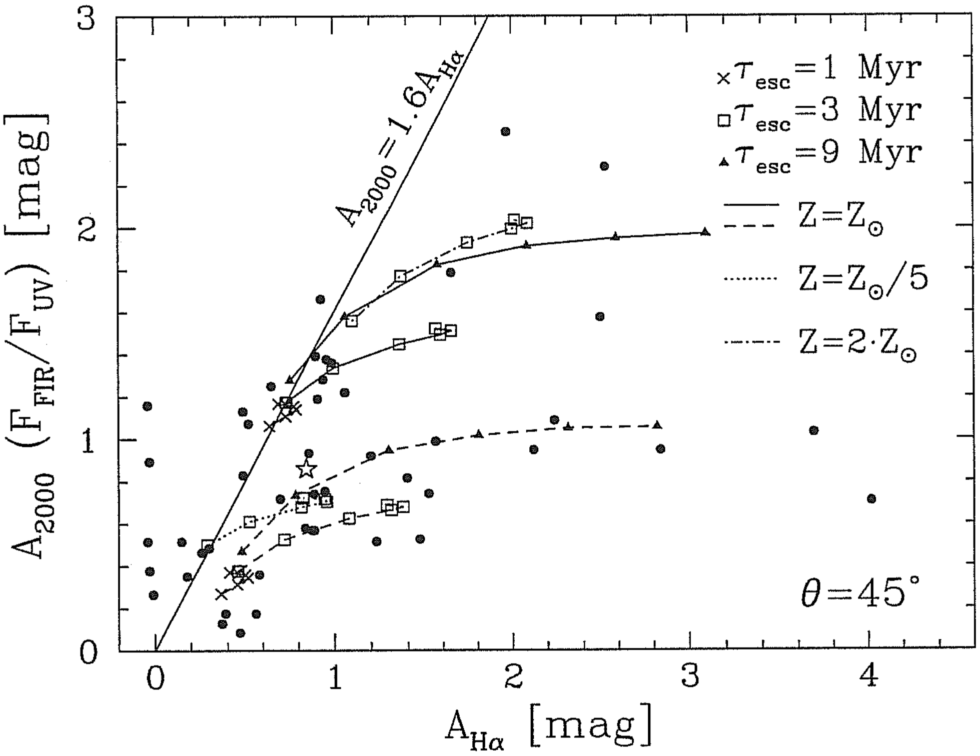

Figure 4.5: On the ordinate, A_{2000} derived from the ratio $F_{\mathrm{FIR}}/F_{2000}$ (using eq. 4.8); on the abscissa, $A_{\mathrm{H}\alpha}$ from Balmer decrement. Filled circles show SFG sample data. Lines connect models (see Sect. 4.3) with the same M_{G} and star formation history, but different τ_{MC}. Solid lines: $M_{\mathrm{G}} = 10^{11}$ M$_\odot$, $\nu_{\mathrm{sch}} = 0.3$ Gyr^{-1}, $\tau_{\mathrm{inf}} = 18$ Gyr, solar metallicity; dashed lines: $M_{\mathrm{G}} = 10^{10}$ M$_\odot$, $\nu_{\mathrm{sch}} = 0.7$ Gyr^{-1}, $\tau_{\mathrm{inf}} = 6$ Gyr, solar metallicity. To emphasize the dependence on metallicity, we show the first model (solid lines) for $\tau_{\mathrm{esc}} = 3$ Myr but $Z = 0.04$ (dot-dashed line) or $Z = 0.004$ (dotted line). For simplicity only models with $\theta = 45°$ are shown here.

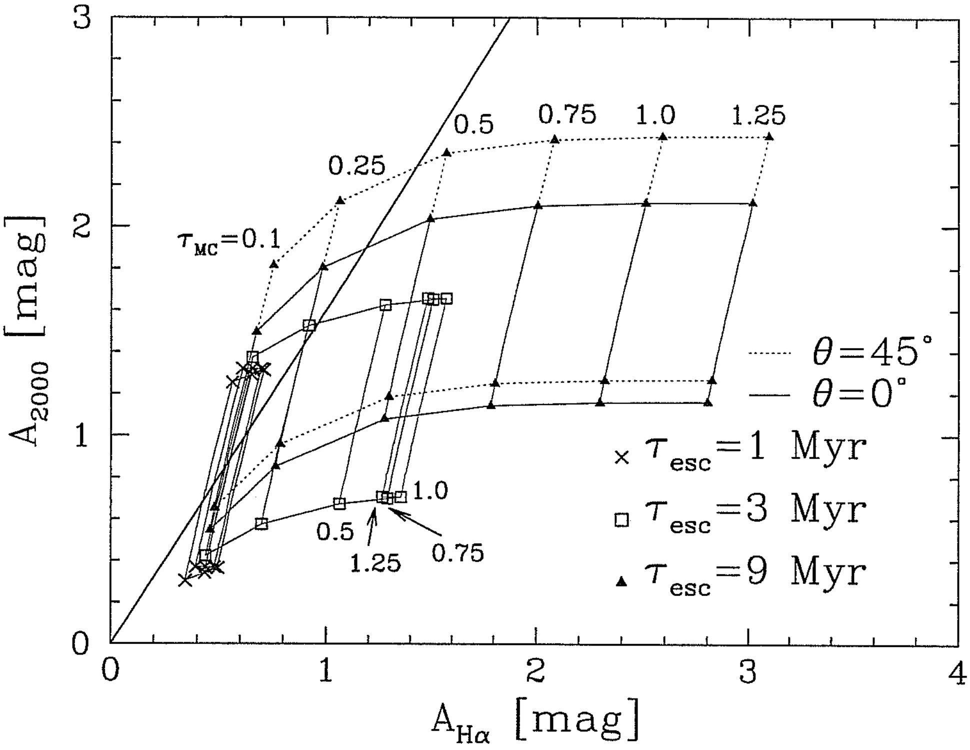

Figure 4.6: UV attenuation in the models versus the attenuation at Hα derived from the Balmer decrement. Almost vertical lines connect models with the same optical thickness of MC ($\tau_{\rm MC}$) and escape time ($\tau_{\rm esc}$), but different SF histories and dust content in cirrus. Only the less and most dusty models are associated to symbols which refer to the escape time. The thick solid line refers to equation 4.4.

The models are compared with data in Fig. 4.5; the attenuation at Hα is derived from the Balmer decrement (eq. 4.3), while the attenuation in UV has been derived by using eq. 4.8. For simplicity, we only represent the most dusty (solid lines) and less dusty (dashed lines) models; all other cases range between the two. Models refer to a 45° inclination; face-on models show a slightly lower attenuation, while edge-on models have larger attenuations and scatter.

The models cover quite well the location of the observed galaxies in this diagram and confirm a real lack of correlation between the UV attenuation, as derived from the $F_{\rm FIR}/F_{\rm UV}$ ratio and $A_{\rm H\alpha}$.

In order to clarify the origin of this scatter and to identify a good estimator of UV attenuation, we contrast the intrinsic UV attenuation – directly extracted from our models ($A_{\rm UV} = -2.5\log(L_{\rm UV}/L_{\rm UV0})$) – respectively with $A_{\rm H\alpha}$ from the Balmer decrement and $F_{\rm FIR}/F_{\rm UV}$ (see Figs. 4.6 and 4.7).

4.3.2 Attenuation from Balmer decrement

The scatter in Fig. 4.6 must be entirely ascribed to the interplay between the different stellar lifetimes associated to the emission properties and the geometry set by the critical escape time. In fact, Hα is mainly produced by ionizing massive stars with a lifetime around 3 Myr, while UV is also emitted by less massive and longer-living stars. We may devise the following typical cases.

- *Escape time shorter than the typical lifetime of an ionizing star*: crosses. Independently of $\tau_{\rm MC}$, the models tend to define a relation which seems however steeper than eq. 4.4. This is due to the fact that both Hα and UV emissions are mainly produced outside MCs, so that they do not respond to differences in $\tau_{\rm MC}$ and the attenuation is mainly due to the diffuse medium.

- *Escape time longer than the typical lifetime of an ionizing star*: triangles. Emission lines are produced only inside MCs, so $A_{\rm H\alpha}$ essentially measures $\tau_{\rm MC}$. When $\tau_{\rm MC} > 0.5$ the UV flux produced inside MCs is completely reprocessed into the IR. Thus, $A_{\rm UV}$ saturates while $A_{\rm H\alpha}$ still increases. This results in an almost horizontal displacement in Fig. 4.6.

- *Escape time comparable to the typical lifetime of an ionizing star*: open squares. At increasing $\tau_{\rm MC}$, the Hα to Hβ ratio increases from the emitted value to a maximum value fixed by the Hβ emitted outside the MCs and by the sum of the Hα still coming from within the MCs (the attenuation is lower at Hα than at Hβ) and from outside. Then the ratio decreases again to the asymptotic value fixed by the attenuation of the diffuse gas. This causes a behavior that is intermediate between the former two cases and, in particular, gives rise to the turnover shown at high $\tau_{\rm MC}$. As a consequence, the attenuation in Hα derived from the Balmer decrement is underestimated.

The variation in dust content of the galaxy and/or of the inclination, at constant $\tau_{\rm MC}$ and $\tau_{\rm esc}$, shifts the models in Fig. 4.6 along a constant direction, somewhat steeper than that of eq. 4.4; furthermore, a variation in metallicity corresponds to a variation of the amount of dust which varies the attenuation due to the diffuse component. These effects add further dispersion to the data.

The results suggest that galaxies in Fig. 4.5 with $A_{\rm H\alpha} \geq 1.5$ mag may be characterized by escape times larger than the typical lifetime of the ionizing stars. Models with $A_{\rm H\alpha} \geq 2.5$ mag have an equivalent width EW(Hα) lower than 6Å; there are several possible explanations for the higher observed $A_{\rm H\alpha}$ with large EW(Hα), such as a small burst (increasing the equivalent width), or an underestimate of Hβ or [N II] lines (giving higher $A_{\rm H\alpha}$).

The results of models and observations described above point out that age selective extinction is present in normal star-forming galaxies and complicates the picture of extinction in galaxies. The simple hypothesis of screen extinction does not work in this kind of galaxies; different ways to compute attenuation give inconsistent results because they rise from specific populations (ionizing and non-ionizing UV emitters) that have different lifetimes and live at different optical depths.

4.3.3 Attenuation from the continuum

A more robust estimation of the UV attenuation can be obtained by considering the energy reprocessed by dust in the IR.

In Fig. 4.7 we ploted the intrinsic $A_{\rm UV}$ against the ratio $F_{\rm FIR}/F_{\rm UV}$. The solid line represents eq. 4.8 and the short dashed line refers to eq. 4.7. To convert attenuation at 1600 Å of eq. 4.7 into $A_{\rm UV}$ at 2000 Å we assume $F_{1600} = F_{2000}$ and $A_{2000} = 0.9 \cdot A_{1600} = 0.9 \cdot 2.5 \log(F_{\rm FIR}/0.84 F_{2000} + 1)$, as in B02. Models show that, contrary to the case of Balmer decrement, the UV attenuation correlates quite tightly with the $F_{\rm FIR}/F_{\rm UV}$ ratio. The origin of this correlation is that the FIR flux is essentially provided by the UV emission of young stellar populations as assumed by Meurer et al. (1999) and Buat et al. (1999). Thus, the $F_{\rm FIR}/F_{\rm UV}$ measures the ratio between the reprocessed energy flux and the residual energy flux in the UV. Outside the MCs, a contribution to the FIR comes from the optical emission of old stellar populations; this causes a dispersion around the average relation.

Similar results were obtained by Gordon et al. (2000); their models show that the $A_{\rm UV}$–$F_{\rm FIR}/F_{\rm UV}$ relationship is valid for different assumptions on dust properties. The dispersion found by Gordon et al. (2000) is much smaller than in our simulations, but in their models all the stellar populations suffer the same extinction (i.e. no dependence on age is introduced).

Models also show that edge-on systems tend to follow a different relation from what is found for face-on systems; this is due to the greater contribution of the diffuse medium to attenuation in the direction of the plane of the galaxy.

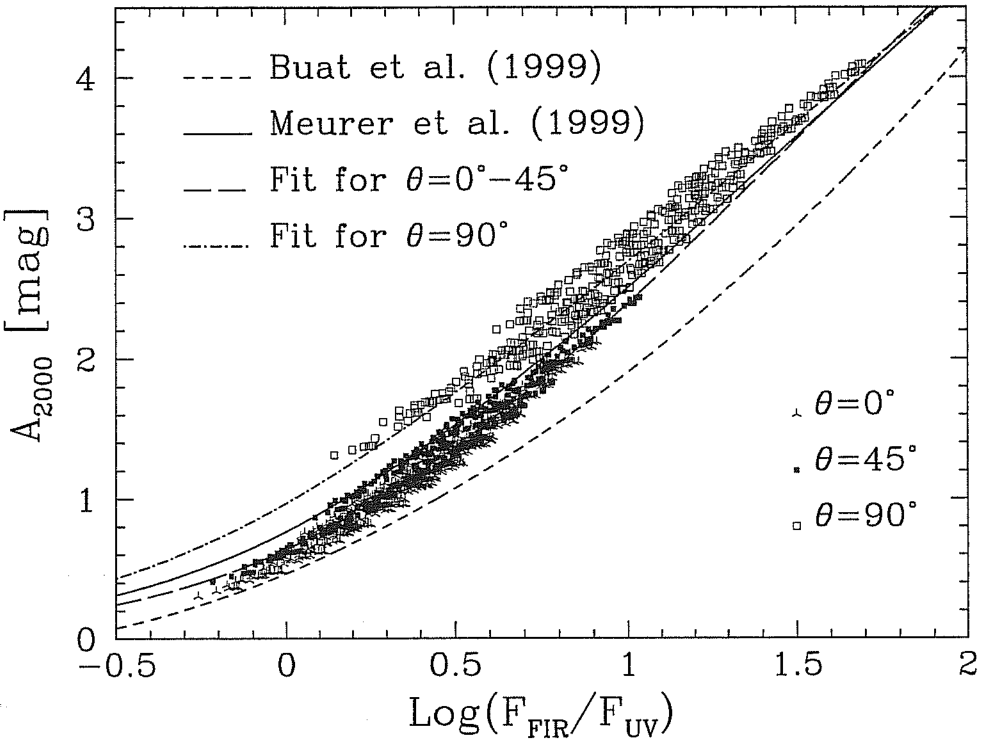

Figure 4.7: UV attenuation vs the ratio $F_{\rm FIR}/F_{\rm UV}$; lines refer to eq. 4.7, eq. 4.8 and our fits.

Our models suggest the following relation for face-on systems:

$$A_{2000} = 2.5 \log\left(\frac{F_{\rm FIR}}{1.25 F_{2000}} + 1\right) \ ; \tag{4.9}$$

while for edge-on systems it is preferable to use

$$A_{2000} = 2.03 \log\left(\frac{F_{\rm FIR}}{0.5 F_{2000}} + 1\right) \ . \tag{4.10}$$

In Fig. 4.7 we also compared the relations proposed by Meurer et al. (1999) (eq. 4.7) and by Buat et al. (1999) (eq. 4.8) with models. The former seems to better agree with our model, and lies between face-on and edge-on models, while the second tends to underestimate the UV attenuation (but only by 0.8 mag in the least favorable case).

4.4 Discussion

These galaxies exhibit a poor correlation between the attenuation in the UV band and Hα (B02, see also Fig. 4.5), with the former generally lower than what expected from the latter on the basis of the simple law $A_{\rm UV} = 1.6 A_{\rm H\alpha}$ (eq. 4.4). Our model explains this poor correlation in the context of age selective extinction. As the extinction in the UV is very high, the contribution to the observed UV flux from stars outside the molecular clouds is important even for relatively small optical thicknesses ($\tau_{\rm MC}$). It is worth noticing that the fraction of young UV emitting stars outside MCs increases for decreasing escape time, while very young stars (which ionize the gas) spend most of their life inside MCs. Therefore, above a threshold value for $\tau_{\rm MC}$ which depends on the escape time, an increase of $\tau_{\rm MC}$ produces an attenuation in Hα larger than that in UV.

Thus, neither observations nor modeling support the assumption of a constant relationship between the attenuation suffered by the continuum and the attenuation for the gas, at least for a current SFR smaller than 10 $M_\odot$/yr. As a consequence, the results of Calzetti (1997) ($A^{\rm stars}_{6563}/A^{\rm gas}_{\rm H\alpha} \sim 0.44$) cannot be extrapolated from starbursts to disk star-forming galaxies.

Moreover, the extrapolation of the Hα attenuation to the UV through the previous reported simple law yields UV corrected fluxes larger than those expected from Hα corrected fluxes, as found by Sullivan et al. (2000; 2001). These authors explain the result by introducing star formation histories that change rapidly with time and/or a more complex model of extinction. On the other hand, our model explains this result as a natural consequence of the age selective extinction.

An additional interesting issue is that the attenuation in Hα derived from the Balmer decrement can be underestimated, since in disk galaxies the escape time and the lifetime of very massive stars is often similar.

The comprehensive treatment of nebular and continuum emission allows to conclude that the assumption of a constant extinction for all stellar populations is not satisfactory. However, the detailed models presented in this work indicate that $A_{\rm UV}$ can be accurately estimated by using the ratio $F_{\rm FIR}/F_{\rm UV}$ (cfr. eqs. 4.9 and 4.10). This conclusion holds provided that the main contribution to FIR comes from the absorbed UV radiation of young stars, but it does not depend on the escape times and on the extinction properties of dust. The relationships we obtain are intermediate between those by Buat et al. (1999) and by Meurer et al. (1999), the latter derived for starburst galaxies.

Chapter 5

Attenuation in starburst galaxies

In this chapter we investigate on the properties of starburst galaxies, in particular we will sudy their exctinction properties and the relation between extinction and the UV spectral index. In Sect. 5.1 we introduce the general issue of starburst galaxies. Sect. 5.2 introduce the method proposed by Meurer et al. (1999) to estimate the dust attenuation from the UV spectral index. In Sect. 5.3 we analyze the sample of UV-bright starbursts by Wu et al. (2002), and in Sect. 5.4 compare the sample with our models. In Sect. 5.5 we study the UV, optical and IR properties of IR luminous starbursts. Finally, in Sect. 5.6 we summarize the main results of this chapter.

5.1 Introduction

The term *starburst* was introduced by Balzano (1983) to mark galaxies whose blue colors are the consequence of an enhanchement of the star formation activity. With the discovery of IR galaxies, the term starburst was also used for this new class of galaxies, even if they can have very red colors. After twenty years there are still many different definitions of what a starburst galaxy is and how it must look like.

The ratio between the current star formation rate (in the last 8 Myr) and the average past star formation rate, SFR/<SFR>, often referred to as the birthrate parameter (Kennicutt et al., 1994), is a useful parameter to measure the strength of the most recent burst. Its value is typically smaller than 1 for normal star forming galaxies (Kennicutt, 1998), while typical starbursts have birthrate parameter in the range 1–10 and possibly larger in the case of luminous infrared galaxies (Mayya et al., 2003).

On the other hand, starburst galaxies may have the potential to form stars for periods much longer than this. For example M 82, the prototype of a starburst, has sufficient amount of gas in order to sustain star formation for a few hundred million years.

Indeed, Kim et al. (1995) had found prominent Balmer absorption lines, typical indicators of relatively older stellar systems, to be common in starburst spectra. In recent years, there have been attempts to use the information contained in the absorption lines to derive the properties of one or more assumed older bursts in individual galaxies, e.g. NGC 7714 (Lancon et al., 2001) and NGC 7679 (Gu et al., 2001). Stellar populations of a few hundreds of million years have been inferred in these studies.

Star formation history of a starburst nucleus may also depend on the spatial scale under investigation. Observations of nearby starburst galaxies with the Hubble Space Telescope have resolved starburst nuclei into several tens, or in some cases, a few hundreds of compact clusters known as Super Star Clusters (SSCs) (O'Connell et al., 1995). SSCs show a considerable range in their colors, suggesting a spread in their ages. Typically SSCs are found in a region of a few hundred parsecs within the starburst nucleus. Regions with strong Balmer abosrption lines are found as far as 1 kpc from the currently active starburst site of M 82 (O'Connell & Mangano, 1978).

Furthermore, star-forming regions are always associated with dust, which has the effect of reddening the observed spectrum. The amount of reddening is traditionally determined by comparing the observed Balmer emission line ratios with those obtained by photoionization models (Osterbrock 1989), using the galactic reddening curve (e.g. Cardelli et al. 1989).

The interplay between age, spatial distribution and attenuation, the latter also being dependend on the environment, makes the analysis of these systems very complex.

For example, Calzetti et al. (1994) found the reddening curve for the nuclear regions to be flatter than that of the Milky Way in the ultraviolet with possible implications for differences in the dust properties. On the other hand, Granato et al. (2001) found that the different shape of the reddening curve could be due to an age-dependent extinction of star-forming regions, rather than to a significant difference in the dust grain properties. Thus, the starburst spectra could be modelled by using the galactic reddening curve, when each stellar population is allowed to have its own extinction.

In this chapter we will investigate on the properties of starburst galaxies taking advantage of our model that may combine different observables such as continuum emission line emission. In particular we will focus on the exctinction properties of starburst and their relation with the UV spectral index.

5.2 UV attenuation from the UV spectral index

The estimate of UV attenuation is an important issue for starbursts, specially for objects at high redshift. In fact, the UV rest-frame of galaxies at $z > 1$ is shifted in the optical, where observations are easier from the ground. Meurer et al. (1999, hereafter MHC99) studied the UV properties of local starbursts in order to derive a method to estimate A_{UV} in Lyman Break galaxies.

The sample of local starbusts used by MHC99 was built by choosing objects that were previously classified as starbusts on the basis of optical data. They had to have a compact morphology and/or strong emission lines, and no evidence of AGN. The second requisite for those galaxies was to have IUE UV spectra with reasonable quality. The catalog can not be considered statistically complete. For each galaxy in the sample Meurer and collaborators computed the spectral index β from IUE spectra in the region between 1500 and 2500 Å. In this region the flux f_λ can be well approximated by a power law $f_\lambda \propto \lambda^\beta$. The β index was obtained using the mean fluxes in 10 spectral bands (defined in Calzetti et al. 1994) in order to avoid stellar absorption features. Meurer and collaborators found that the index β correlate quite well with the ratio $F_{\rm FIR}/F_{1600}$. This relation can be converted into a relation between A_{1600} and β by using the previously derived equation 4.7. Then, with a linear fit they get:

$$A_{1600} = 4.43 + 1.99\beta \tag{5.1}$$

Considering the simple (and unrealistic) configuration of a dusty screen between stars and observer, the authors conclude that the slope of Eq. 5.1 ($\mathrm{d}A_{1600}/\mathrm{d}\beta = 1.99$) can be produced by an attenuation law similar to the one proposed by Calzetti (1997), while the Galactic extinction law is ruled out.

Since this method provides an estimate of $A_{\rm UV}$ using only rest-frame UV data, it has been widely applied to correct the UV luminosities of Lyman break galaxies and to estimate the cosmic star formation rate at high redshift (Steidel et al., 1999)

However, as we will discuss in Sect. 5.5, an important class of star-forming galaxies (namely the infrared luminous galaxies) does not follow this relationship.

5.3 UV-bright starburst sample

The sample of UV-bright starbursts used in MHC99 was enlarged by Wu et al. (2002, hereafter W02) and it is available on the web[1]. The sample consists of 83 starbursts selected from the availability of the IUE spectra; a fraction of them also have a spectrum in the optical region (45 objects), the fluxes in I, H, and K' bands and IR observations (IRAS plus some ISO data). The IUE data were re-calibrated with HST observations. Due to the extended coverage of SEDs, this sample is a unique chance to study the starburst population; thus we have done a deeper analysis of these data. However, it is worth to remember that there is no clear selection criteria (such as limiting flux or color) for this sample.

The spectra were corrected for the foreground extinction of the Galaxy with two different parameterizations of the extinction law and two different assumptions for the galactic dust distribution. Since results obtained adopting different assumptions are very similar, we have analyzed SEDs resulting from only one combination of dust distribution and extinction law. We chose the Schlegel-Finkbeiner-Davis system (Schlegel et al., 1998) for dust distribution and the CCM parameterization (Cardelli et al., 1989) of extinction law.

---

[1] URL: `http://morpheus.phys.lsu.edu/~starbrst/`

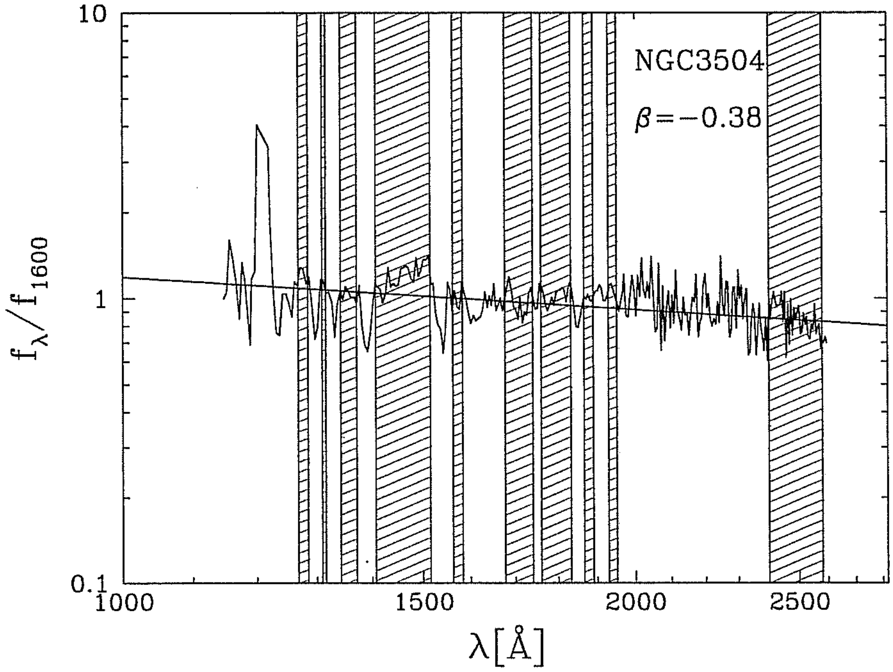

Figure 5.1: The UV spectrum of NGC 3504 compared with the linear (in log-log) fit. Shadowed regions show the 10 spectral bands defined by Calzetti et al. (1994).

For all the objects in the sample, we computed the UV spectral index following the Calzetti et al. (1994) recipe, in which β is computed through the linear fitting (in $\log(f_\lambda)$ vs $\log\lambda$) of the mean flux in 10 spectral bands between 1500 and 2500 Å. An example of the fitting is reported in figure 5.1, where the considered spectral bands are marked.

The computed β, together with the FIR luminosity (obtained from Helou's definition), the ratio $L_{\rm FIR}/L_{1600}$, the luminosity at 5550 Å($L_{\rm V} = 5550 \cdot L_{5550}$) and the UV spectra are reported in tables and figures in Appendix A.

We also computed the luminosity of several optical lines. The major problem in the computation is that Hβ is superimposed to the corresponding stellar absorption feature, while Hα is blended with [N II]6585 and [N II]6549. Thus, we performed a spectral fit of all components (stellar absorption with a Lorentzian plus a Gaussian emission in Hβ and three Gaussian for Hα+[N II]) in the two spectral regions. Also these results are reported in Appendix A.

5.3.1 The Meurer diagram for the W02 sample

The first analysis we have done is to reproduce the relation between $F_{\rm FIR}/F_{\rm UV}$ and β for this sample. Fig. 5.2 show the $F_{\rm FIR}/F_{\rm UV}$ vs β diagram (hereafter it will be called Meurer diagram) with the errors on β. Different symbols are used in different ranges of

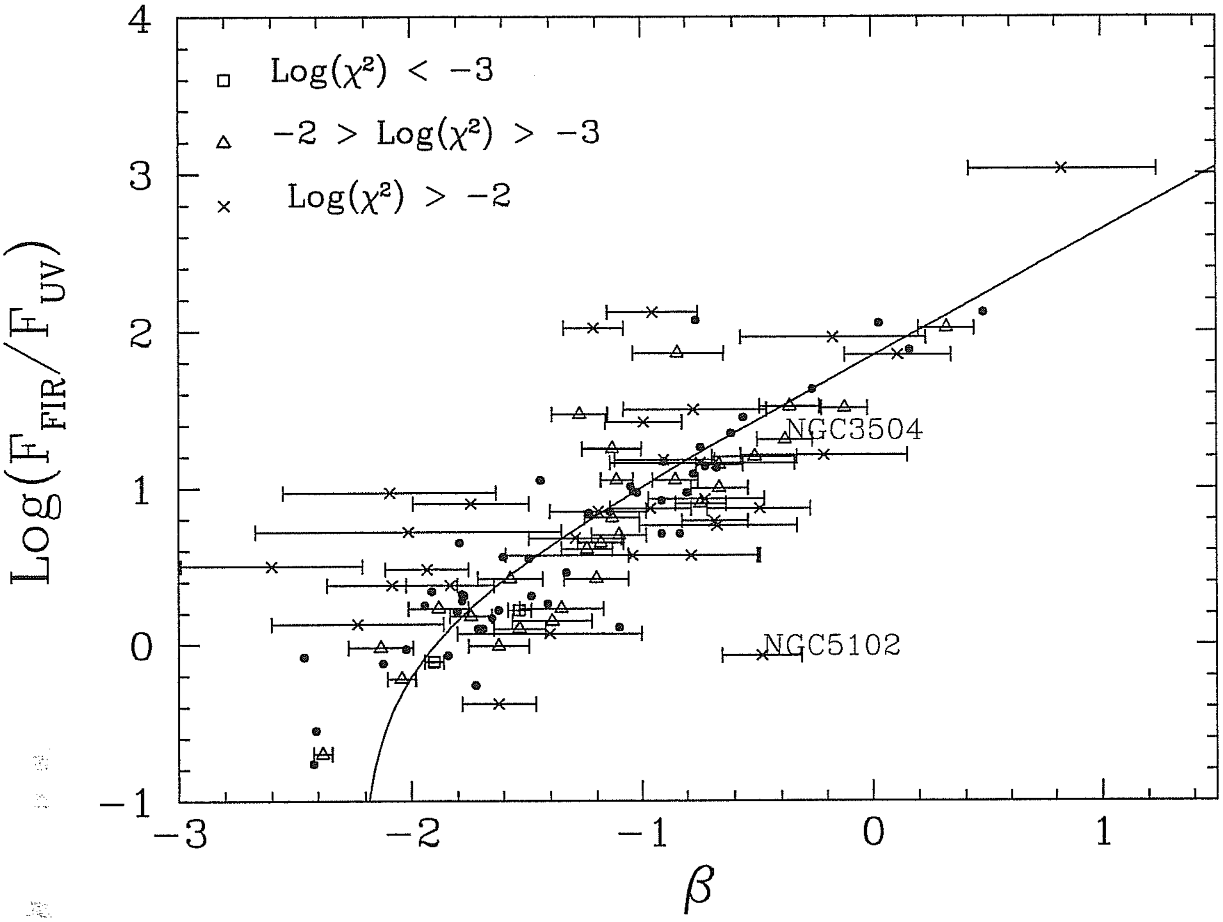

Figure 5.2: The ratio FIR/UV vs. β for the W02 sample. Different symbols (open squares, open triangles and crosses) refer to different quality of the power-law fitting of UV spectra; error bars show the statistical error on the β determination. Small filled circles are data published in MHC99, while the thick line shows the mean relationship provided by MHC99.

the χ^2 value of the fit[2].

The whole sample shows a larger scatter than the Meurer's one but if one select only galaxies with a low noise spectrum, the dispertion decreases. Moreover, the outline NGC5102 is not a starburst at all: from IR luminosity and optical spectrum, the SFR in this galaxy is near to zero.

In figure 5.3 we show the diagram $F_{\rm FIR}/F_{\rm UV}$ vs β with different symbols according to the FIR luminosity. There is no clear differentiation between galaxies with different FIR luminosity; only an expected trend of higher FIR/UV ratio for more luminous galaxies. This result is in keeping with the general observed correlation between SFR and attenuation. We also ranked the sample according to the equivalent width of Hα+[N II] (figure 5.4); but no differentiation is seen also in this case.

---

[2] $\chi^2 = \sum_{i=1}^{10}(\log f_i - \alpha - \beta \log \lambda_i)^2$ where f_i is the average flux in the spectral band at the wavelength λ_i, while α and β are the parameters resulting from the fit.

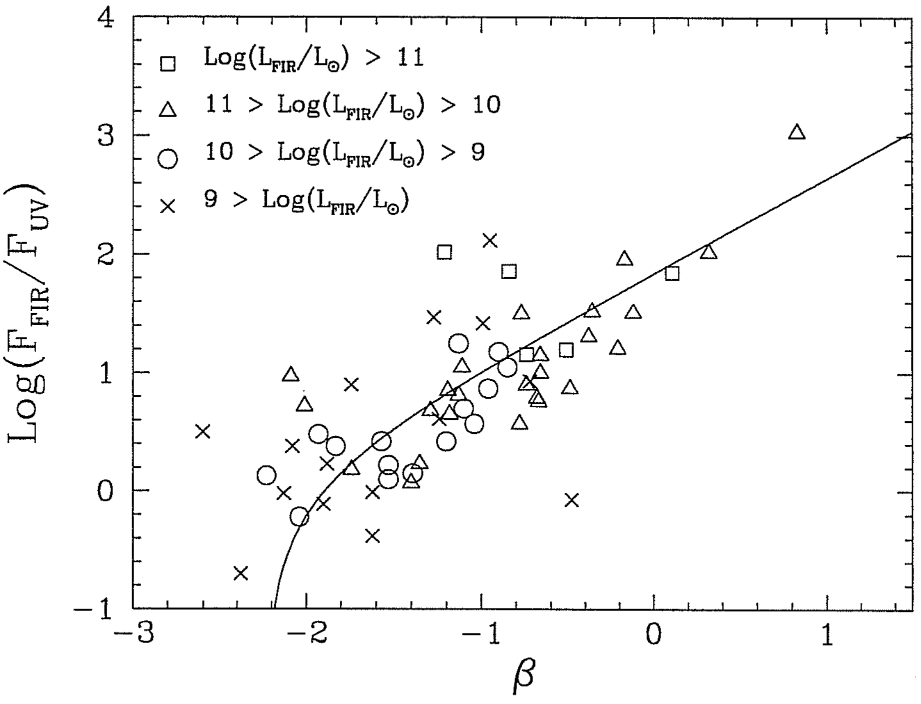

Figure 5.3: The ratio FIR/UV vs. β for the UV selected sample. Different symbols refere to different FIR luminosity.

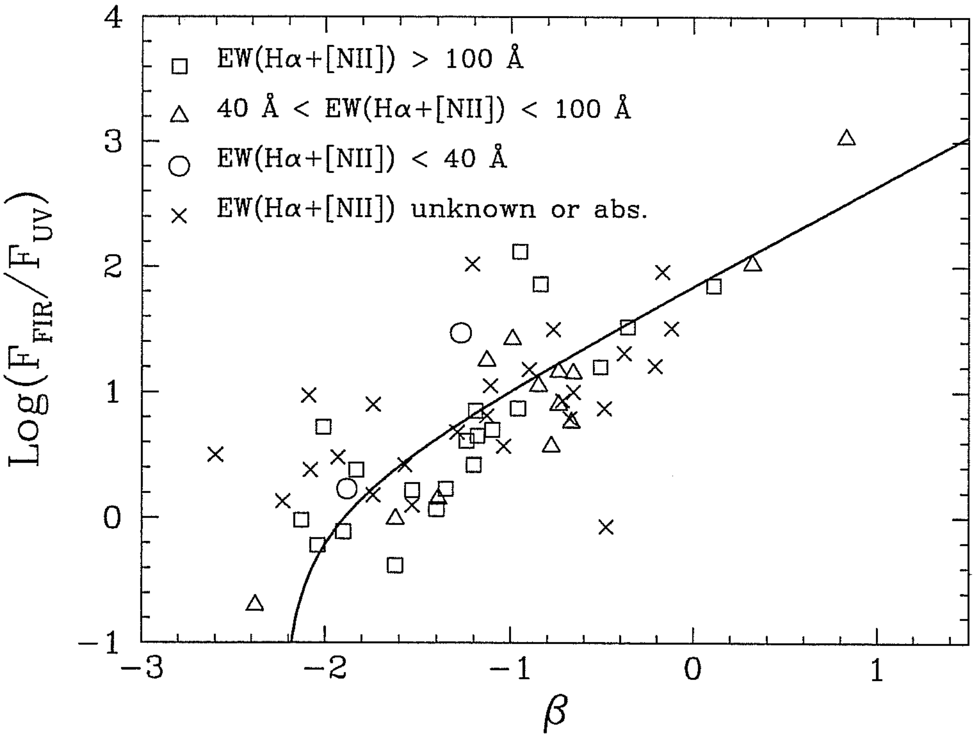

Figure 5.4: As in the previous figure but symbols are used for differencing in equivalent width of Hα+[N II].

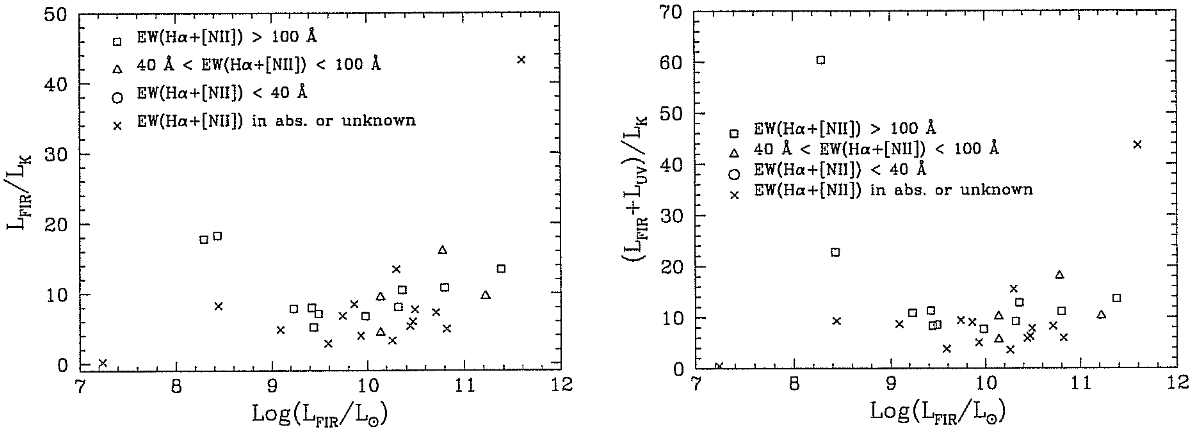

Figure 5.5: Left panel: the ratio FIR/K' vs the FIR luminosity for the W02 sample. Right panel: the ratio (FIR+UV)/K' vs the FIR luminosity.

An interesting test on the bursting nature of these objects can be done by looking at the ratios FIR/K' and (FIR+UV)/K'. In fact, these quantities measure the ratio between the current SFR and the underlying old population. In normal star-forming galaxies this ratio has a value around 1. In fig. 5.5 it can be noted that almost all the galaxies in the sample have an important enhancement of SFR, but only in a few cases the old population is very small. Data show also a trend of increasing FIR/K' with FIR luminosity. As expected from the observed optical spectrum, the galaxy NGC5102 have a (FIR+UV)/K' near to zero, corresponding to passive evolution.

Figure 5.6, where we contrast the ratio FIR/V versus the FIR luminosity, confirms a trend of increasing dust obscuration with FIR luminosity. All galaxies have a FIR/V ratio smaller than 35; this value is considerably smaller than that found (FIR/V $\sim$ 90) by Poggianti et al. (2000) for Very Luminous InfraRed Galaxies (see Sect. 5.5 for the definition). This result points out that the UV selected starbursts represent a fraction of the starburst population, accounting only for the less obscured objects.

5.3.2 The attenuation of stellar continuum and the Balmer decrement

In figure 5.7 we reproduced the relation between the attenuation from the ratio FIR/UV (eq. 4.7) and the attenuation suffered by the gas, as computed by the Balmer decrement (eq. 4.3). The two quantities correlate quite well but there are some outliners. The results are similar to what obtained by B02. The linear relation in the figure shows the expected relation between the two quantities as discussed in sect. 4.3. In this case the UV luminosity is computed at $\lambda_{\rm UV} = 1600$ Å so that eq. 4.4 becomes $A_{\rm UV}({\rm FIR/UV}) = 1.78 A_{\rm H\alpha}$. The presence of a correlation between the two quantities suggests that UV, FIR and Hα are mainly produced by the same stellar population.

It is worth noticing that this result is very different from what found for normal

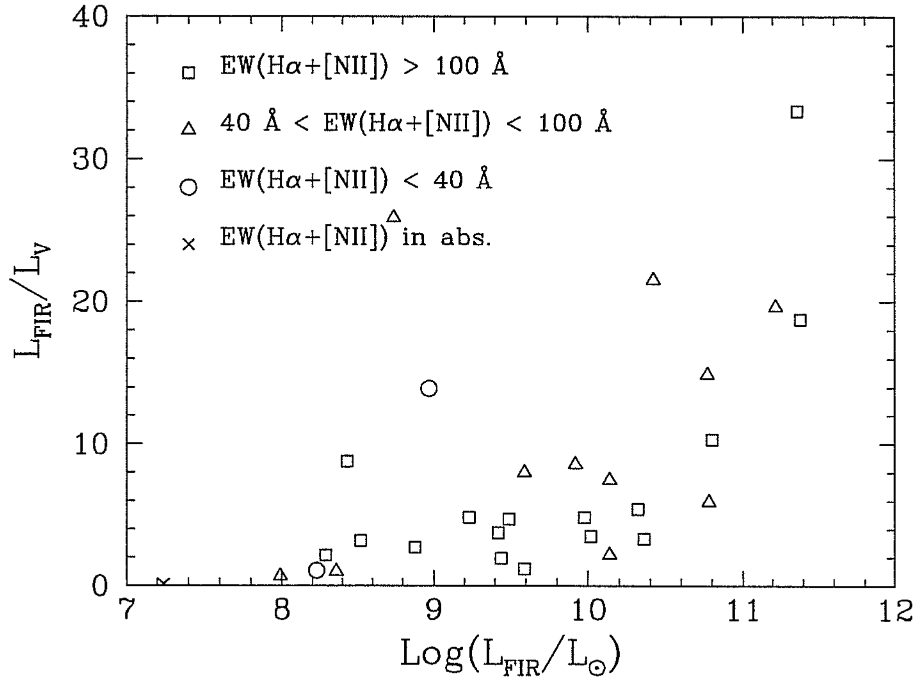

Figure 5.6: The ratio FIR/V vs the FIR luminosity for the W02 sample.

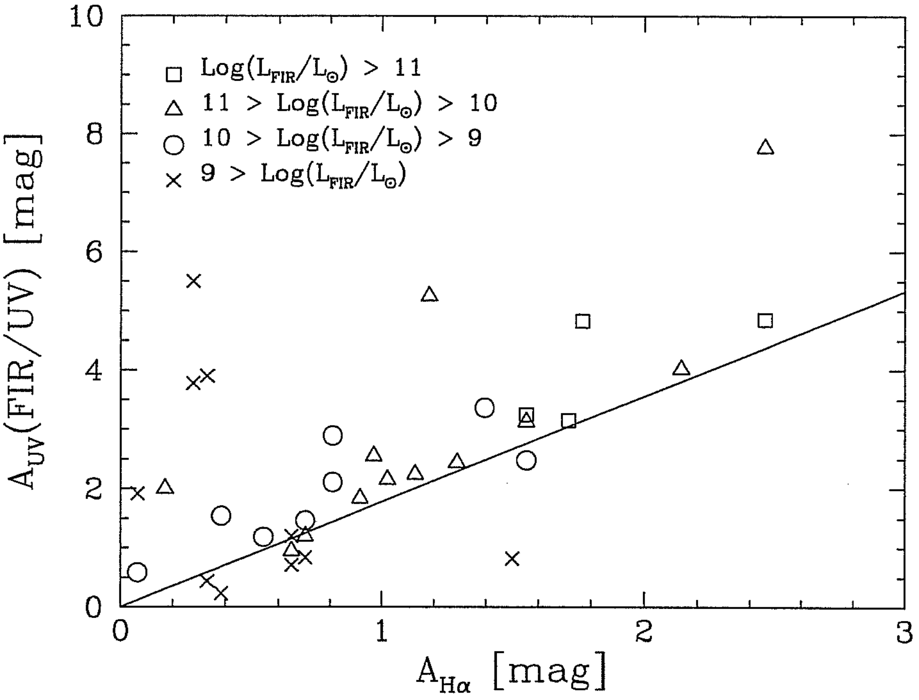

Figure 5.7: The comparison between the attenuation at 1600 Å derived from equation 4.7 versus the attenuation in Hα derived from the Balmer decrement in the sample of W02. Galaxies are represented with different symbols according to their FIR luminosity.

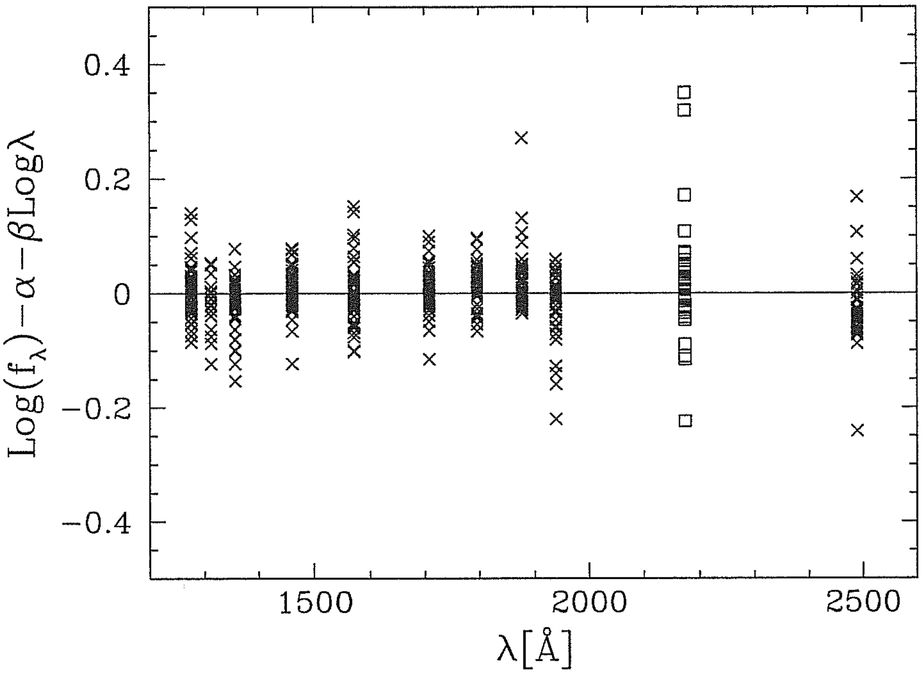

Figure 5.8: The residuals $d_\lambda = \log f_\lambda - \alpha - \beta \log \lambda$ from the fitting of UV spectra for galaxies with $\beta > -1.5$ versus the wavelength in the 10 spectral bands (crosses) and around 2175 Å (empty squares).

star-forming galaxies, as discussed in Sect. 4.3.

5.3.3 The 2175 Å dust absorption feature

It is worth noticing that the galaxies in the sample do not show an evident dust absorption around 2175 Å; some of them show an emission in the same place due to an overestimate of foreground extinction. As an example, the galaxy NGC 3504, which is one of the redder objects in the sample with a low-noise spectrum, does not show (see fig. 5.1) any evidence of the dust absorption feature.

In order to verify if the absorption feature is actually present in the UV-bright starbursts, we plotted the differences between the observed flux and the result of the fitting of the spectral index for each galaxy in the sample. Fig. 5.8 contrasts the differences $d_\lambda = \log f_\lambda - \alpha - \beta \log \lambda$ versus the wavelength in the 10 spectral bands (crosses) used for the fit and around 2175 Å (empty squares), for galaxies with $\beta > -1.5$. If the dust absorption feature would be present, the majority of the points at $\lambda = 2175$ Å in the figure should have $d_\lambda < 0$; on the contrary, their distribution is centered at $d_\lambda = 0$.

Let's now estimate which value of d_λ would be found at 2175 Å if the absorption bump was present. Assuming that the stellar emission f^*_λ is well represented by a power-law ($\log f^*_\lambda = \alpha_0 + \beta_0 \log \lambda$), an attenuation law that preserves the power law shape in the attenuated spectrum must have the form $\tau_\lambda = A - B\log\lambda$. In fact, in this case we get that the observed flux f_λ is:

$$\begin{aligned} \log f_\lambda &= \log\left(f_\lambda^* e^{-\tau_\lambda}\right) = \log f_\lambda^* - \tau_\lambda \log(e) \\ &= \alpha_0 + \beta_0 \log\lambda - \log(e)(A - B\log\lambda) \\ &= (\alpha_0 - A\log(e)) + (\beta_0 + B\log(e))\log\lambda \end{aligned} \tag{5.2}$$

then, the observed spectral index is $\beta = \beta_0 + B\log(e)$. Equation 5.1 can be written in term of τ_{1600}: $\beta = \beta_0 + 1.086\tau_{1600}/1.99$, so we get:

$$B\log(e) = \frac{1.086}{1.99}\tau_{1600} \Rightarrow B = 1.256\tau_{1600} \tag{5.3}$$

Using the latter in the definition of A and B at 1600 Å, we get $A = 5.024\tau_{1600}$. So, we determined an attenuation law that preserve the power law shape of attenuated flux and is compatible with equation 5.1.

The optical depth expected from this law at 2175 Å is $\tau_{2175} = 0.832\tau_{1600}$; in presence of a bump at 2175 Å the latter would be $\tau_{2175} = (1+\epsilon)0.832\tau_{1600}$. Then the corresponding residual d_λ would be:

$$\begin{aligned} d_{2175} &= \log f_{2175} - \alpha - \beta\log\lambda = -\tau_{2175}\log(e) + 0.832\tau_{1600}\log(e) \\ &= -\epsilon 0.832\tau_{1600}\log(e) = -0.36\epsilon\tau_{1600} \end{aligned} \tag{5.4}$$

In figure 5.8 we have considered only objects with $\beta \geq -1.5$ that corresponds to $\tau_{1600} \geq 1.445$, so, from equation 5.5 we get $d_{2175} \leq -0.52\epsilon$. It can be noted in the figure that, apart from three objects, d_{2175} is smaller than -0.1, that means $\epsilon < 0.19$ and $\tau_{2175} < 0.992\tau_{1600}$. Comparing the last result with the galactic extinction law in which $\tau_{2175} \simeq 1.35\tau_{1600}$, we can conclude that the attenuation law in starbursts of the W02 sample has no bump or a negligible one at 2175 Å. This is in good agreement with what found by Calzetti and collaborators in several works (Calzetti et al., 1994; Calzetti, 1997; Calzetti & Heckman, 1999). Indeed, Calzetti and collaborators analyzed the IUE spectra of starbursts from Kinney et al. (1993) with a simple model (i.e. without age selective extinction) for dust reprocessing of star light and derived a mean attenuation law (thereafter called Calzetti's law) that does not show the presence of the 2175 Å dust absorption bump.

5.4 Simulated UV-bright starbursts

For a better analysis of the UV-bright starbursts, we have done a set of simulations of bursting galaxies.

The simulated galaxies are assumed to form stars in a smooth way during all their history, plus a final analytical burst starting at the age $t_0 = 10$ Gyr. The star formation history in the first 10 Gyr is computed assuming a linear Schmidt law with a gas infall timescale $\tau_{\rm inf} = 12$ Gyr and a star formation efficiency $\nu_{\rm sch} = 0.3$ Gyr^{-1}. Two values were assumed for the total baryonic mass at t_0: $M_{\rm G} = 0.5 \cdot 10^{10}$ M$_\odot$ and 10^{10} M$_\odot$. The adopted IMF is a Salpeter one between $m_{\rm inf} = 0.15$ M$_\odot$ and $m_{\rm up} = 125$ M$_\odot$. It results a SFR around 0.5 and 1 M$_\odot$/yr (respectively for $M_{\rm G} = 0.5 \cdot 10^{10}$ M$_\odot$ and 10^{10} M$_\odot$) just before the switching on of the burst. The total gas mass $M_{\rm gas}$ available at that time is 1.5 and $3 \cdot 10^9$ M$_\odot$ for the two bayonic masses. During the burst, a fraction $f_{\rm gas}$ of the mass of gas present before is converted into stars.

The burst is assumed to have a star formation activity exponentially decaying; so that the star formation rate Ψ during the burst is given by the law

$$\Psi_{\rm burst}(T) = \frac{f_{\rm gas} M_{\rm gas}}{t_{\rm b}} \cdot \exp\left(-\frac{T - t_0}{t_{\rm b}}\right) \tag{5.5}$$

where $t_{\rm b}$ is the e-folding time of the burst and T is the age of the galaxy.

We assumed that the gas converted in stars is in molecular form, so that during the burst the fraction of molecular gas decreases, while the gas in diffuse medium is constant. Moreover, the number of MCs during the burst was fixed, so that the MCs become more and more transparent as the gas is consumed. If $m_{\rm MC,0}$ is the initial mass of MCs, the mass during the burst is given by:

$$m_{\rm MC}(T) = m_{\rm MC,0} \left[\frac{f_{\rm MC} - f_{\rm gas}}{f_{\rm MC}} + \frac{f_{\rm gas}}{f_{\rm MC} t_{\rm b}} \exp\left(-\frac{T - t_0}{t_{\rm b}}\right)\right] . \tag{5.6}$$

As a consequence, the optical thickness of MCs, that is proportional to $m_{\rm MC}/r_{\rm MC}^2$ (Sect. 3.2), with $r_{\rm MC}$ being the MC radius, decays in the same way, being $r_{\rm MC}$ assumed constant during the burst.

We have assumed that newly born stars remain within the parent molecular cloud for a time longer than that assumed in normal galaxies. Furthermore, stars older than the burst are supposed to be escaped by MCs. So, the escaping time $\tau_{\rm esc}$ in our simulation increases from a minimum value $\tau_{\rm min}$ as the burst continues: $\tau_{\rm esc} = \tau_{\rm min} + (T - t_0)$.

The geometry chosen was the spheroidal one, since starbursts tend to occur in the nuclei regions and/or to have a complex geometry. The metallicity during the burst was set to be solar.

We considered two different cases whose parameters are reported in table 5.1. Model A was built to reproduce objects with a low obscuration, while model B is for more obscured galaxies.

The resulting SEDs were computed at different times, starting from 2 and 4 Myr after t_0 (respectively for models A and B), at constant time intervals (2 Myr for model A and 4 Myr for model B), until an age of 58 Myr for model A and 118 Myr for model B.

Table 5.1: The adopted value of GRASIL parameters for the different models.

Parameter	Model A	Model B
M_{G}	$0.5 \cdot 10^{10}$ $\mathrm{M}_{\odot}$	10^{10} $\mathrm{M}_{\odot}$
f_{gas}	5%	10%
τ_{min}	4 Myr	30 Myr
τ_{b}	10 Myr	20 Myr
f_{MC}	10%	15%
$m_{\mathrm{MC,0}}/r_{\mathrm{MC}}^2$	120, 60, 30, 7.5 $\mathrm{M}_{\odot}/\mathrm{pc}^2$	60, 120, 160, 250 $\mathrm{M}_{\odot}/\mathrm{pc}^2$
r_{c}^{*}	0.3 kpc	0.3 kpc
$r_{\mathrm{c}}^{\mathrm{d}}$	0.5 kpc	0.5 kpc

5.4.1 The Meurer diagram

Figure 5.9 and 5.10 show the time evolution of simulated starbursts, on the Meurer diagram, compared with the W02 sample. The different patterns correspond to different choices of the initial value of MCs optical depth. The models evolve from the bluer (more negative values of β) toward redder colors, starting from an age of 2 Myr after the beginning of the burst, to an age of 58 Myr. After that, the galaxies evolve passively toward more redder β.

It is worth noting that models follow the observed correlation between FIR/UV and β, and the observed values of Hα equivalent width. However, the ultraviolet spectral index β in the more active phase is bluer ($\Delta\beta \sim -0.5$) than for the observed objects.

Analysing the causes of this discrepancy, we have found that an important contribution is due to the presence of the 2175 Å bump in the extinction law of the dust mixture used in our models. In fact if we neglet the region around the bump (the spectral windows above 1800 Å) in the fitting of the model spectral slope we generally find a redder value of β.

Interestingly, the spectral slope of the models with the lower extinction is steeper (bluer) than that predicted by the dust free case in eq. 5.1, namely $\beta_0 \simeq -2.2$. This suggests that observed starbursts could have stellar populations intrinsically redder than our models, eventually due to a different IMF.

5.4.2 The attenuation law

Figure 5.11 compares the attenuation curves for simulated galaxies with the attenuation law from Calzetti et al. (1994) and the galactic extinction law. The attenuation law A_λ in simulated galaxies is defined as the difference in magnitudes of the stellar luminosity L_λ with and without dust. All curves are normalized to unity at $\lambda = 1600$ Å.

It has to be noted that, even if the grain properties used in our model reproduce the galactic extinction law, the obtained attenuation laws show a weaker 2175 Å bump, in between the Calzetti law and the galactic one. This is a consequence of the age

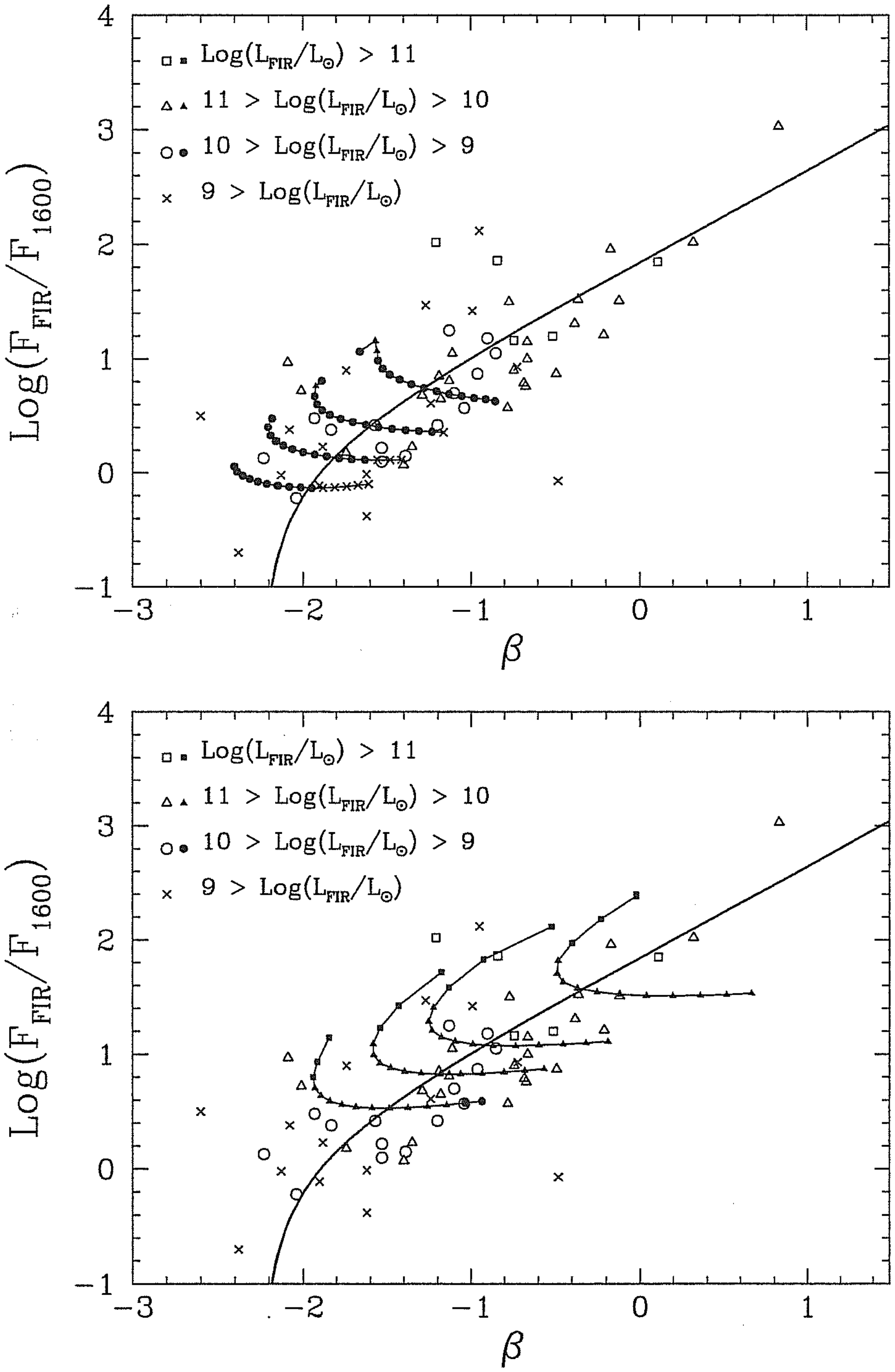

Figure 5.9: The FIR/UV vs the UV spectral index for observed UV-bright galaxies and simulated one (upper panel: model A; lower panel: model B). The time evolution of simulated starbursts is shown as connected symbols at uniform spaced times. Models evolve from bluer β (on the left) toward redder values. Different symbols show the FIR luminosity of the models during the evolution and that of the observed galaxies.

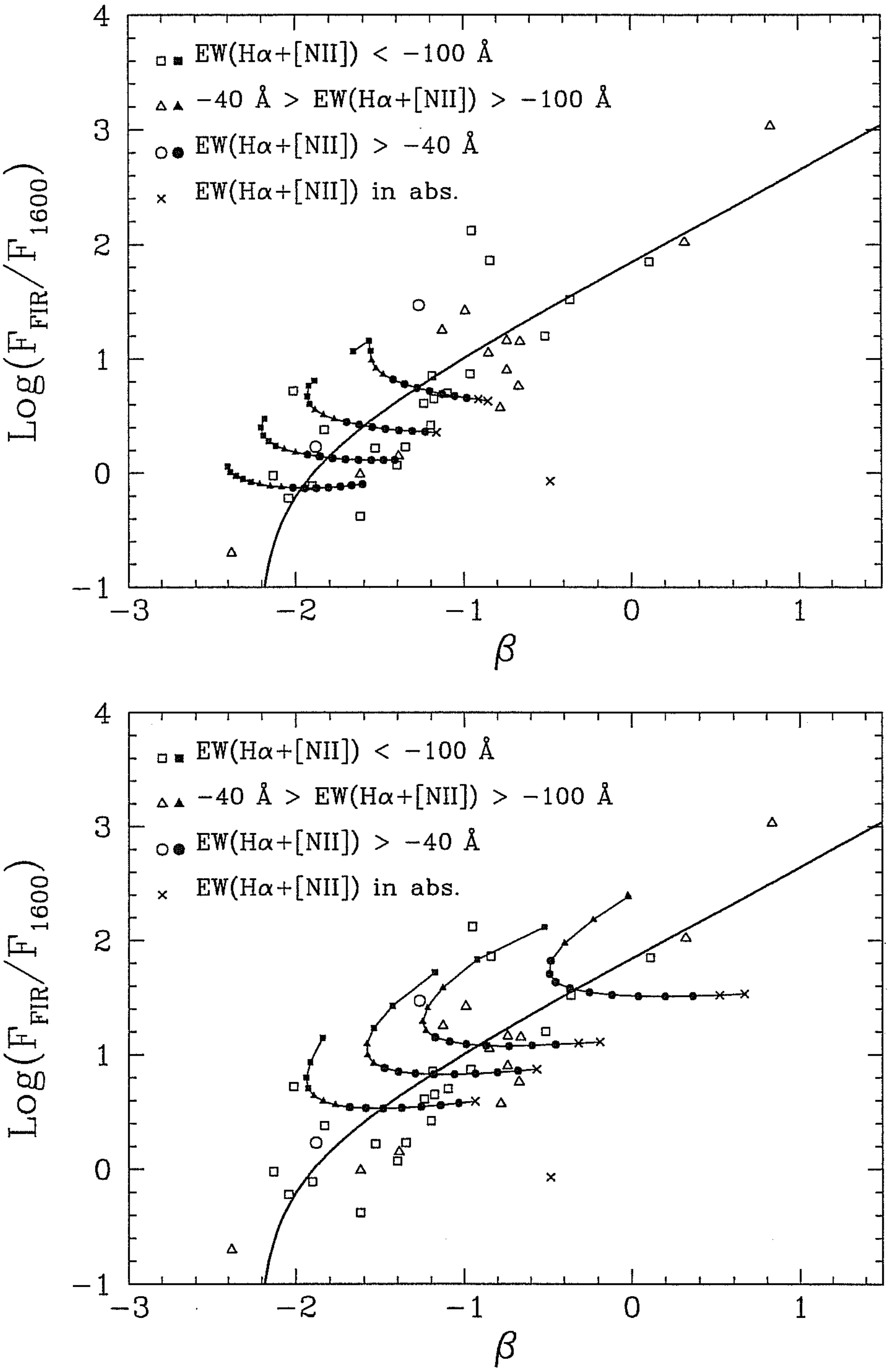

Figure 5.10: The FIR/UV vs the UV spectral index for simulated and observed UV bright galaxies as in fig. 5.9. Different symbols show the equivalent width of Hα+[Ne II] of the models in the case A (upper panel) and in the case B (lower panel) during the evolution (connected symbols) and of the observed galaxies.

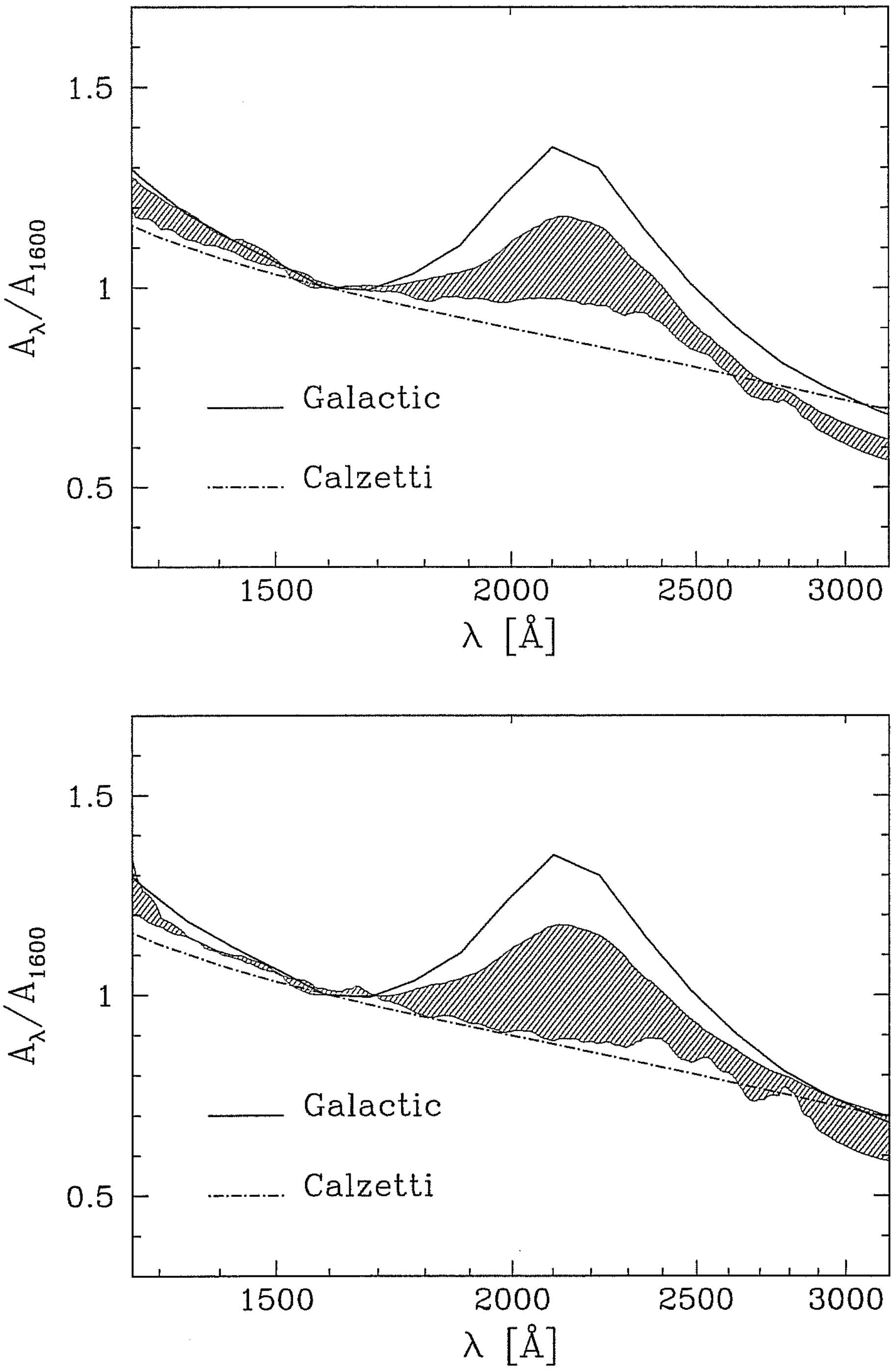

Figure 5.11: The attenuation curve of simulated UV bright galaxies. The thick continue line show the galactic extinction law, while the dot-dashed line refer to the Calzetti attenuation law. The shadowed region show the variation of the attenuation A_λ of the models. Upper panel: model A, lower panel: model B.

selective extinction. In fact, as the optical depth of MCs increases, a growing fraction of the observed UV is produced by the older stellar population from outside MCs; this emission can fill the absorption feature in the SED of young population.

Figure 5.12 shows the comparison between the attenuation at 1600 Å from the ratio FIR/UV (using equation 4.7) and the attenuation at Hα from the Balmer decrement (eq. 4.3). The models reproduce the observed correlation quite well even if the data show a slightly large dispersion.

Finally, we compared the A_{1600} directly extracted from the models and the ratio $F_{\rm FIR}/F_{1600}$. As expected, the correlation is very strong and the dispersion of the models is small. This result can be compared with the analogous one for normal galaxies in Sect. 4.3.3, where the dispersion is much larger. In fact, in the starburst case the contribution of old stars to dust luminosity is near to zero. The residual dispersion in the diagram is due to the variation of dust SED among the models; this variation can be attributed to the different dust temperatures and optical thickness of MCs.

5.5 IR luminous starbursts

An important class of starburst galaxies are the infrared galaxies, whose principal characteristic is to emit almost all their luminosity in the infrared.

At luminosities above $10^{11}L_{\odot}$, infrared galaxies become the dominant (in number) population of extragalactic objects in the low redshift ($z < 0.3$) universe (Sanders & Mirabel, 1996). The trigger for the intense infrared emission appears to be the strong interaction (or merger) of gas-rich galaxies, and the bulk of the infrared luminosity for all but the most luminous objects is due to the dust heating of an intense starburst (Genzel et al., 1998). At the highest luminosities ($L_{\rm IR} > 10^{12}L_{\odot}$) these galaxies appear to be powered by a mixture of starburst and active galactic nucleus, the latter becoming predominant as the luminosity increases (Kim et al., 1995; Sanders & Mirabel, 1996).

Note that the IR luminosity refers to the total dust emission from 8 to 1000 μm, as estimated by the four IRAS bands (Sanders & Mirabel, 1996): $L_{\rm IR} = 0.971 \cdot L_{12}\nu_{12} + 0.775 \cdot L_{25}\nu_{25} + 0.929 \cdot L_{60}\nu_{60} + 0.6 \cdot L_{100}\nu_{100}$. This definition differs from the FIR definition used in the previous sections, where the considered spectral interval is from 40 to 120 μm. As a consequence, the FIR luminosity is a fraction of the IR one, and for starbursts $L_{\rm IR} \sim 1.75 \cdot L_{\rm FIR}$ (Calzetti et al., 2000).

Infrared galaxies are commonly classified on the ground of their IR luminosity. The IR galaxies are divided in: Luminous IR Galaxies (LIRGs) with $L_{\rm IR} \geq 10^{11}L_{\odot}$, Very Luminous IR Galaxies (VLIRGs) with $L_{\rm IR} \geq 10^{11.5}L_{\odot}$ and Ultra Luminous IR Galaxies (ULIRGs or ULIGs) with $L_{\rm IR} \geq 10^{12}L_{\odot}$. Objects with $L_{\rm IR} \geq 10^{13}L_{\odot}$ are sometimes called Hyper Luminous IR Galaxies; these extreme and rare[3] objects are almost always produced by powerful AGNs (Soifer et al., 1995; Evans et al., 1998).

---

[3] No HyLIG is present in the local universe; the few known objects are at redshift $z \geq 1$.

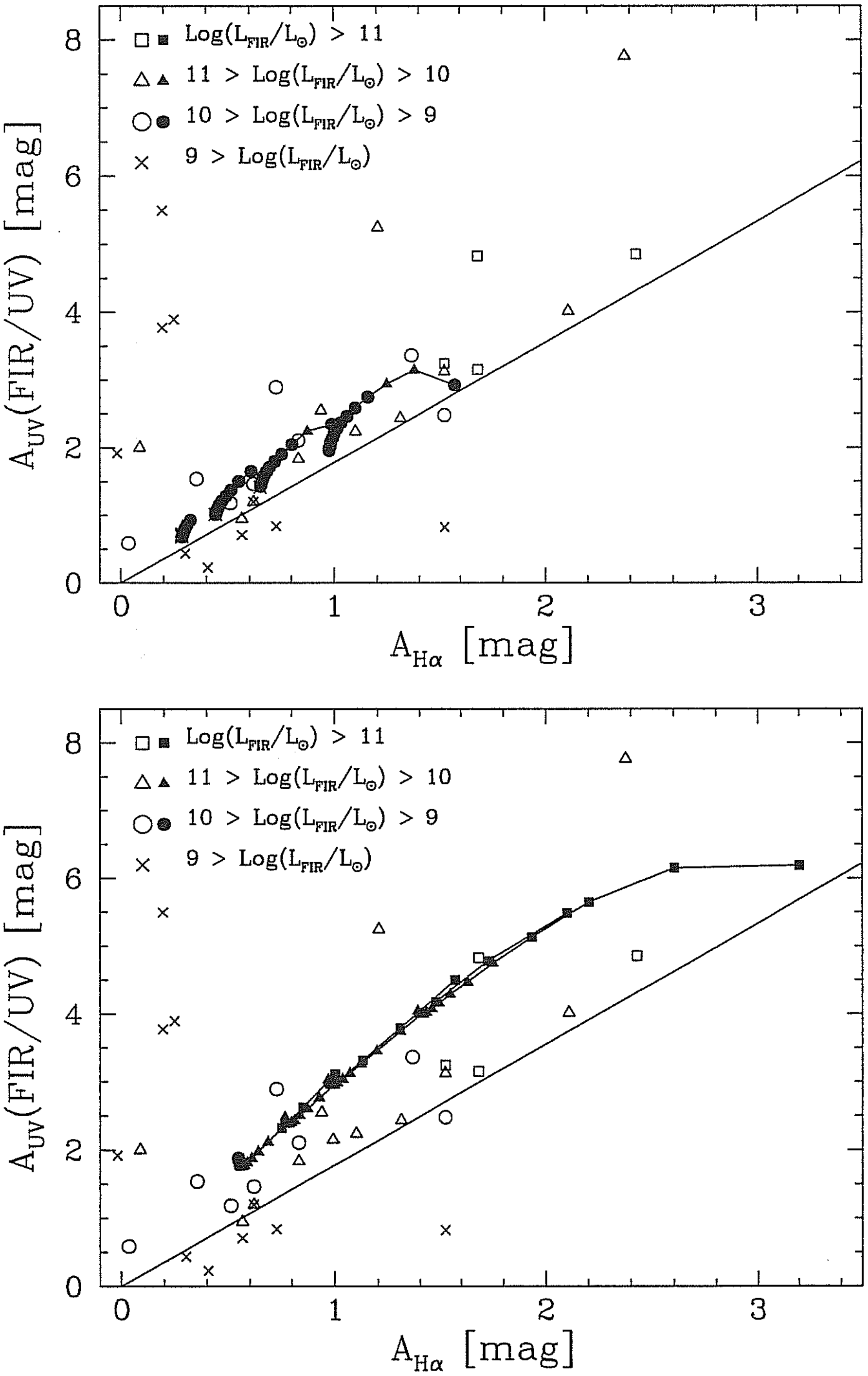

Figure 5.12: The comparison between A_{1600} derived from the FIR/UV ratio versus the attenuation in Hα derived from the Balmer decrement. Galaxies of W02 sample are represented with different symbols according to their FIR luminosity; connected symbols show the time evolution of models of the case A (upper panel) and the case B (lower panel).

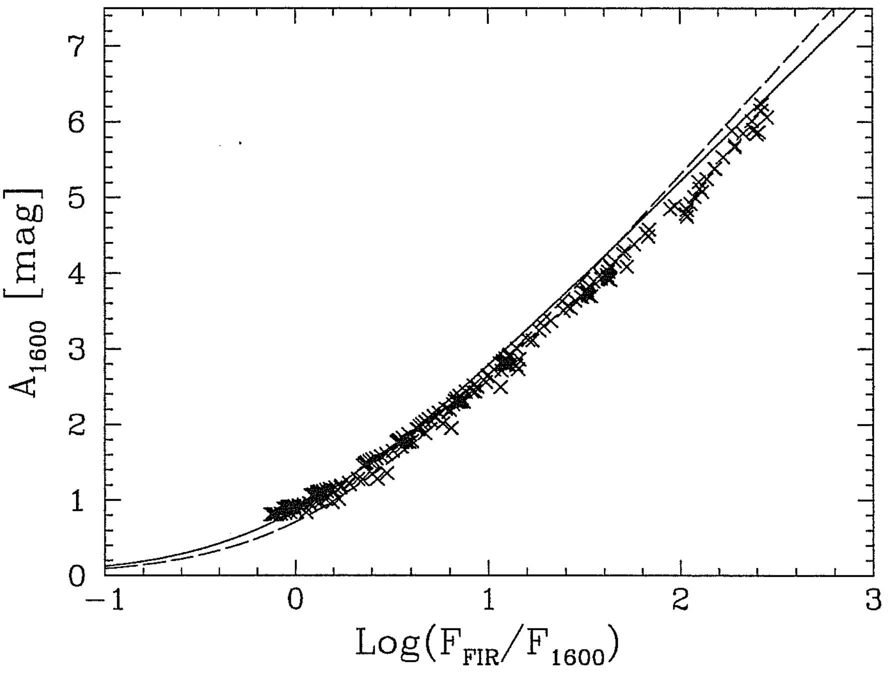

Figure 5.13: The comparison between real A_{1600} derived from the models and the ratio $F_{\rm FIR}/F_{1600}$ in simulated starburst (crosses). The solid line shows the relation derived by MHC99 (eq. 4.7), while the dashed line is the relation that we derived for normal galaxies (eq. 4.9) assuming $A_{1600} = A_{2000}/0.9$.

Infrared galaxies are likely to become more common at higher redshifts where the number of mergers and interaction is much higher. Moreover, these galaxies are possibly linked with high redshift sub-mm galaxies, even if sub-mm galaxies seem to have larger SFR and IR luminosities.

Unfortunately, even if IR galaxies are an important population, they are poorly studied in the UV domain. Recently, Goldader et al. (2002) published their observations with the Hubble Space Telescope of seven galaxies with L_{IR} between $10^{11.5}$ and $10^{12.2} L_{\odot}$. Three main results are worth being underlined:

- The peak(s) of UV emission are not spatially superimposed to the peak of IR emission. This displacement is typically some hundred of parsecs, and only a small fraction of UV light is emitted in the IR bright region.
- All the observed galaxies are faint in the UV. If placed at higher redshifts they could be detected in a HDF-like[4] survey up to $z \sim 1.5$, but undetectable at $z \sim 3$, where Lyman Break Galaxies are observed. Moreover, their sub-mm luminosity would be too small if compared to SCUBA galaxies observed at the same redshift.
- The observed galaxies do not follow the relation FIR/UV vs. β observed in UV-bright starbursts; they show a FIR/UV larger by one or two orders of magnitude than what expected by the UV spectral index.

5.5.1 Simulated IR luminous galaxies

Similarly to what was done in Sect. 5.4, we have simulated with our code some starburst galaxies to be compared with observations.

In this case, the total baryonic mass of the galaxy is $M_{\mathrm{G}} = 2.5 \cdot 10^{10}$, and the gas fraction f_{gas} converted in stars during the burst is much higher and corresponds to 80% of the total gas mass present in the galaxy before the burst. We also assume that $f_{\mathrm{MC}} = f_{\mathrm{gas}}$. The computations were done for three different e-folding time of the burst: $t_{\mathrm{b}} = 10, 20, 50$ Myr. In figure 5.14 the star formation rates of the simulated starbursts are shown during the burst.

The initial optical depth of these models is higher than in the UV-bright simulation; in this case we have $m_{\mathrm{MC,0}}/r_{\mathrm{MC}}^2 = 400\ \mathrm{M}_{\odot}/\mathrm{pc}^2$.

5.5.2 The Meurer diagram of VLIRGs

Figures 5.15 and 5.16 show the time evolution of our models for IR luminous galaxies. The three patterns correspond to the different assumptions on the e-folding time t_{b}. The models are able to reproduce the position of VLIRGs galaxies observed by Goldarer et al. (2002) and of the three galaxies of similar luminosity we found in the W02 sample.

---

[4] Hubble Deep Field: HDF north and south are very deep observations by the Hubble Space Telescope.

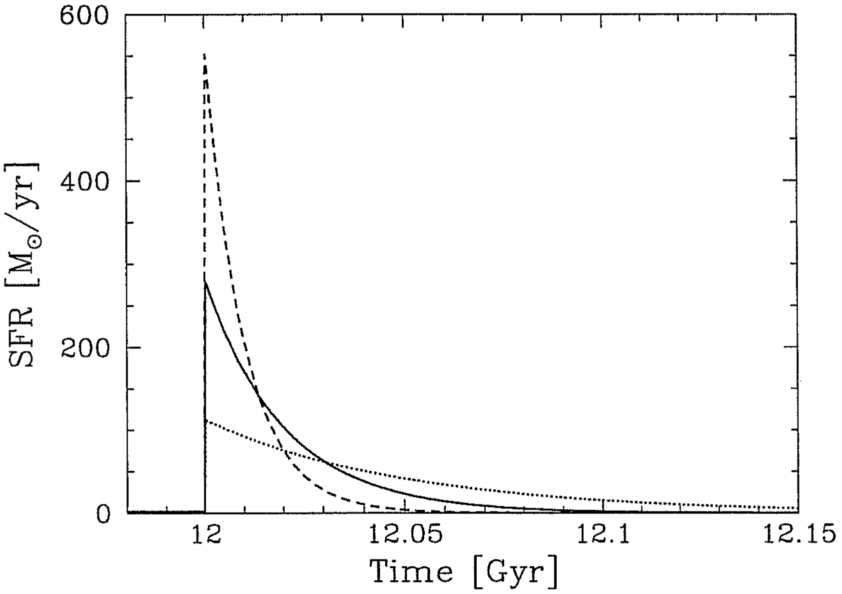

Figure 5.14: The star formation rate during the burst of simulated IR luminous galaxies. Different lines refer to different e-folding times: dashed for t_b = 10 Myr, continue line for t_b = 20 Myr and dotted for t_b = 50 Myr.

It is worth noticing that all models follow a similar pattern in which we can identify three phases:

1. The obscured phase: when the age of the burst is smaller than t_b, the burst is heavily obscured. The UV emission of the burst is almost completely absorbed by dust, and what is seen in the UV band comes from older (i.e. formed before the burst) stellar population. In this phase the ratio FIR/UV is essentially a measure of the ratio between the burst luminosity and the UV luminosity of older stars. Another consequence is that the observed UV spectral index is determined by the older population and does not measure the attenuation of the burst population.

2. The UV-bright phase: after an age of t_b, the burst has consumed an important fraction of the gas and MCs become more transparent. The UV from the burst population is less obscured and becomes predominant so that the galaxy falls on the Meurer relation.

3. The passive phase: when all the molecular gas is consumed and the SFR goes to zero, the galaxy evolves passively. The stellar spectra become redder and the objects leave the Meurer relation. This phase lasts until new gas is cooled and becomes available for the star forming activity.

This scheme could suggest the interpretation of the UV-bright sequence as an evolutionary pattern and of the UV-bright starbursts as product of evolved IR luminous

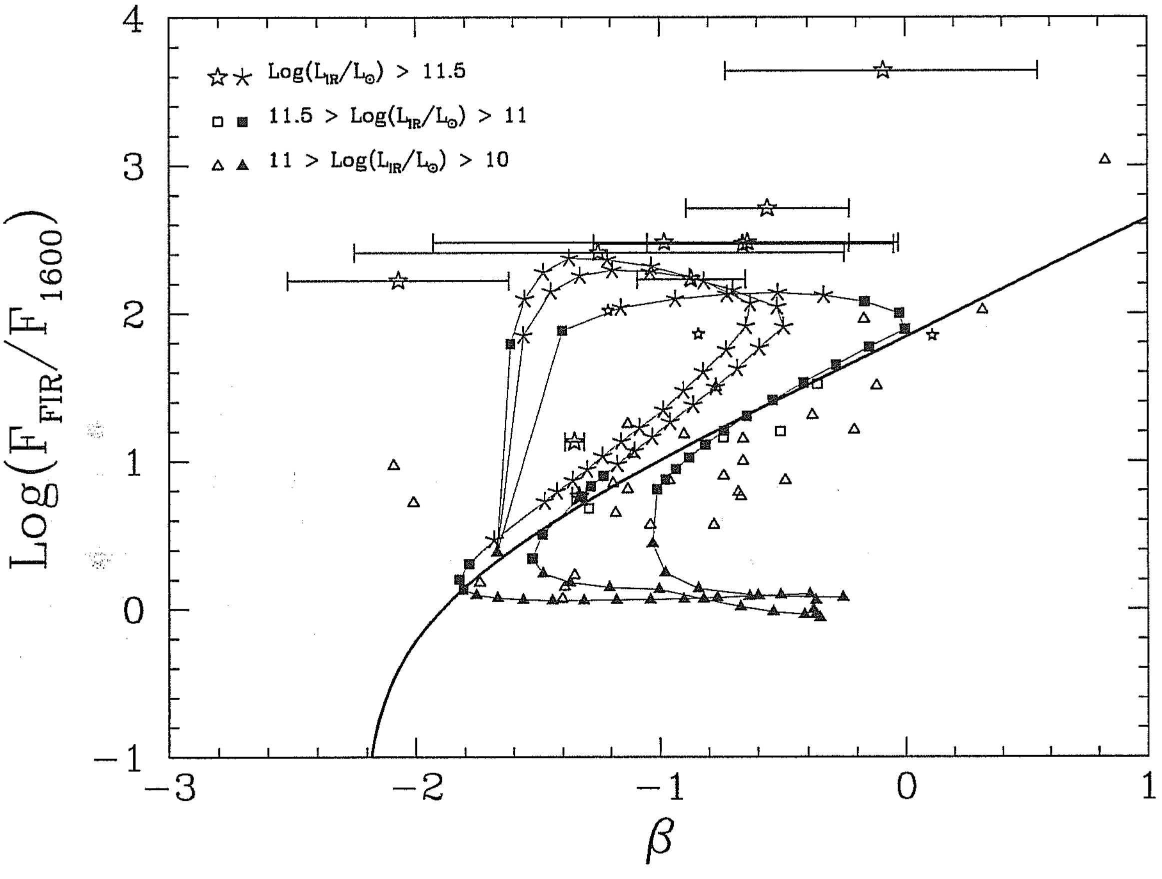

Figure 5.15: The $F_{\rm FIR}/F_{\rm UV}$ vs the UV spectral index for simulated VLIRGs. Galaxies from Wu et al. sample with $L_{\rm IR} > 10^{10}L_\odot$ are plotted with small symbols (open squares, open triangles, and open stars), while VLIRGs from Goldader et al. (2002) are shown with largeopen stars. Error bars indicate the uncertainties in the β determination. The evolution of models for three different burst timescales are compared with observations at different times from the burst set-up. The reddest sequence corresponds to $t_{\rm b} = 50$ Myr, the bluest one corresponds to $t_{\rm b} = 10$ Myr; in the middle there are the models with $t_{\rm b} = 20$ My.

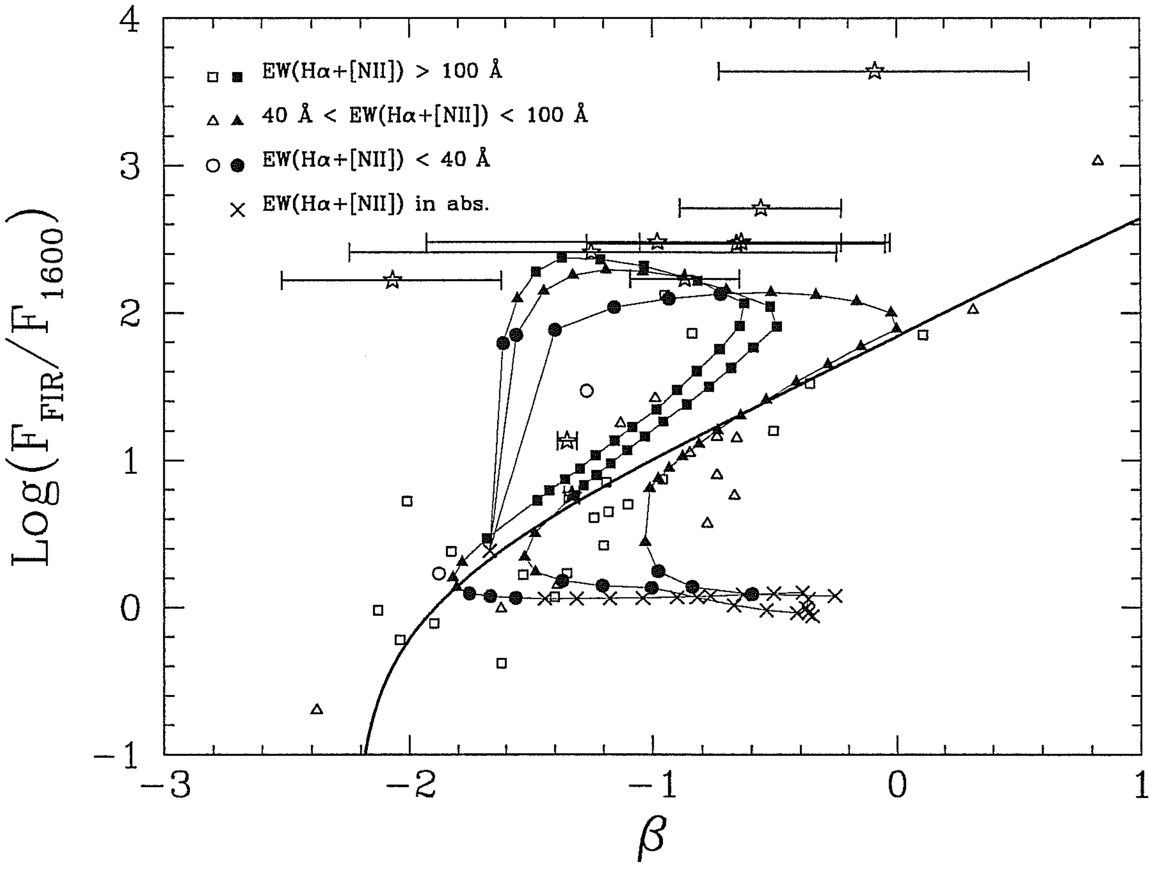

Figure 5.16: As figure 5.15, but putting in evidence the value for the equivalent width of Hα+[N II].

Table 5.2: Spectral classification by Dressler et al. (1999).

Class	EW([O II]3727)	EW(Hδ)	Comments
k	absent	<3Å.	Passive, elliptical-like spectrum.
k+a/a+k	absent	≥3Å.	Strong Balmer abs. without emission lines
e(a)	present	≥4Å.	Strong Balmer absorption plus emission
e(c)	present, > −40Å	<4Å.	Moderate Balmer abs. + emission, spiral-like
e(b)	≤ −40 Å	any	Very strong [O II]
e	present	?	At least one emission line, Hδ unmeasurable

galaxies. This would be a wrong interpretation, since the bluer end of the observed sequence is populated by galaxies with a very large equivalent width of Hα. On the contrary, evolved IR galaxies in which the star formation activity has declined have a smaller line emission. The conclusion is than UV bright sequence is not an evolutionary phase of more powerfull starburst, but the locus of galaxies in which the same stellar populations are responsible of both UV and FIR emission, namely when the attenuation is not too large.

Another important result is that the different position of VLIRGs in the Meurer diagram compared to UV-bright starbursts is a consequence of the age selective extinction. This can also easily explain why Goldader and collaborators found that the UV emission does not spatially coincide with the IR luminous source.

5.5.3 The optical properties of VLIRGs

Poggianti & Wu (2000) studied the optical spectra of a sample of VLIRGs from Wu et al. (1998a; 1998b). The aim of their study was to understand if distant and dusty star-forming galaxies can be recognized from optical/near-IR data. The issue rises from the difficulty to identify without ambiguity dusty galaxies from optical and near-IR colors. In fact, these objects at high redshift have colors similar to high redshift evolved spheroids (Graham & Dey, 1996; Cimatti et al., 1998; Dey et al., 1999). Thus, Poggianti & Wu (2000) looked for a spectroscopic signature able to select highly extincted galaxies.

For this purpose, they classified the objects on the basis of the equivalent width of [O II]3727 and Hδ. Several spectral classes can be defined following Dressler et al. (1999) from the equivalent width of these two lines; we reported this classification in table 5.2.

The Dressler classes correspond to different kind of objects. Spectra of type k belong to passive galaxies that did not have any star formation activity in the last Gyr; type k+a/a+k spectra indicate objects that had an important star formation activity in the last Gyr but with no current activity. The classes e(c) and e(b) are typical of respectively normal spirals and starburst galaxies. Type e(a) spectra were interpreted as post-starburst galaxies with a residual star formation. However Poggianti et al. (1999) found that similar spectra are frequent in merging or interacting galaxies and rare in normal field galaxies. Thus, e(a) spectra are more likely to be interpreted as produced

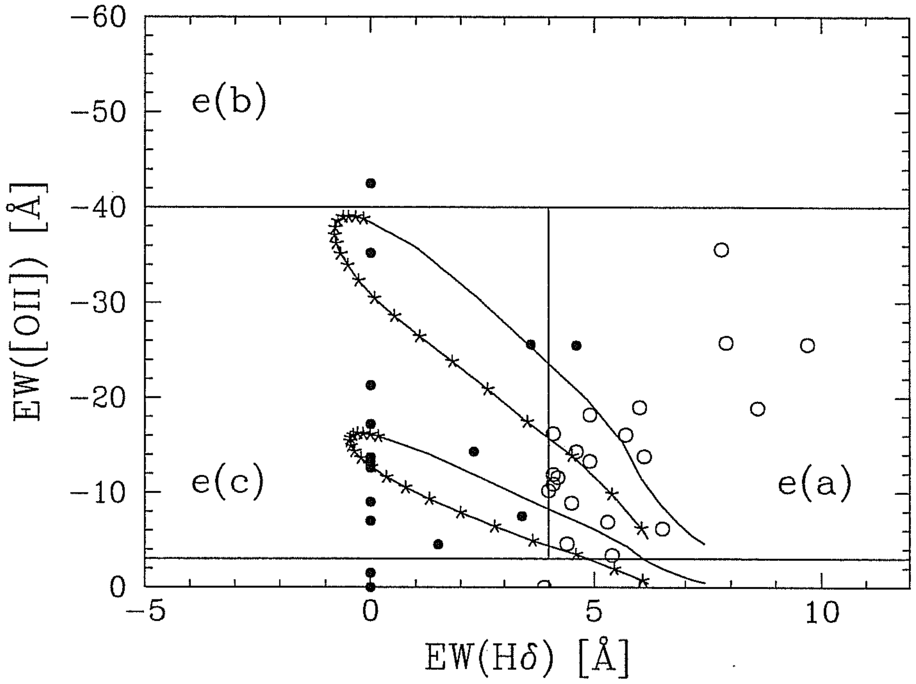

Figure 5.17: The evolution of IR starburst models on classification diagram of the [O II]3727 equivalent width versus Hδ equivalent width, compared to the observed VLIRGs by Poggianti & Wu (2000) (filled and open circles). The models shown here have $t_b = 20$ Myr; models with a lower [O II]3727 emission have a solar metallicity, the other have $Z = 0.4 Z_\odot$. Observed object with Hδ unobserved or nearly filled are placed at EW(Hδ)=0.

by dusty starburst galaxies.

Poggianti & Wu confirmed this result by finding that a large fraction (~50%) of VLIRGs in their sample have e(a) spectra. Poggianti et al. (2001) investigated the origin of the this kind of spectra by comparing the average spectum of e(a) galaxies in Poggianti & Wu with a simplified synthesis model. The simulated spectra are built as a summation of SSP spectra of different ages, each one with its own optical emission lines; the extinction value is allowed to vary from one population to another. It results that, in order to reproduce the optical continuum, the equivalent width of Hα+[N II], Hβ, Hδ and [O II]3727, and the ratio $F_{\rm FIR}/F_{\rm V}$, it is necessary to have an important age selective extinction.

Therefore, we computed the equivalent width of [O II]3727 and Hδ in our simulated galaxies. The results from the models with $t_b = 20$ Myr are compared with data from Poggianti & Wu (2000) in figure 5.17. In the figure we also show models with metallicity $Z = 0.4 \cdot Z_\odot$, since the several observed objects exhibit a ratio R_{23} ($R_{23} \equiv$ ([O II]3727+[O III]4959+[O III]5007)/Hβ, see Dessauges-Zavadsky et al., 2000) corresponding to low metallicities.

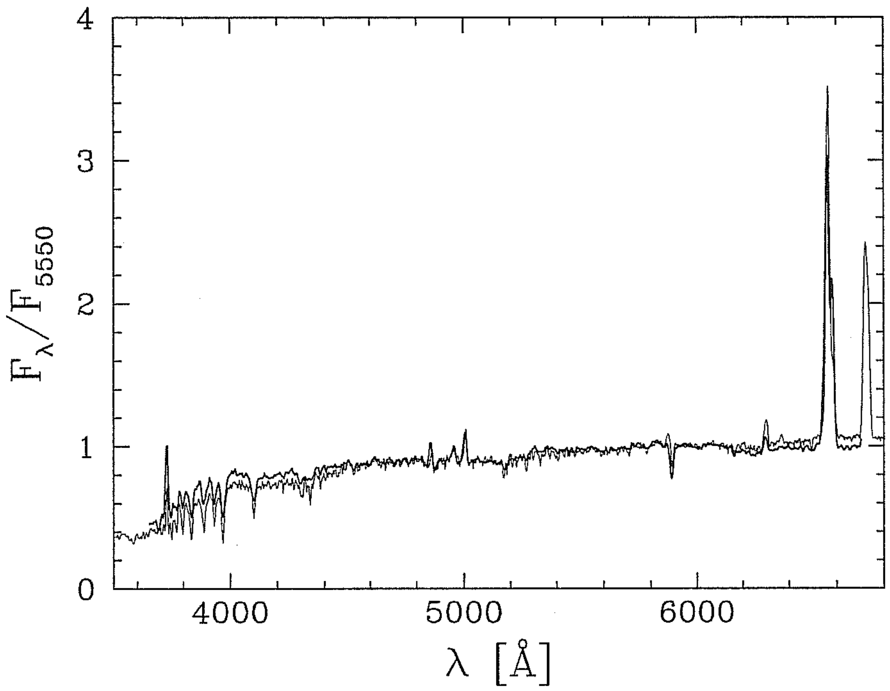

Figure 5.18: The comparison between the average spectrum of e(a) galaxies in the sample of Poggianti & Wu (2000) (thick line) and a simulated spectrum (thin line).

The models show that the e(a) spectra can be produced during the obscured phase, while in the following UV-bright phase the Hδ absorption feature is filled by the line emission. It is worth noticing that it is not possible to reproduce an EW(Hδ) $>$ 6-7 Å, as seen in four objects of the sample. Such high values of the Hδ absorption can be only obtained by assuming a previous burst with an age of some 10^8 years.

Finally, we compare in figure 5.18 the average spectrum of e(a) galaxies in the sample of Poggianti & Wu (2000) with a simulated spectrum in the obscured phase. The similarities between the two spectra point out that e(a) spectra are a common characteristic of obscured starbursts.

5.6 Discussion

In Sect. 5.3 we analyzed the sample of UV-bright starbursts by Wu et al. 2002. The diagram FIR/UV versus β does not show any clear difference in the position of the objects on the basis of the FIR luminosity or the Hα equivalent width. As expected, we only found a trend for more IR luminous galaxies to be more obscured.

The analysis of the UV spectra in the sample does not show the presence of the 2175 Å bump in the attenuation law. We estimated the expected deviation of the spectra from the power-law shape in presence of a bump and compared it with the observed deviation.

We found that the attenuation at 2175 Å (A_{2175}) is smaller than $0.99A_{1600}$, while for the galactic extinction law it is $A_{2175} = 1.35A_{1600}$; this points out that the attenuation law in UV-bright galaxies is more similar to the Calzetti attenuation law.

The models for UV-bright starbursts presented here underline that the relationship found by Meurer et al. between FIR/UV and β can also be well reproduced by an extinction law similar to the galactic one. The models in their most active phase seem to be bluer ($\Delta\beta \sim -0.5$) than the observed galaxies. Part of this displacement can be ascribed to the bump in the extinction law: if we avoid the spectral windows near the bump when computing the spectral index, we get a better agreement. It is worth noticing that the models show an expected dust free spectral index around -2.5, that is 0.3 bluer than the expected one from the Meurer relationship. This points out that the part of the disagreement between models and the Meurer relation could be due to a different intrinsic UV spectral index in the stellar continuum, possibly ascribed to an IMF which is different form the Salpeter one. However, the scatter of data around the mean relation (and the errors on the β determinations) does not allow to have a clear answer. Moreover, the scatter around the relation can be due to a variation of the IMF from one object to the other.

The attenuation laws found in our models show a reduced bump even if the exctinction law adopted in the models is the galactic one. This is a consequence of age selective extinction which, as already pointed out by Granato et al. (2000), could at least in part explain the differences between the galactic and starburst attenuation laws found in the W02 sample and in Calzetti's works. This result is an example of the importance of the inclusion of the age selective extinction when modelling dusty galaxies.

It is worth noticing that the observed luminosities in UV-bright starbursts are acheaved converting a small fraction (10%) of the total gas, in agreement to what found by Mayya et al. (2003).

Expanding our analysis to the IR luminous galaxies, we explained the observed (Goldader et al., 2002) discrepancy between the UV spectral index and the ratio FIR/UV in VLIRGs. Again, this is another effect of the age selective extinction. In particular, we found that, in the VLIRG phase, UV emission of the burst is completely converted in dust luminosity, and the UV flux comes from stellar population formed before the burst. Therefore, the observed UV spectral index is determined by the older population and does not measure the attenuation of the burst population. Thus we can conclude that the estimation of dust attenuation from the UV spectral index is useless when applied to IR luminous galaxies.

Finally, we have analysed the optical properties of our models. We found that the optical spectra in the obscured phase can be calssified as e(a) spectra, according to the Dressler et al. (1999) classification. It is worth noticing that some objects have EW(Hδ) > 6-7 Å, that can only be explained by assuming a previous burst with an age of some 10^8 years. We conlude confirming that e(a) spectra are a common characteristic of obscured starbursts, as proposed by Poggianti & Wu (2000).

Chapter 6

SFR estimators

In this chapter we discuss the different estimators of the star formation rate. After the introduction (Sect. 6.1), in Sect. 6.2 we study the estimation of the SFR from UV and IR luminosities. In Sect. 6.2.1 we discuss the use of radio emission as SFR estimators and explain the FIR-radio correlation. In Sect. 6.3 we discuss the use of emission lines for the SFR estimation. Finally, in Sect. 6.4 we compare our result with the literature.

6.1 Introduction

One of the most important quantities that distinguish the different galaxy types along the Hubble diagram is the star formation activity. Therefore, measurements of the star formation rate are a fondamental tool to study the evolution of galaxies.

The current star formation activity is always traced by looking at the signature of massive stars, because of their short lifetime. We can enumerate four different SFR indicators: the UV luminosity, the emission lines, the infrared emission of dust and the radio emission from SN accelerated electrons. A review on the SFR estimators can be found in Kennicutt (1998).

As discussed in the previous chapters, the presence of dust introduces big uncertainties in the determination of intrinsic luminosities of emission lines and UV stellar continuum. This generally causes a discrepancy between the estimated SFR from the different indicators. Several observational (Hopkins et al., 2001; Sullivan et al., 2000; Sullivan et al., 2001; Buat et al., 2002; Rosa-gonzález et al., 2002; Bell, 2003) and theoretical works (Charlot & Longhetti, 2001; Hirashita et al., 2003) have addressed this issue. The problem is particularly important when estimating the comoving space density of the star formation rate (also called cosmic SFR). In fact, the uncertainties in the UV of high redshift galaxies correcting for extinction does not allow to clearly determine if the cosmic SFR decreases or not at $z \geq 2$ (Steidel et al., 1999).

In this chapter we concentrate on the case of normal star-forming galaxies to discuss the quality of estimations of SFR from different indicators, and the impact of dust

Table 6.1: Calibrations of SFR (SFR/Luminosity) from dust emission, in 10^{-37} $M_\odot yr^{-1}W^{-1}$ (or a: 10^{-33} $M_\odot yr^{-1}W^{-1}$Å), and from UV luminosity (lower panel, in 10^{-23} $M_\odot yr^{-1}W^{-1}Hz$).

Band	SFR/L	Δ(SFR/L)
IR_{8-1000}	3.99	3.12–7.39
IR	4.98	3.62–8.93
FIR	8.82	6.12–16.4
PAH 7.7μm	46.7	31.3–81.5 a
ISO LW3	79.9	70.9–135.
MIPS 24	48.0	34.6–114.
MIPS 70	9.23	6.19–17.0
MIPS 160	7.66	6.15–13.7
UV	284.5	103.4-622.8
UV_β	125.9	92.7-184.0
UV_{FIR}	104.5	90.7-114.5

attenuation. We will cover the case of starburst galaxies and the effects of a temporally varing SFR in future works.

6.2 SFR from the UV and IR continuum

In the chapter 4, we justified the tangled relation between the attenuation properties of star forming galaxies as seen at different wavelengths, by means of a model that accounts for the complex interplay between geometry, obscuration time and stellar lifetimes.

Using these models, we have obtained calibrations of the SFR for a wide range of different observables from the UV to the radio regime.

Only models with $\tau_{esc} \leq 6$ My are used here because the majority of the data in Fig. 4.5 can be explained with short escape times, $\simeq 3$ Myr, in agreement with other evidences coming from the analysis of the UV SEDs and from the number counts in HR diagrams of massive stars (Silva et al., 1998). In order to give a useful reference value of the calibration, we selected a reference model whose parameters are summarized in Table 4.1. This model is represented by a star in Fig. 4.5. Unless otherwise specified, all calibrations refer to a Salpeter IMF with $m_{inf} = 0.15$ $M_\odot$ and $m_{up} = 120$ $M_\odot$ and solar metallicity.

Infrared luminosity is one of the most common SFR estimators. The interstellar dust is able to convert in IR emission a substantial fraction of the UV light emitted by young stars. Thus, the IR luminosity is proportional to the SFR.

The relation between the SFR and the infrared luminosity is summarized in Table

6.1. The first column indicates the observed quantity, the second column provides the value of the calibration for the reference model described above, and the last column provides the range of variation of the calibration among the set of models.

The row labeled IR_{8-1000} refers to the total dust emission from 8 to 1000 μm, while IR refers to the infrared emission estimated with the four IRAS bands (Sanders & Mirabel, 1996) and FIR refers to the far-infrared emission estimated from the 60 and 100 μm IRAS bands (as described in Helou et al. 1988).

In the following rows of Table 6.1, we show the calibration of the specific luminosity at the peak of the PAH emission feature at 7.7μm (PAH 7.7μm), the flux in the ISO band LW3, and the SIRTF experiment MIPS at 24μm, 70μm and 160μm.

The infrared estimators exhibit larger variations in normal star-forming galaxies than in starburst galaxies. Inspection of the above table shows that the calibrations can vary by up to 80% around the reference model. In the case of normal galaxies a considerable part of radiation from young stars is not absorbed by MCs clouds, so that variations in the duration of the obscuration by MCs and in the optical depth of MCs produce an important change in IR emission. Furthermore, the absorption of light from old populations by diffuse dust may be a significant source of IR radiation, thus weakening the correlation with the SFR. This is quite different from more powerful starbursts where most of the energy produced by young stars is converted into IR emission, so that variations in absorption do not produce any important variation of the IR flux.

The ratio between SFR and UV luminosity (λ_{UV}=2000 Å) is presented in the lower panel of Table 6.1. First row refers to UV uncorrected for dust extinction, the second to the UV luminosity corrected for extinction through the UV slope (A_{UV} vs β, eq. 5.1 converted to 2000 Å) and the last row to UV luminosity corrected for extinction by adopting the relation A_{UV} vs $\log(F_{\mathrm{FIR}}/F_{\mathrm{UV}})$ with eq. 4.9 and 4.10. These calibrations refer to face-on models; calibrations from edge-on modes have a much larger range of variation, with the important exception of FIR-corrected estimator.

It is important to notice that the FIR-corrected UV estimator is quite robust; in fact, as shown in sec. 4.3, the attenuation in the UV is tightly related to the ratio $F_{\mathrm{FIR}}/F_{\mathrm{UV}}$, for a significant variation of the optical depth and escape time (Fig. 4.7). Consequently, by adopting the ratio $F_{\mathrm{FIR}}/F_{\mathrm{UV}}$ to estimate A_{UV}, one may get the intrinsic UV flux and obtain a reliable SFR indicator. In summary, UV and FIR fluxes alone are fragile SFR indicators, while their combination is a very good estimator of the UV attenuation. Notice also that, because of the slope of the relation A_{UV} vs $F_{\mathrm{FIR}}/F_{\mathrm{UV}}$, this method is not much affected by uncertainties in the FIR flux due to old populations.

We also provide the dust free calibration of UV for different metallicities in Table 6.2.

Table 6.2: Calibrations of SFR in UV band in the dust-free case, and for radio emission (in 10^{-23} $M_{\odot} yr^{-1} W^{-1} Hz$) as a function of metallicity.

Z	UV	1.49 GHz	8.44 GHz
0.0008	78.9	59.5	166.1
0.004	88.7	65.1	212.6
0.008	94.8	66.6	230.9
0.015	99.7	67.7	246.2
0.02	103.4	68.6	258.4
0.03	107.7	69.8	269.1
0.04	112.3	71.1	280.7
0.05	117.4	72.5	293.5

6.2.1 SFR from radio and the FIR/Radio ratio

We report in Table 6.2 the new radio calibrations at 1.49 GHz and 8.44 GHz, according to Bressan et al. (2002), as a function of the stellar metallicity. The emission at these frequencies in our model is provided by ionized gas (thermal emission) and SN remnant (non-thermal emission). The variation in luminosity (at constant SFR) is due to the variation of the number of ionizing photons of SSPs with metallicity, of the temperature of the ionized gas for free-free component, and to the variation of SN rate for non-thermal contributions. It is worth noticing that the variation of 1.49 GHz calibration with metallicity is ±15%.

Observations indicate that FIR and radio emissions are strongly correlated over a wide range of IR luminosities, from star-forming to starburst galaxies (Sanders & Mirabel, 1996):

$$q = \log \frac{F_{\rm FIR}/(3.75 \times 10^{12}{\rm Hz})}{F_{\rm 1.49GHz}/({\rm W\ m^{-2}Hz^{-1}})} \simeq 2.35 \pm 0.2\ . \qquad (6.1)$$

From calibrations in Table 6.1 and in Table 6.2, for the FIR and the 1.49 GHz, we obtain $q = 2.32$ for the reference model, with a range of variation $q = 2.05 - 2.48$.

Remarkably, the 0.2 dex observed scatter is fully accounted in our models simply by the variation of the SFR-FIR relationship (see also Perez-Olea & Colina 1995). This suggests that the relationship between radio emission and star formation is extremely tight and implies that the underlying physical mechanism responsible for it is quite homogeneous.

Although IR and radio calibrations depend on $f_{\rm d}$ (here assumed to be 0.3), their values changes for less than 5% (25% for 8.44 GHz) if $f_{\rm d} = 0$ is assumed.

Table 6.3: Calibrations of SFR for emission lines (in 10^{-33}M$_\odot$yr^{-1}W^{-1}, or *a:* in 10^{-35} M$_\odot$yr^{-1}W^{-1}. No dust: the intrinsic calibrations in the case without dust. Ref. model: calibrations for the reference model. Max value: the maximum value found in our models. The values between brackets in the forth column refer to the edge-on case.

Line	No dust	Ref. model	Max value
Hβ	0.188	0.758	7.94 (25.8)
Hα_0	6.01	6.62	15.12 (29.3) *a*
Paβ	1.01	1.415	2.52 (4.37)
Paβ_0	1.01	1.01	1.06 (1.18)
Paα	0.432	0.505	0.676 (0.938)
Brγ	5.65	6.31	7.86 (10.2)
Brβ	3.26	3.50	4.12 (4.96)
Brα	1.68	1.721	1.91 (2.10)
Huα	12.8	13.12	14.7 (16.2)
[O II]3727	0.127	0.844	25.2 (104.8)

6.3 Optical near- and mid-infrared emission lines

H recombination lines are the only ones almost proportional to the Lyman continuum flux and, as a consequence, to the SFR; other emission lines also depend on other quantities so that their use as SFR estimators is quite dangerous.

In Table 6.3 we report our calibrations for some emission lines. The second column shows the intrinsic calibrations (without dust); the third column provides the calibration for the reference model described above. The forth column provides the maximum value found in our models (the minimum value of calibrations corresponds to the case without dust).

The calibrations are given assuming that the fraction of ionizing photons absorbed by dust inside H II regions (f_d) is 0. Calibrations for different values f_d can be obtained by dividing the value reported by $1 - f_d$.

Hβ. The first entry in the table is Hβ uncorrected for extinction; this line may be the only hydrogen line detected in the spectra of intermediate–redshift galaxies and, in that case there is no way to correct it for extinction. The calibration we provide here shows that for a typical SFR of a few M$_\odot$/yr, the inferred SFR may be underestimated by a factor of three.

Hα_0. The Hα_0 row refers to the Hα luminosity corrected for extinction using the Balmer decrement (eq. 4.3). We notice that the decrement has been evaluated from comparisons of the observed ratio of the intensity of the emissions at Hα and Hβ with the expected ratio. We did not attempt to simulate a real measure of the Balmer decrement in a synthetic spectrum. Thus, our calibration assumes that one is able to correct the lines for the contribution of the underlying older populations.

It is worth noticing that, due to the age selective extinction, the calibration may change by a factor of two, or even more because the extinction at Hα is underestimated, as demonstrated in Sect. 4.3.2, when the escape time is similar to the lifetime of ionizing stars.

Another factor of uncertainty is provided by the orientation of the observed galaxy because the extinction from diffuse medium is characterized by a mixed geometry, which tends to produce a higher ratio between attenuation and reddening than for the screen geometry.

Paβ, Paβ_0. In Table 6.3 then Paβ follows, either uncorrected or corrected (Paβ_0) for extinction, assuming that the intrinsic value of Paβ/Brγ is 5.65 (and $\tau_{\mathrm{Pa}\beta}/\tau_{\mathrm{Br}\gamma} = 2.95$). In this case the extinction is lower and the SFR can be obtained with a large accuracy. However, it must be kept in mind that at these wavelengths uncertainties in the photometry of different wavebands may constitute the larger source of uncertainty in the estimated extinction (eg. Calzetti et al. 1996).

Paα. The table continues with Paα uncorrected for extinction. This line sits at the short wavelength border of the K band (λ=18752Å); like Hβ, it may be detected by ground observations only in the spectra of intermediate redshift galaxies.

Brγ, Brβ, Brα, Huα. The following entries in the table are Brγ, Brβ, Brα and Huα uncorrected for extinction. As expected, the extinction effects decrease when the wavelength increases, except for Huα ($\lambda = 12.372\mu$m) that falls in the absorption feature of silicates. We did not considered the Pfα because it is superimposed to the 7.7μm PAH emission that outshines it.

[O II]3727. The table closes with the [O II]3727 line uncorrected for extinction (note we only use solar metallicity). The importance of this line is that in high redshift galaxies this is the only bright line that, once redshifted, remains in the optical domain. Recently, Jansen et al. (2001) investigated the use of this line as SFR tracer, and found that SFR estimations by means of [O II]3727 agree with the Hα_0 value, as long as the line intensity is corrected for extinction and calibrated for metallicity. However, it is not possible to perform these corrections without observing other lines that (if visible) are better estimators of SFR; therefore we conclude that [O II]3727 is a poor indicator of SFR.

Table 6.4: SFR calibrations as a function of metallicity

Z	Hα	Hβ	Paα	Paβ	Brα	Brβ	Brγ	Huα
0.0008	0.03541	0.10139	0.34008	0.67452	1.51153	2.55926	4.08921	13.00402
0.0040	0.04253	0.12297	0.36807	0.76569	1.56540	2.76821	4.53969	13.01145
0.0080	0.04848	0.14261	0.39540	0.84931	1.63540	2.97196	4.95617	13.25893
0.0150	0.05393	0.16369	0.41011	0.91920	1.63674	3.08429	5.25272	12.83562
0.0200	0.06008	0.18817	0.43235	1.00523	1.67584	3.25748	5.64724	12.78491
0.0300	0.05988	0.19754	0.39877	0.98059	1.48264	3.02189	5.38029	10.84010
0.0400	0.06167	0.21058	0.39288	1.00109	1.42695	2.99529	5.41738	10.17261
0.0500	0.06131	0.21591	0.37661	0.98956	1.34182	2.89063	5.30293	9.36745

Table 6.5: Comparison of some calibrations of SFR with results from previous works. Calibrations are referred to a Salpeter IMF between 0.1 and 100 $M_\odot$. Reference: *a:* Kennicutt (1998), *b:* Haarsma et al. (2000).

	This work	others	
UV	1.20	$1.4 \cdot 10^{-21}$ $M_\odot yr^{-1} W^{-1} Hz$	*a*
IR_{8-1000}	4.63	$4.5 \cdot 10^{-37}$ $M_\odot yr^{-1} W^{-1}$	*a*
Hα	7.05	$7.9 \cdot 10^{-35}$ $M_\odot yr^{-1} W^{-1}$	*a*
1.49 GHz	79.6	$123.3 \cdot 10^{-23}$ $M_\odot yr^{-1} W^{-1} Hz$	*b*

6.4 Comparisons with literature

By using our set of simulated disk galaxies, we calibrated different SFR estimators, collected in Tables 6.1, 6.2 and 6.3. Some calibrations may be compared with values obtained in the literature. In particular we compare the results with Kennicutt (1998) (UV, IR and Hα) and Haarsma et al. (2000) (radio); these comparisons are summarized in Table 6.5, after a small correction factor (1.16), which accounts for the slightly different IMF adopted, is applied to our estimates.

There is a good agreement for Hα, UV and IR calibrations (note that Kennicutt uses the notation FIR for the total dust emission between 8 and 1000 μm), while our calibration for the radio emission is a factor 1.5 smaller than that proposed by Condon (1992) and Haarsma et al. (2000), and a factor 1.3 larger than the one quoted by Carilli (2002).

It is worth noticing that our calibrations give a ratio (eq. 6.1) between the radio and FIR emissions, $q = 2.32$, very close to the observed value, and that we can explain in a natural way the scatter around the observed relation. In disk galaxies, this scatter is due to the variation of the fraction of stellar emission absorbed (and re-radiated) by dust.

In the case of normal star forming galaxies, the model evidences that Hα, UV and even IR estimators of SFR are affected by important scatters. For what concerns Hα, this is due to the age selective extinction, that can produce an underestimate of the attenuation when it is derived by the Balmer decrement. Also IR emission by itself does not provide an accurate estimate of the SFR in disk galaxies, because the fraction of UV radiation not absorbed by the dust can be high. The combination of UV and FIR luminosities provides a very good SFR estimator essentially because, even for a modest SFR, one recovers in the FIR what is lost in the UV.

Chapter 7

Infrared emission lines

This chapter is dedicated to some application of infrared lines. After a short introduction (Sect. 7.1), in Sect. 7.2 we describe the estimation of metallicity from IR lines, and propose a new method based on far infrared lines. In Sect. 7.3 we applied our model to the study of a excitation diagram of galactic H II regions and starbursts. Finally, in Sect. 7.4 we discuss the possibility to use near-IR emission lines to study the formation process of elliptical galaxies.

7.1 Introduction

Many emission lines are present in the IR spectra of galaxies. These lines became very interesting with the ISO mission that provided the first moderate and high[1] resolution infrared spectra. The SIRTF mission and the future Herschel mission will provide a big amount of spectra, in the mid- and far-infrared respectively, and the knowledge on infrared nebular lines will become essential to extract more information from those spectra. Furthermore, their long wavelength reduce drastically the effects of dust obscuration on them, and become very useful in highly obscured objects.

Apart from the hydrogen recombination lines, all the luminous metallic lines in the IR are fine-structure transitions These are transition between electronic configurations in which an electron change only its magnetic momentum number. Although their transition probabilities are very low, these lines are rather luminous (possibly more than optical lines) and their emission is an important cooling mechanism of gas, especially at high metallicity.

Fine-structure lines are excellent diagnostics of gas density, hardness of the exciting radiation field and abundance of important elements.

---

[1] The adjective "low", "high" or "moderate" are used in infrared spectroscopy, when referred to the spectral resolution, with a different meaning from the use in optical spectroscopy. In fact, a resolution power $R = \lambda/\Delta\lambda$ around 1000 is commonly considered in the infrared a high resolution, while in the optical high resolution is with $R \gg 10^4$.

Different fine-structure transitions of the same ion have different sensitivity to collisional deexcitation. This can be used to identify the typical electron density of the emitting gas (Rubin et al., 1994). Typical line pairs used for this purpose are [Ar III]21.8μm/9μm, with a maximum sensitivity to the electron density at $\log(n_e) = 4.7$, [Ne III]36/15.5μm ($\log(n_e) = 4.7$), [O III]52/88μm ($\log(n_e) = 2.9$), [S III]19/33μm ($\log(n_e) = 3.5$), and [N II]122/205μm ($\log(n_e) = 1.8$). Though collision strengths for these lines may need to be reexamined (Rubin et al., 2001), it appears that they can trace the density of the emitting gas over a wide range, from $n_H = 10$ cm^{-3} to $n_H = 10^5$cm^{-3}, i.e. possibly encompassing the typical densities of star forming regions in normal galaxies as well as in compact obscured starbursts (Bressan et al., 2002).

The ratio of fine-structure line intensities from suitable elements in different ionization stages can be used to obtain information on the ionizing spectrum and the ionization parameter of H II regions. This analysis is particularly interesting because it can provide constrains on the stellar atmosphere models and on the IMF shape at higher masses. As an example, the ratio [Ne III]15.5μm/[Ne II]12.8μm depends mainly on the fraction of photons with $\lambda < 302.8$ Å over the total Lyman photons, and not on the temperature of the ionized gas.

Finally, the weak dependency of fine-structure line on the temperature makes these lines good estimators of the gas metallicity. Commonly, the gas metallicity is derived from optical metallic lines; however their emission falls when the gas temperature is lower than 10^4 K. As the gas metallicity grows the gas temperature decreases, and the emission of optical metallic lines rapidly decreases over the solar metallicity. On the contrary, fine-structure line can be used for abundance determinations up to $Z \sim Z_\odot$.

7.2 Abundance determinations

It is straightforward to extend to the infrared the method used for abundance determinations for optical lines. This method is based on the ratio between the sum of the intensities of the most abundant ions of an element, and that of a hydrogen recombination line (typically the Brα line). It works as long as the current density is lower than the critical density for collisional deexcitation of the involved transition.

Let's take the case of a generic element X that is present in the ionization states X II, X III etc. Let's suppose to observe one transition for each ionization state. The abundance relative to hydrogen is given by:

$$\frac{\mathrm{X}}{\mathrm{H}} = \frac{\alpha_{\mathrm{Br}\alpha} h\nu_{\mathrm{Br}\alpha}}{L_{\mathrm{Br}\alpha}} \left(\frac{L_{[\mathrm{XII}]}}{q_{[\mathrm{XII}]} h\nu_{[\mathrm{XII}]}} + \frac{L_{[\mathrm{XIII}]}}{q_{[\mathrm{XIII}]} h\nu_{[\mathrm{XIII}]}} + ... \right) \tag{7.1}$$

where $\alpha_{\mathrm{Br}\alpha}$ is the recombination rate of hydrogen with emission of Brα, and $q_{[\mathrm{XII}]}$ is the collisional excitation rate of [X II] transition (for electronic density near to zero). The last can be rewritten as:

$$q = \frac{8.629 \cdot 10^{-6}\mathrm{K}^{1/2}}{T_\mathrm{e}^{1/2}} \cdot \frac{\gamma_{lu}}{\omega_l} e^{-\frac{\chi_{lu}}{kT_\mathrm{e}}} \ \mathrm{cm}^3/\mathrm{s} \tag{7.2}$$

where γ_{lu} is the effective collision strength of the transition, ω_l is the statistical weight of the lower level in the transition, and χ_{lu} is the energy difference.

In the near- and mid-infrared the elements to which we can apply the above method are neon ([Ne III]15.5μm and [Ne II]12.8μm), argon ([Ar III]9μm and [Ar II]7μm) and sulphur ([S IV]10.5μm, [S III]18.7μm and [S II]1.03μm). Suitable calibrating relationships can be found in Giveon et al. (2002) and Verma et al. (2003).

In the far-infrared the method is applicable only to nitrogen ([N II]122μm and [N III]57μm). For these lines we have derived the following calibrations with respect to the Brα line for different assumptions on the electronic temperature T_e. From Storkey & Hummer (1995):

$$\alpha_{\mathrm{Br}\alpha} h\nu_{\mathrm{Br}\alpha} = \begin{cases} 9.906 \cdot 10^{-27}\mathrm{erg} \cdot \mathrm{cm}^3/\mathrm{s} & \text{for } T_\mathrm{e} = 10000\ \mathrm{K} \\ 2.298 \cdot 10^{-26}\mathrm{erg} \cdot \mathrm{cm}^3/\mathrm{s} & \text{for } T_\mathrm{e} = 5000\ \mathrm{K} \end{cases} \tag{7.3}$$

From Peng & Pradham (1995):

$$q_{[\mathrm{NIII}]57} h\nu_{[\mathrm{NIII}]57} = \begin{cases} 0.21 \cdot 10^{-20}\mathrm{erg} \cdot \mathrm{cm}^3/\mathrm{s} & \text{for } T_\mathrm{e} = 10000\ \mathrm{K} \\ 0.28 \cdot 10^{-20}\mathrm{erg} \cdot \mathrm{cm}^3/\mathrm{s} & \text{for } T_\mathrm{e} = 5000\ \mathrm{K} \end{cases} \tag{7.4}$$

From Lennon & Burke (1994):

$$\gamma_{[\mathrm{NII}]122} = \begin{cases} 1.12 & \text{for } T_\mathrm{e} = 10000\ \mathrm{K} \\ 1.0 & \text{for } T_\mathrm{e} = 5000\ \mathrm{K} \end{cases}, \ \omega_{[\mathrm{NII}]122} = 3 \tag{7.5}$$

Thus, knowing that $h\nu_{[\mathrm{NII}]122} = 1.6314 \cdot 10^{-21}$ J:

$$q_{[\mathrm{NII}]122} h\nu_{[\mathrm{NII}]122} = \begin{cases} 5.1938 \cdot 10^{-22}\mathrm{erg} \cdot \mathrm{cm}^3/\mathrm{s} & \text{for } T_\mathrm{e} = 10000\ \mathrm{K} \\ 6.4811 \cdot 10^{-22}\mathrm{erg} \cdot \mathrm{cm}^3/\mathrm{s} & \text{for } T_\mathrm{e} = 5000\ \mathrm{K} \end{cases} \tag{7.6}$$

$$\frac{\mathrm{N}}{\mathrm{H}} = \begin{cases} 1.907 \cdot 10^{-5} \left(L_{[\mathrm{NII}]122} + 0.247 L_{[\mathrm{NIII}]57}\right) / L_{\mathrm{Br}\alpha} & \text{for } T_\mathrm{e} = 10000\ \mathrm{K} \\ 3.546 \cdot 10^{-5} \left(L_{[\mathrm{NII}]122} + 0.231 L_{[\mathrm{NIII}]57}\right) / L_{\mathrm{Br}\alpha} & \text{for } T_\mathrm{e} = 5000\ \mathrm{K} \end{cases} \tag{7.7}$$

where N/H is the nitrogen abundance respect to hydrogen.

It is worth noticing that this method requires the measurement of the intrinsic intensity of a hydrogen recombination line. Thus, it is not applicable when these lines are not accessible, either because of instrumental limitation or for very high extinction. In this case, we suggest to adopt another indicator tightly correlated with the intrinsic intensity of hydrogen recombination lines or, equivalently, with the SFR. The best SFR indicator

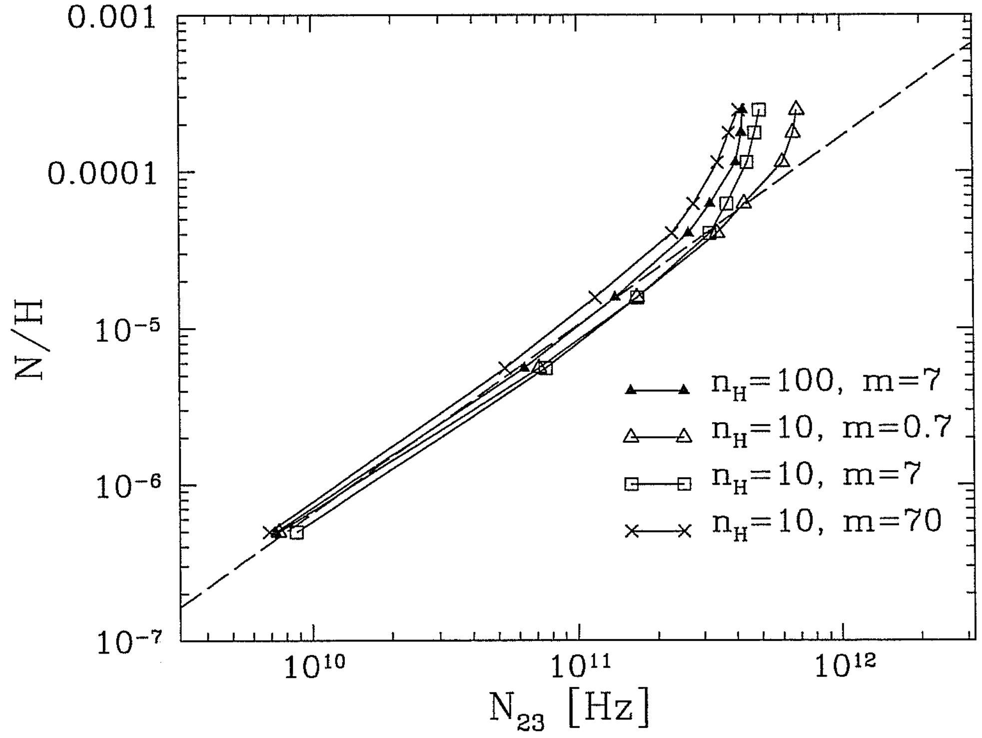

Figure 7.1: The relationship between nitrogen abundance (relative to hydrogen) and N_{23} (defined by eq. 7.8) for models with different densities and ionization parameters. The dashed line shows a linear fit to models with $Z < 0.015$.

we have found is the radio luminosity (Table 6.2). To this purpose, we have run a set of models varying the metallicity of the gas (from Z=0.0008 to Z=0.05), the hydrogen density, from 10 to 100 cm^{-3}, and the ionization parameter. The latter is a function of the mass of ionizing clusters M^*, and of the filling factor ϵ through eq. 3.8. We stress that the emission lines resulting from quiescent star forming galaxies are the sum of the emission of H II regions of different ages, so that there is not a single ionization parameter U at work. However, since all the ionization parameters scale linearly with the quantity $m \equiv (M^* \epsilon^2)^{1/3}$, we have changed m from 0.7 to 70 $M_\odot^{1/3}$ to simulate a similar range of variation of U. The fraction of ionizing photon absorbed by dust was assumed to be $f_\mathrm{d} = 0.3$.

Fig. 7.1 shows the relationship in our models between the nitrogen abundance and the ratio N_{23} defined as

$$N_{23} = \left(L_{[\mathrm{NII}]122} + 0.247 L_{[\mathrm{NIII}]57}\right) / L_{1.49\mathrm{GHz}} \ . \tag{7.8}$$

We notice that the metallicity is well determined for values below solar. For higher values the relation steepens considerably making the determination of the metal content quite uncertain.

A linear fit to models in which the metallicity is lower than 0.015 is plotted in Fig. 7.1;

its analytical expression is

$$\log\left(\frac{\mathrm{N}}{\mathrm{H}}\right) = -18.21 + 1.203 \log N_{23} \ , \qquad (7.9)$$

where N_{23} is given in hertz.

We stress that this relation holds as long as the density is below the critical density for collisional de-excitation of the [N II]122μm transition ($n_e \sim 300$ cm^{-3}).

A similar calibration could be obtained by adopting the FIR luminosity instead of the radio luminosity. However, in the case of disk galaxies the relation between the FIR luminosity and the SFR is not as tight as that between the radio luminosity and the SFR (see Table 6.1) and it would introduce a significant scatter in the calibration. The use of FIR luminosity for the case of starburst galaxies seems to be more promising. We will explore this possibility in the future works.

7.3 Ionizing spectrum hardness diagnostics

Giveon et al. (2002) (hereafter G02) used the ratios [Ne III]15.5μm/[Ne II]12.8μm, [Ar III]9μm/[Ar II]7μm, and [S IV]10.5μm/[S III]19μm to study the properties of single galactic and extragalactic H II regions observed with ISO. In particular, they compared the observed ratios with H II region models computed with *Cloudy*. In the computation they assume that each H II region is excited by a single massive star instead of a cluster or an OB association. The filling factor was fixed to 1, therefore the ionizing flux (and by consequence the ionization parameter) is only a function of the star temperature. Thus, once computed the nebular models, they obtain a single path on the diagnostic diagrams [Ar III]9μm/[Ar II]7μm versus [Ne III]15.5μm/[Ne II]12.8μm.

The stellar spectra were computed using stellar atmospheric models both with hydrostatic Local Thermal Equilibrium (LTE) from Kurucz (1992) and Non-LTE with winds, the latter computed with the stellar atmosphere code from Pauldrach et al. (2001). The stellar effective temperature used in G02 models ranges from 35000 to 45000 K.

The results obtained by G02 show that models with LTE atmospheres have a much lower value of the ratio [Ne III]15.5μm/[Ne II]12.8μm than observed galactic H II regions, while Non-LTE models reproduce quite well the position of observed galactic H II regions in the diagram.

Verma et al. (2003) analyzed some starburst spectra and compared their excitation diagram with the sample by Giveon et al. The region occupied by the two different samples overlaps, however the starbursts show a ratio [Ne III]15.5μm/[Ne II]12.8μm higher (up to 10 times larger) than the galactic H II regions.

Since the analysis done in G02 do not explains the results of Verma et al. (2003), we used our code to compute the expected emission of starbursts and to compare it with G02 and Verma et al. observations.

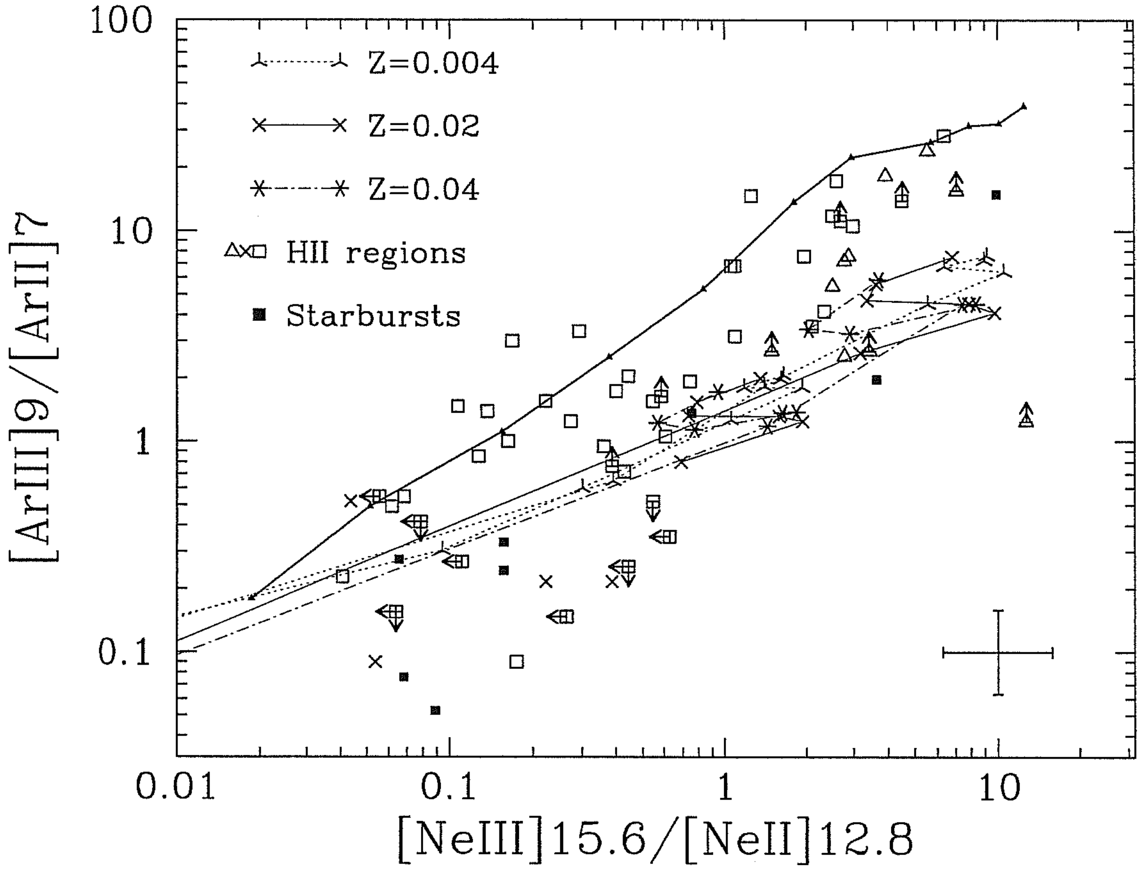

Figure 7.2: The excitation diagram [Ar III]9μm/[Ar II]7μm versus [Ne III]15.5μm/[Ne II]12.8μm luminosity ratios. Observed galactic H II regions by G02 are shown with crosses (those within 1 kpc from the galactic center) and open squares (those outside 1 kpc from the galactic center); extragalactic H II regions by G02 are shown with open triangles. Upper- or lower-limits in ratios determinations are plotted with arrows. Observed starbursts by Verma et al. (2003) are shown with filled squares. The cross in the lower right corner represent the typical errors of observed data. Finally, the thick line refer to the models by G02 for galactic H II regions.

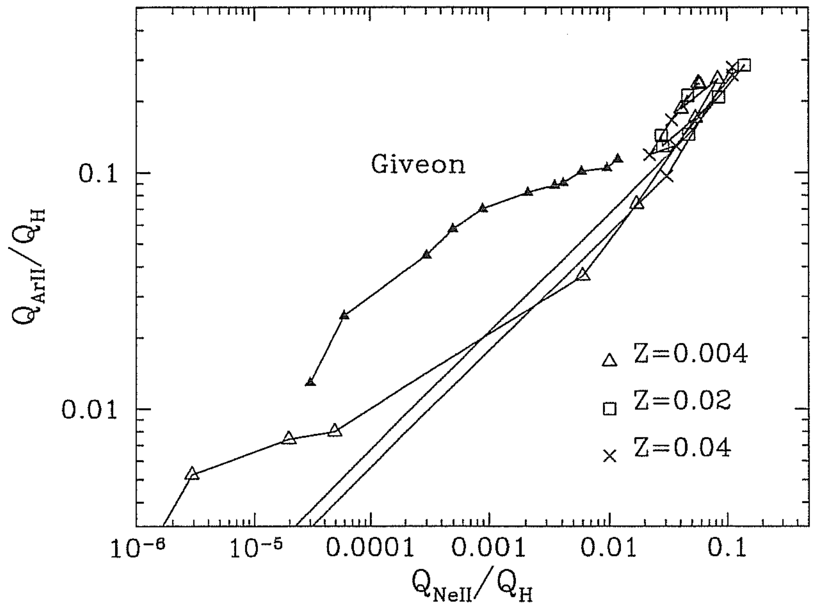

Figure 7.3: The ratio $Q_{\mathrm{ArII}}/Q_{\mathrm{H}}$ versus $Q_{\mathrm{NeII}}/Q_{\mathrm{H}}$ for G02 NLTE stellar spectra of different effective temperature (filled triangles) compared with our SSP spectra at different ages, for three different metallicity.

We computed the nebular emission due to star clusters of different ages ranging from 0 to 20 Myr for different assumptions on the filling factor and stellar mass ($m = 1$ and $m = 0.1$) The results are shown in figure 7.2. Form the figure we recognize that our models cover only part of observed galactic H II regions while starburst data are well reproduced.

The main difference between our models and G02 models stays in the fact that we use SSP spectra instead of single stellar spectra. The IMF used in our SSP extended up to m_{up}=125 $\mathrm{M}_{\odot}$, thus it contains stars with effective temperature much higher (up to 10^5 K) than the temperature used by G02. As a consequence, our SSP spectra contain much more hard photons than G02 spectra.

This is shown in figure 7.3 where we compared the hardness of SSP spectra at different ages and metallicity with the G02 spectra. The hardness is expressed in term of $Q_{\mathrm{ArII}}/Q_{\mathrm{H}}$ and $Q_{\mathrm{NeII}}/Q_{\mathrm{H}}$, noticing that the Ar II is ionized by photons with $\lambda < 448.7$ Å and Ne II is ionized by photons with $\lambda < 302.8$ Å. SSP spectra show an $Q_{\mathrm{NeII}}/Q_{\mathrm{H}}$ up to 15 times higher than G02 stellar spectra. The high value of [Ne III]15.5μm/[Ne II]12.8μm found in our model is thus a consequence of the higher hardness of of SSP spectra.

The results shown in figure 7.2 suggest that also in starbursts the hardest region of ionizing spectra is dominated by stars more massive than 30 $\mathrm{M}_{\odot}$ and that the IMF in these objects must extend up to masses around 100 $\mathrm{M}_{\odot}$. A similar conclusion was achieved by Thornley et al. (2000) that analyzed the [Ne III]15.5μm/[Ne II]12.8μm comparing it with the IR luminosities for some starbursts.

We support that the difference shown between galactic H II regions and starbursts can be explained looking at the different star formation activity regime. In fact, the Galaxy form stars in a quiescent regime, so young stars are produced prevalently in small star clusters and OB associations with a total mass smaller than 1000 $M_\odot$ (Lada & Lada, 2003). In this case it is more unlikely that a OB association have stars more massive than 30 $M_\odot$. On the contrary, in starbursts the star clusters are much bigger and the presence of massive stars is more probable.

Finally, we comment on the position of the observed data on the excitation sequence in figure 7.2. From our models we found that the degree of excitation is mainly due to the ratio $Q_{\rm He}/Q_{\rm H}$. In fact, models with the same $Q_{\rm He}/Q_{\rm H}$ but with a ionization parameter that differ for one order of magnitude show a variation of line ratios smaller than 0.6 dex, while a variation of a factor 2 in $Q_{\rm He}/Q_{\rm H}$ provides a variation of line ratios around 4. We conclude that the excitation sequence is mainly due to the shape of the ionizing continuum, that changes with the age of the stellar population. So we confirm Thornley et al. (2000) results that the sequence is an age sequence. This is also in agreement with Verma et al. (2003), who found that highly excited starbursts exibit WR star emissions.

7.4 Models for spheroidal galaxy formation

Recently Granato et al. (2003, henceforth GDS03) presented a physically motivated model for the early co-evolution of massive spheroidal galaxies and the active nuclei at their centers. The model has been built by extending the previous scenario descibed in Granato et al. (2001), which made use of a partly empirical approach.

The model, in the framework of a cold dark matter cosmology, follows with simple recipes and a semi-analytic technique the evolution of the baryonic component. The main difference with respect to other treatments, were the nuclear activity is usually regarded as an incidental diversion, is in the emphasis given to the formation of a super massive black hole in the galaxy center, and to the effect of following QSO activity. As a result, the physical processes acting on baryons reverse the order of formation of spheroidal galaxies with respect to the hierarchical assembling of DM halos. This is in agreement with the previous conclusions of Granato et al. (2001). We refer the reader to GDS03 for a full description of the model.

GDS03 found predictions in excellent agreement with observations for a number of observables which proved to be extremely challenging for all the current semi-analytic models, including the sub-mm counts and the corresponding redshift distributions, and the epoch-dependent K-band luminosity function of spheroidal galaxies.

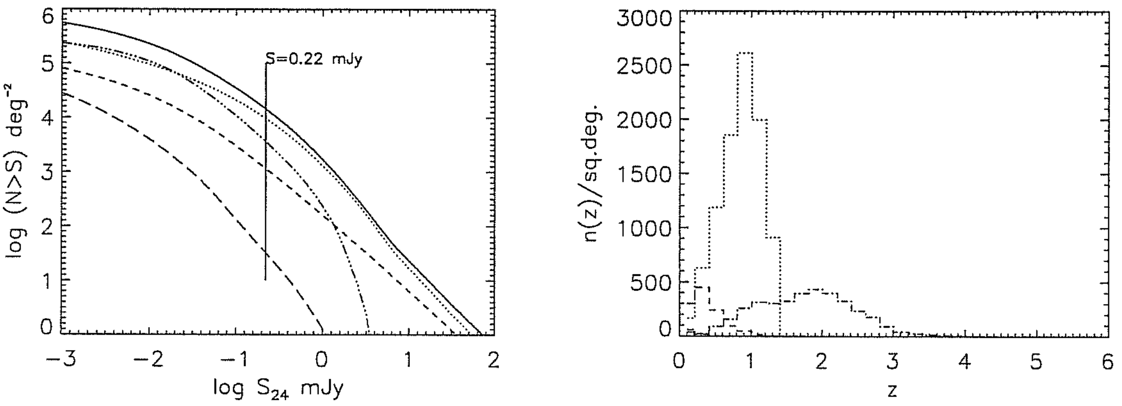

Figure 7.4: 24μm source counts and redshift distributions, at 0.22 mJy, the expected 5σ confusion limit. The dotted line refers to starbursts, the dashed one is for spirals, the dot-dashed one for star-forming spheroidal galaxies, long dashed line for passively evolving spheroidal galaxies.

7.4.1 Number counts for SIRTF surveys

A unique opportunity to observe spheroidal galaxies in their formation phase is given by the infrared space satellite SIRTF. The Space InfraRed Telescope Facility (SIRTF) is the last Great Observatory mission lunched (August 26th 2003) by NASA. The observatory carries an 85 cm cryogenic telescope and three scientific instruments:

- The InfraRed Array Camera (IRAC): a four-channel camera that provides simultaneous 5.2 ×5.2 arcminutes images at 3.6, 4.5, 5.8 and 8 μm.
- The InfraRed Spectrograph (IRS): an instrument for spectroscopy with low (resolution power $R \sim 60 - 120$) and moderate ($R \sim 600$) resolution in the wavelength interval 5.3-40 μm and 10-37 μm (for low and moderate resolution respectively)
- The Multiband Imaging Photometer for SIRTF (MIPS): an instrument for imaging and photometry in broad spectral bands centered nominally at 24, 70, and 160 μm, which is also designed to provide low-resolution spectroscopy ($R \sim 20$ between 52 and 99 μm).

Two projects of the SIRTF Legacy Science Program are centered on galaxy evolution: The Great Observatories Origins Deep Survey (GOODS) and the SIRTF Wide-area Infrared Extragalactic Survey (SWIRE). These two photometric surveys will observe a large number of IR galaxies at high redshifts.

Silva et al. (in preparation) according to the GDS03 model computed the expected number counts for IRAC and MIPS observations, and also which fraction of objects are forming spheroidal.

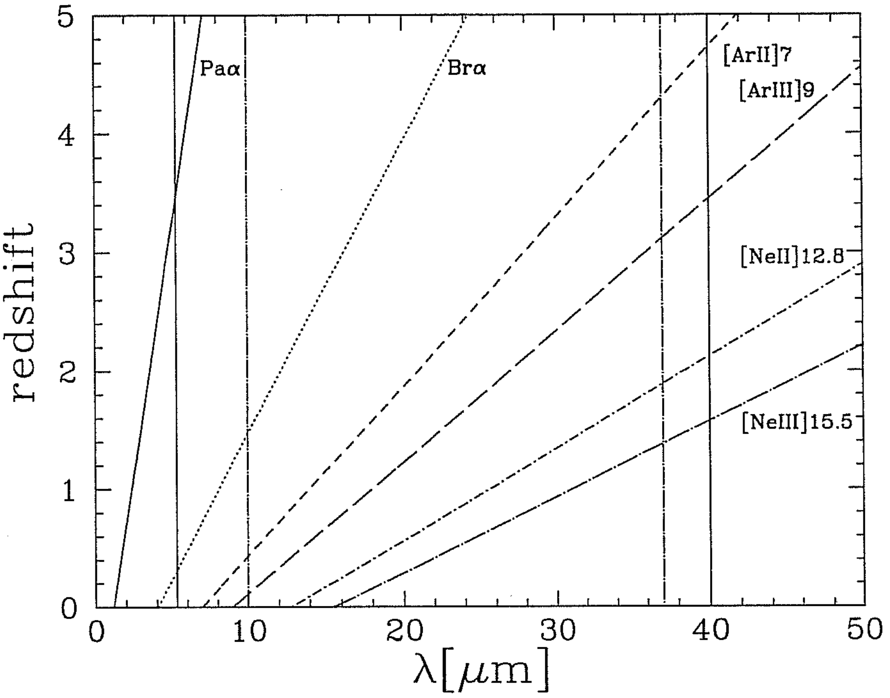

Figure 7.5: The observed wavelength of some near- and mid-infrared emission lines at different redshifts. The continue vertical lines show the spectral window covered by low resolution mode of IRS, while the dot-dashed lines refer to the high resolution mode.

Their predictions for source counts and redshift distribution at 24μm are in Fig. 7.4 (for the reference case for spheroids). Following Condon (Condon, 1974), they find a 5σ confusion limit of $S_c = 0.22$ mJy. Fig. 7.4 also shows the redshift distributions expected at 0.22 mJy. At that flux limit, a fraction 25% of the total detected sources is expected to be provided by spheroids. In the 70 and 160 μm bands, at the confusion limit, a fraction up to 50% of the total sources could be provided by spheroids.

It is worth to investigate if the NIR emission lines expected from these galxies can be detected with IRS.

7.4.2 Emission lines observations with SIRTF

Figure 7.5 sketches the wavelength shift of several luminous near- and mid-infrared emission lines in order to show the interval of redshifts in which these lines could be observed by the spectrometer IRS. Note that the Ne lines will be observable only for $z \leq 2$, and that Paα could be only observed in more distant sources.

We computed the nebular emission for some simulated galaxies used in GDS03 to determine if their emission lines can be observed by SIRTF.

The selected models are galaxies produced in dark matter halos with a total mass of $2.5 \cdot 10^{13}$ M$_\odot$ assumed to virialize at four different redshifts, namely z = 2, 3, 4 and

5. For each model, we computed the nebular emission for two extreme values of optical thickness of MCs $\tau_{\rm MC}$, namely 2 mag and 30 mag at 1 μm.

Figure 7.6 shows the expected fluxes of Brα (restframe wavelength $\lambda_{\rm Br\alpha} = 4.05\mu$m), Pa$\alpha$ ($\lambda_{\rm Pa\alpha} = 1.88\mu$m), [Ar II]7$\mu$m, [Ar III]9$\mu$m, [Ne II]12.8$\mu$m and [Ne III]15.5$\mu$m. The horizontal dotted lines refer to the 1-σ sensitivity for unresolved emission lines in 480 seconds with the high resolution mode of IRS; note that the sensitivity of the low resolution mode is an order of magnitude better. Results in fig. 7.6 suggest that spectroscopic observations with SIRTF can detect emission lines from spheroids in formation at high redshit, possibly up to redshift ≥ 4 in the most luminous cases. It is worth noting that objects at redshifts 1 or 2 are only 50% brighter than objects at $z \geq 4$. This is due to the higher star formation activity in halos that virialize at higher redshifts.

A lot of information can be obtained from the detection of such lines. The most obvious one is the redshift, that otherwise has to be estimated from photometric methods (with obvious uncertainties) or with spectroscopic follow-ups by 10-meter class ground-based telescopes. However, the dust obscuration can be high enough to preclude the observation of rest-frame UV-optical, while mid-IR lines suffer a much smaller obscuration. The measure of spectroscopic redshifts of these galaxies is fundamental in order to compute the redshift distribution of the different galaxy populations and to compute the luminosity function at the different redshifts and its evolution.

Furthermore, the Brα can provide a measure of the star formation rates in a way that is independent of estimations from the IR luminosity. Since, amongs bright hydrogen line, Brα is the less obscured one, it is the only line that can provide a reasonable estimation of the SFR without dust corrections.

Finally, as shown in the previous sections of this chapter, the above lines can be also used for the determination of metallicity, providing useful constrains on the models for chemical evolution of these objects.

We conclude that spectroscopic observations with SIRTF of SCUBA galaxies or star forming spheroids selected in the photometrics surveys can provide fundamental information on the formation process of elliptical galaxies. We will develop this discussion in the future to address a proposal for SIRTF observations.

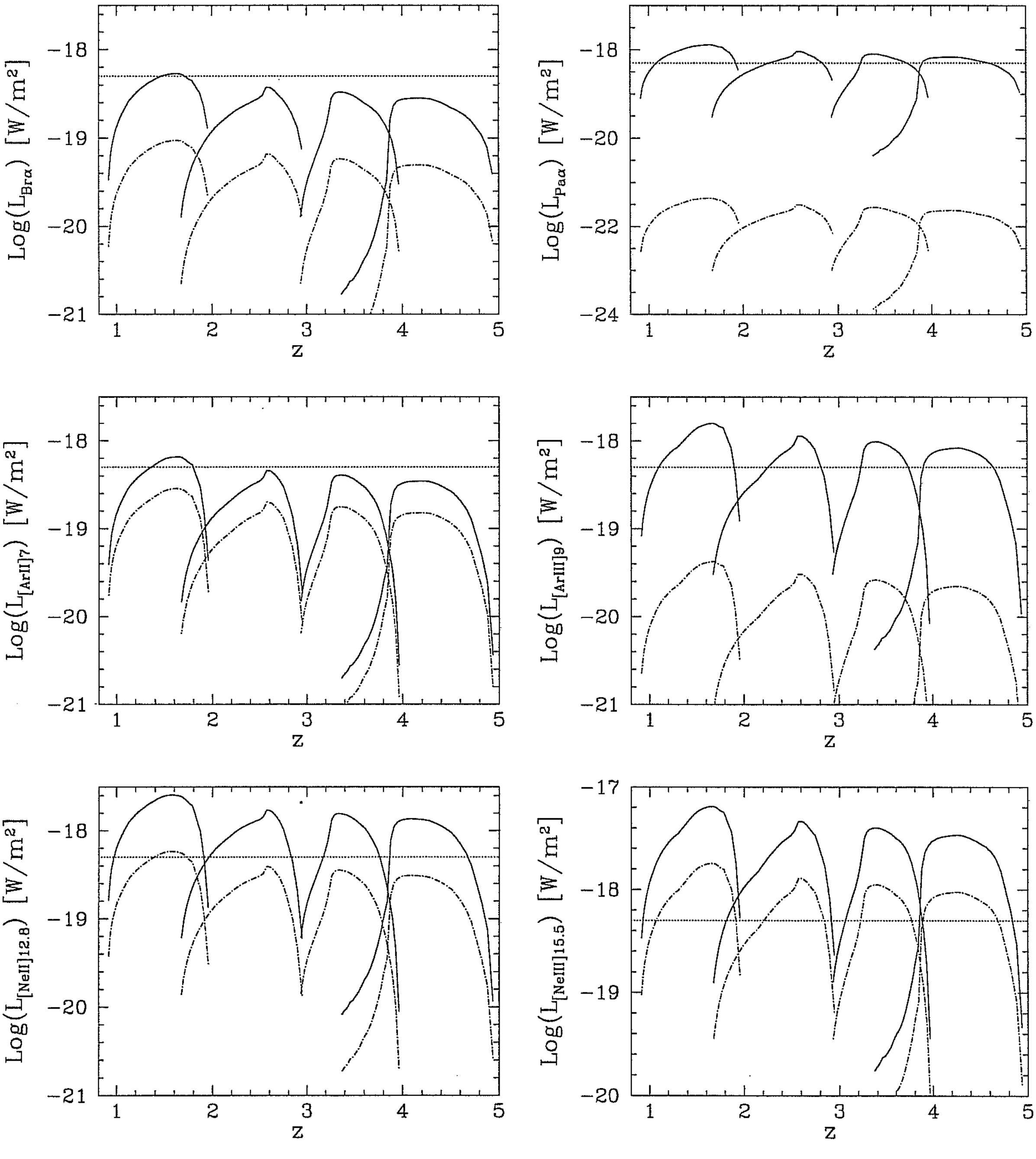

Figure 7.6: The expected observed fluxes for six near- and mid-infrared lines (form top-left: Brα, Paα, [Ar II]7μm, [Ar III]9μm, [Ne II]12.8μm, [Ne III]15.5μm) from massive spheroid galaxy models with different virialization redshifts, for $\tau_{MC} = 2$ (solid line) and 30 mag (dot-dashed line).

Chapter 8

Conclusions

The main topics and results of this thesis are summarized below:

1. We have built, with the photoionization code *Cloudy*, a new library of H II region models specifically designed to be used in models for population synthesis. The ionizing spectra has been represented with a suitable analytical form, that is a function of the ionizing fluxes for hydrogen, helium and O II (namely Q_{H}, Q_{He}, and Q_{O}). We checked that the analytical spectra reproduce the emission line luminosities of HII regions excited by SSPs within a reasonable accuracy provided that they have the same value for Q_{H}, Q_{He}, and Q_{O}. The main advantage of the procedure is that the HII region library can be used independently of the choice of the IMF and stellar atmosphere models, once Q_{H}, Q_{He}, and Q_{O} of ionizing populations are specified. The library can be freely retrieved from the web[1].

2. We have presented a general method to compute nebular emission in star-forming galaxies that uses the above library and we implemented it in the spectrophotometric code GRASIL. Now the code can simulate the complete SED of galaxies in great detail, from far UV to the radio wavelengths, including stellar absorption features, nebular emission, dust and PAH emission. Moreover, we can make a consinstent comparison between emission lines and the continuum. We have shown that emission lines provide new important constraints on the optical depth of molecular clouds, on the current metallicity, and on the shape of the emitted stellar continuum at wavelengths smaller than the Lyman break.

3. We applied the model to study the attenuation in normal star forming galaxies. The poor correlation between the extinction in the UV and of the Hα line found by Buat et al. (2002) is interpreted in our model as a natural consequence of age selective extinction. In fact, the UV (2000 Å) flux is also provided by stars that live more than 10 Myr, so it can be emitted by stars already outside parental molecular clouds. When the optical thickness of MCs grows over a critical value, the UV flux

---

[1] `http://www.sissa.it/~panuzzo/hii/` or `http://web.pd.astro.it/granato/grasil/grasil.html`

inside MCs is completely converted in dust emission and the observed flux comes from outside the MCs. In this case, the UV attenuation simply measure the ratio between the UV flux emitted outside MCs and the total emitted one, rather than measuring the MCs optical thikness. On the contrary, nebular emission is induced only by massive stars with a lifetime of a few Myr, and, if the escape time is not short enough, the nebular emission comes only from inside the MCs. In the case that the escape time is similar to the lifetime of ionizing stars, a fraction of line emission is produced outside MCs. This fraction can be important in the case of Hβ so that the Balmer decrement is changed, giving a lower measure of the attenuation than that suffered by MCs.

4. By converse, we found that $A_{\rm UV}$ correlates quite tightly with the ratio $F_{\rm FIR}/F_{\rm UV}$. This result confirms that even in normal spiral galaxies the FIR luminosity is produced by the reprocessed UV light of young stars, and that the contribution from absorbed optical light of old stars is small. We can conclude that the ratio $F_{\rm FIR}/F_{\rm UV}$ is a robust measure of UV attenuation.

5. We studied the attenuation properties of starburst galaxies. In particular we analyzed the sample of UV-bright starbursts by Wu et al. (2002). From the UV spectra we found that these objects have an attenuation law which presents a suppressed bump at 2175 Å, more similar to the Calzetti law than to the galactic one. We also compared the attenuation at Hα from the Balmer decrement and the attenuation at 2000 Å derived from the ratio $F_{\rm FIR}/F_{\rm UV}$; it results that these two quantities correlate, contrarily to what found in the case of normal galaxies. This result shows that in UV-bright starbursts UV, FIR and Hα are emitted by the same stellar population.

6. Using a set of simulations, we reproduced the observed diagram $F_{\rm FIR}/F_{\rm UV}$ vs β of UV-bright starbursts. The models seem to be bluer ($\Delta\beta \sim -0.5$) than the observed galaxies. This can be partially ascribed to the bump in the extinction law at 2175Å. Models also show a dust free spectral index around -2.5 which is 0.3 bluer than the expected one from the Meurer relation; this points to a different intrinsic UV spectral index in the stellar continuum, possibly due to an IMF different form the Salpeter one. The scatter of data around the mean relation does not allow a clear answer.

   The attenuation law extracted from the models show a reduced bump at 2175 Å although the adopted extinction law is similar to the galactic one. This is a consequence of age selective extinction which, as already pointed out by Granato et al. (2000), could at least in part explain the differences between the galactic and starburst attenuation laws.

7. Very Luminous IR galaxies observed by Goldader et al. (2002) do not follow the relation $F_{\rm FIR}/F_{\rm UV}$ vs. β found in UV-bright starbursts; they show a $F_{\rm FIR}/F_{\rm UV}$ larger by one or two orders of magnitude than that expected by the UV spectral

index. We are able to explain these observation as another consequence of age selective extinction. We notice that VLIRGs models follow a pattern in which we can identify three phases: a) The obscured phase, in which the burst is heavily obscured and what is seen in the UV band comes from older stellar population and the UV spectral index do not measure the attenuation of the burst population. b) The UV-bright phase, when the burst has consumed an important fraction of the gas and MCs become more transparent. The UV from the burst population is less obscured and the galaxy fall on the Meurer relation. c) The passive phase, when all the molecular gas is consumed the SFR goes to zero, and the galaxy evolves passively leaving the Meurer relation. It is worth noticing that only some UV-bright starbursts in Wu et al. sample are, possibly, the result of the above evolution.

8. We presented new calibrations for the SFR estimators obtained by using lines and continuum from the UV to radio wavelengths, and study the reliability of each estimator. NIR H recombination lines and radio luminosities are proved to be very accurate SFR estimators. In the case of normal spiral galaxies, the model evidences that Hα, UV and even IR estimators of SFR are affected by important scatters. For Hα, the age selective extinction can produce an underestimate of the attenuation when it is derived by the Balmer decrement. Also IR emission does not provide an accurate estimate of the SFR in disk galaxies, because the fraction of UV radiation not absorbed by the dust can be high. Anyhow, the UV luminosity corrected by using the ratio $F_{\rm FIR}/F_{\rm UV}$ is a robust SFR estimator, essentially because one recovers in the FIR what is lost in the UV. We also reproduced the observed value of the q ratio between radio and FIR emission. Its scatter in normal spiral galaxies is ascribed to the variation of extinction between different objects.

9. We presented some applications of infrared nebular lines. In particular we have provided a new calibration for the nitrogen abundance (N/H) as a function of the intensities of the [N II]122μm and [N III]57μm, and Brα lines. When the latter line is missing or useless (e.g. when affected by strong extinction), we suggest the possible use of the radio luminosity as indicator of the ionizing flux $Q_{\rm H}$, that enters implicitly the above calibration. We provide a new calibration of the metallicity with the ratio N_{23} defined by equation 7.8. This new calibration will turn out to be particularly useful for the Herschel experiment.

10. We were also able to explain the difference in the ratio [Ne III]15.5/[Ne II]12.8 between starbursts and galactic H II regions as the consequence of the presence of stars more massive than 30 $M_\odot$. This could be due to the smaller mass of young star clusters in our galaxies.

11. Finally, we estimated the luminosity of some near- and mid-IR emission lines from elliptical galaxies in formation at high redshift. The results show that these lines can be detected up to $z \sim 4$ by the SIRTF experiment, at least in the most luminous

cases. Thus, we discussed the possibility of a SIRTF spectroscopic follow-up of these objects selected from the SWIRE and the GOODS surveys.

Appendix A

The UV-bright sample

In this Appendix we report the results of our analysis of data from the UV-brigth starburst sample from Wu et al. (2002).

In table A.1 we reported the measured β together with its uncertinety $\Delta\beta$. Other computed quantities in table A.1 are the FIR luminosity (obtained from Helou's definition), the ratio $L_{\mathrm{FIR}}/L_{1600}$ and the luminosity at 5550 Å($L_{\mathrm{V}} = 5550 \cdot L_{5550}$).

Table A.1: Computed quantities for the Wu's sample.

Object	D [Mpc]	β	$\Delta\beta$	Log($L_{\mathrm{FIR}}/L_{1600}$)	Log($L_{\mathrm{FIR}}/L_{\odot}$)	Log($L_{\mathrm{V}}/L_{\odot}$)
Arp248B	0.00	-0.72	0.25	0.93	–	–
ESO185IG013	83.95	-1.40	0.22	–	–	9.59
ESO296IG011	82.79	-2.01	0.66	0.72	10.02	9.47
ESO338IG004	43.05	-2.04	0.06	-0.22	9.59	9.51
ESO383G044	60.53	-1.04	0.55	0.57	9.93	–
ESO572G034	15.70	-2.13	0.14	-0.02	8.52	8.01
IC1586	91.20	-0.78	0.28	0.57	10.14	9.80
IC214	139.32	-0.74	0.40	1.16	11.22	9.93
IC2184	60.53	-2.09	0.46	0.97	10.17	–
IC2458	29.24	-2.99	0.52	–	–	–
Mkn116	16.52	-2.39	0.22	–	–	–
Mkn1267	90.36	-0.98	0.25	–	–	9.88
Mkn153	43.05	-2.01	0.11	–	–	–
Mkn170	21.38	-2.60	0.39	0.50	8.42	–
Mkn19	60.43	-1.42	0.11	–	–	–
Mkn209	5.70	-1.80	0.16	–	–	–
Mkn220	70.60	-1.36	0.14	–	–	–
Mkn25	45.29	-1.93	0.18	0.48	9.59	–
Mkn309	196.79	1.33	0.29	–	–	10.37
Mkn33	28.31	-1.57	0.14	0.42	9.74	–
Mkn357	226.98	-1.40	0.40	0.07	10.84	10.23
Mkn36	8.39	-1.68	0.10	–	–	–

Table A.1: Continue.

Object	D [Mpc]	β	$\Delta\beta$	$\mathrm{Log}(L_{\mathrm{FIR}}/L_{1600})$	$\mathrm{Log}(L_{\mathrm{FIR}}/L_{\odot})$	$\mathrm{Log}(L_{\mathrm{V}}/L_{\odot})$
Mkn477	179.47	-1.29	0.20	0.68	10.82	–
Mkn487	16.00	-1.27	0.22	–	–	7.81
Mkn499	123.03	-0.74	0.20	–	–	9.97
Mkn542	209.89	-1.94	0.23	–	–	10.37
Mkn54	113.24	-1.74	0.09	0.18	10.33	–
Mkn66	94.22	-1.39	0.17	0.15	9.88	9.63
Mkn789	52.24	-0.77	0.31	1.50	10.17	–
Mkn7	43.68	-2.23	0.37	0.13	9.22	–
Mkn829	24.89	-1.90	0.04	-0.11	8.88	8.45
Mkn960	91.22	-1.35	0.18	0.23	10.25	9.81
NGC1140	22.70	-1.53	0.05	0.22	9.44	9.15
NGC1313	4.33	-0.99	0.17	1.42	8.74	7.33
NGC1510	13.00	-1.62	0.13	-0.01	8.36	8.36
NGC1569	1.73	-1.62	0.16	-0.38	8.29	7.96
NGC1614	72.11	-0.84	0.20	1.86	11.38	10.11
NGC1672	17.95	-0.12	0.10	1.51	10.29	–
NGC1705	7.80	-2.38	0.04	-0.70	7.99	8.16
NGC1800	10.67	-1.88	0.13	0.23	8.23	8.19
NGC1808	13.49	0.83	0.41	3.03	10.42	9.09
NGC2403	3.21	-0.95	0.20	2.12	8.66	6.25
NGC2415	61.09	-0.49	0.22	0.87	10.71	–
NGC2537	6.89	-1.74	0.25	0.90	8.44	–
NGC2782	43.45	-1.11	0.07	1.05	10.44	–
NGC2798	31.48	-0.17	0.40	1.96	10.49	–
NGC3049	26.18	-1.10	0.12	0.70	9.49	8.82
NGC3125	15.42	-1.20	0.14	0.42	9.23	8.54
NGC3256	41.11	0.11	0.23	1.85	11.36	9.84
NGC3310	20.70	-1.13	0.12	0.81	10.30	–
NGC3353	20.23	-1.52	0.14	–	–	–
NGC3395	30.34	-1.44	0.28	–	–	–
NGC3396	30.48	-1.36	0.47	–	–	–
NGC3448	26.79	-0.90	0.22	1.18	9.86	–
NGC3504	29.38	-0.38	0.12	1.31	10.47	–
NGC3690	52.00	-1.21	0.13	2.02	11.60	–
NGC3991	53.46	-1.65	0.04	–	–	–
NGC3995	54.45	-0.68	0.14	0.79	10.13	–
NGC4194	44.26	-0.36	0.13	1.52	10.80	9.78
NGC4214	4.09	-1.55	0.09	–	–	–
NGC4385	36.81	-0.96	0.18	0.87	9.98	9.30
NGC4449	2.92	-1.76	0.04	–	–	–
NGC4500	53.46	-0.66	0.12	1.00	10.26	–
NGC4670	16.67	-1.53	0.11	0.10	9.09	–

Table A.1: Continue.

Object	D [Mpc]	β	$\Delta\beta$	Log($L_{\rm FIR}/L_{1600}$)	Log($L_{\rm FIR}/L_{\odot}$)	Log($L_{\rm V}/L_{\odot}$)
NGC4853	120.23	-0.21	0.36	1.21	10.26	–
NGC4861	12.47	-2.15	0.06	–	–	7.97
NGC5102	3.12	-0.48	0.17	-0.07	7.24	8.14
NGC5236	4.37	-0.85	0.10	1.05	9.59	8.69
NGC5253	2.50	-1.24	0.11	0.61	8.43	7.48
NGC5860	77.09	-0.67	0.34	0.76	10.23	9.86
NGC5996	54.70	-1.19	0.21	0.85	10.32	9.59
NGC6052	76.21	-0.74	0.11	0.90	10.78	10.00
NGC6090	126.34	-0.51	0.18	1.20	11.22	10.18
NGC6217	27.29	-0.66	0.10	1.15	10.14	9.27
NGC6221	21.38	-0.66	0.46	–	–	9.27
NGC7250	22.39	-1.83	0.19	0.38	9.42	8.84
NGC7496	23.66	-1.13	0.13	1.25	9.92	8.99
NGC7552	22.70	0.32	0.12	2.02	10.77	9.59
NGC7673	54.70	-1.18	0.10	0.65	10.36	9.84
NGC7714	43.85	-1.16	0.08	–	–	9.72
NGC7793	6.19	-1.27	0.12	1.47	8.97	7.82
UGC4305	3.05	-2.08	0.28	0.38	7.31	–
UGC8315	16.62	-2.11	0.62	–	–	–

Figure A.1 and A.2 show the UV spectra of the galaxies with the appropriate fit $F_{\lambda} \propto \lambda^{\beta}$.

Figure A.3, A.4, A.5 and A.6 show the fits of spectral regions around Hα and Hβ, while in table A.2 we reported the luminosities of such lines.

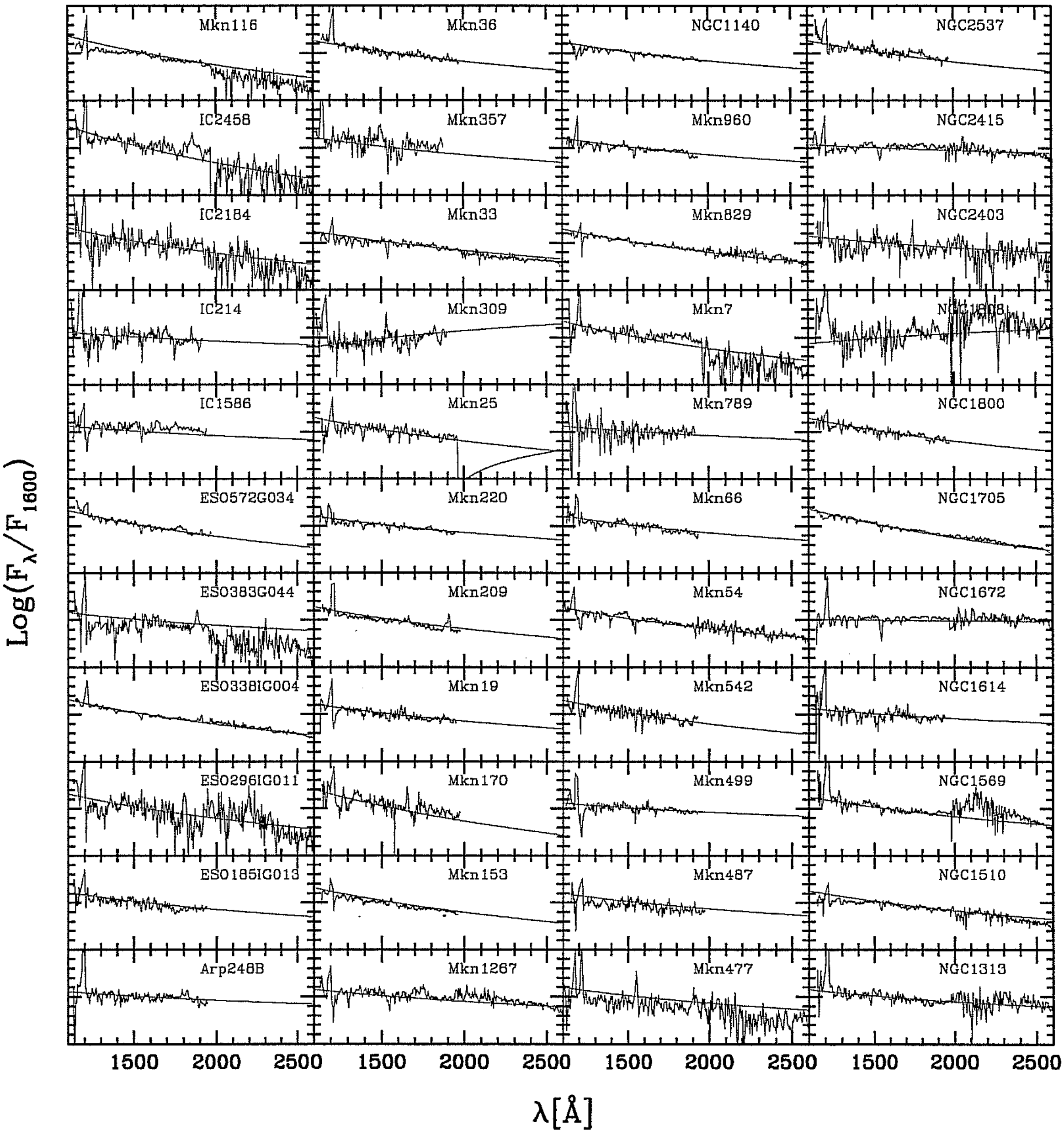

Figure A.1: UV spectra of first 44 objects of the sample compared with the appropriate fit.

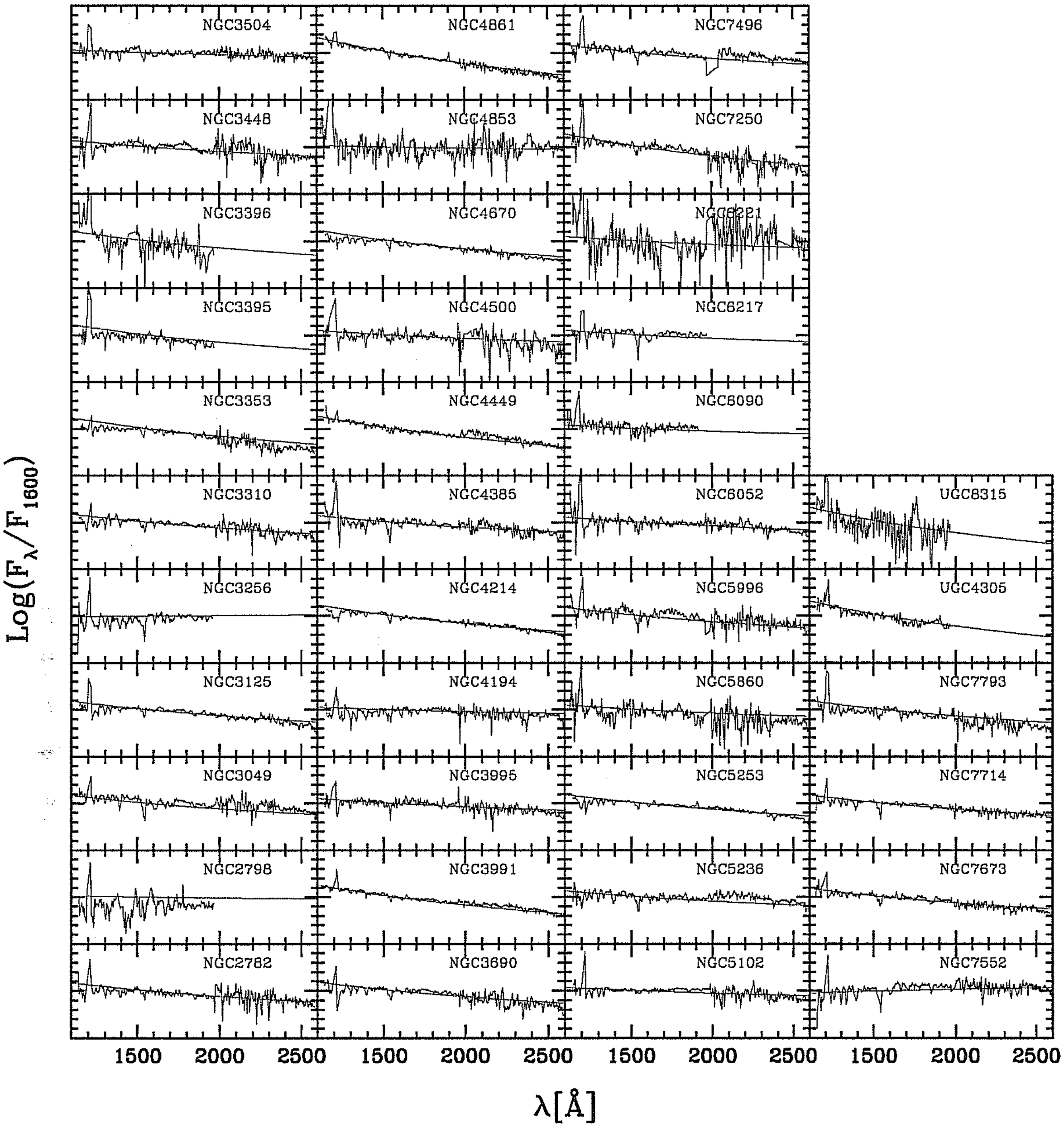

Figure A.2: As fig. A.1, but for the remaining objects.

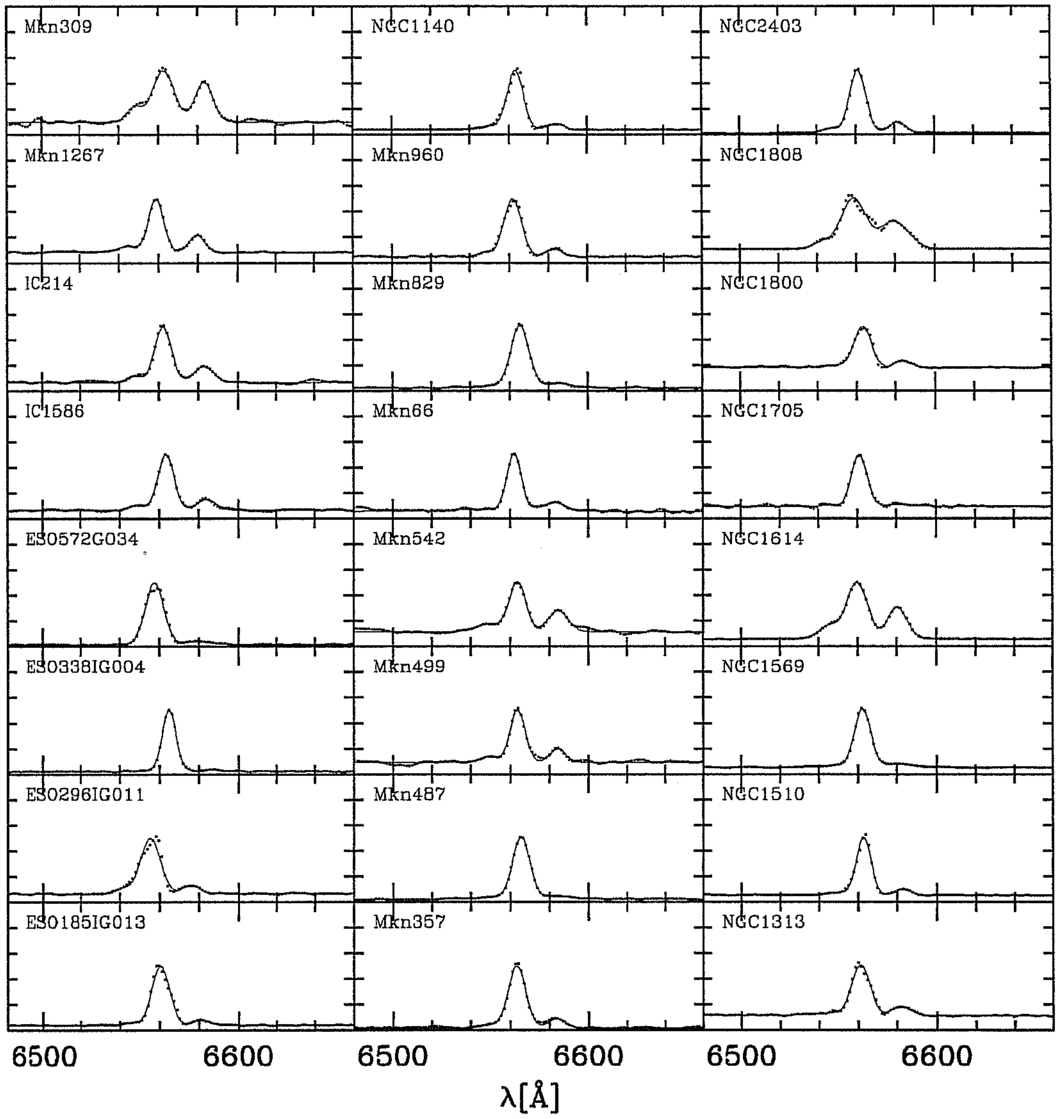

Figure A.3: Optical spectra of first 24 galaxies of the sample in the region around Hα. The flux is in ordinate and in linear scale; the latter is different form an object to another and was chosen from the value of the continuum and the emission line. Small dots are data, tiny lines show the fitting function.

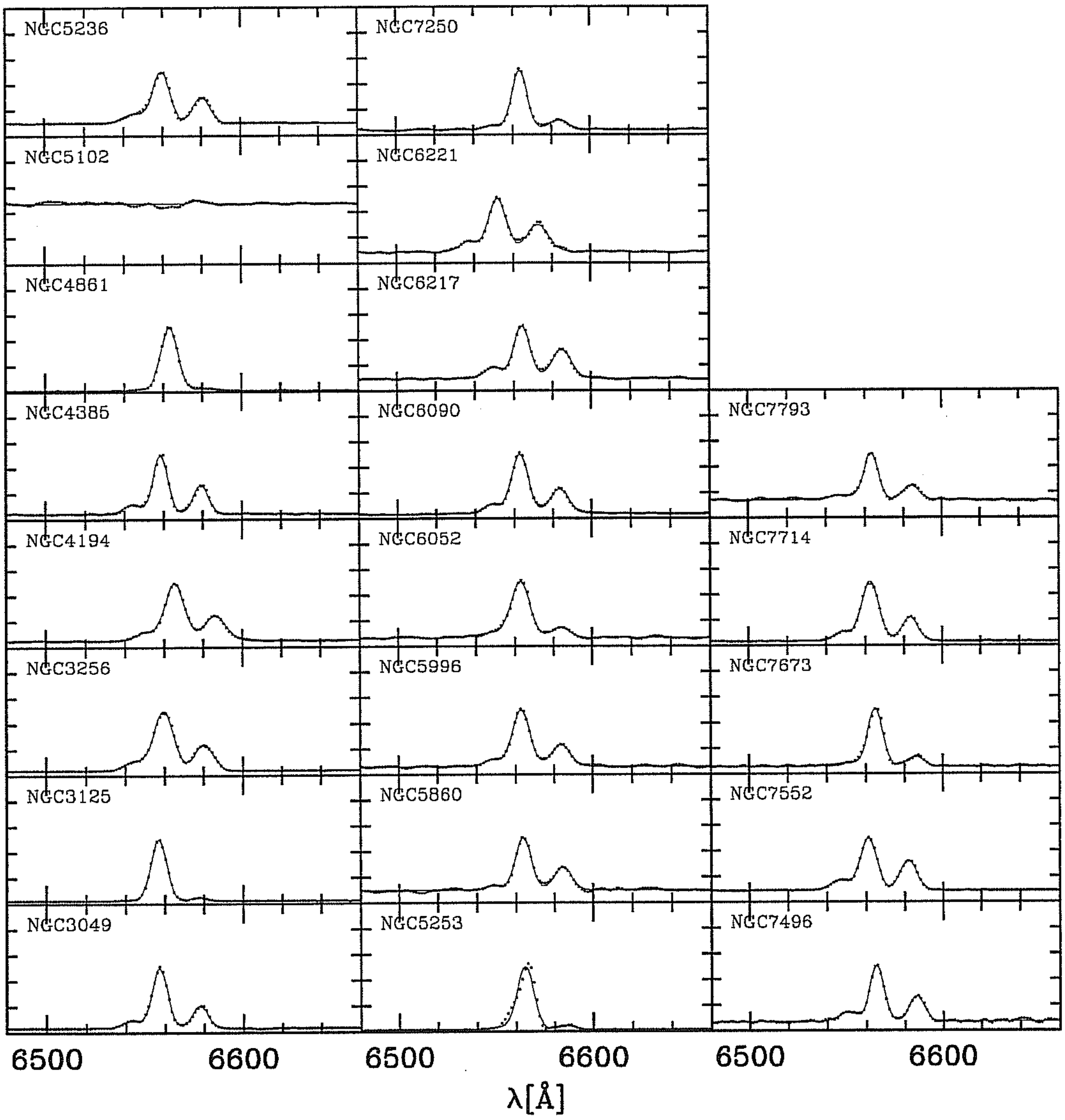

Figure A.4: As previous figure but for the following galaxies.

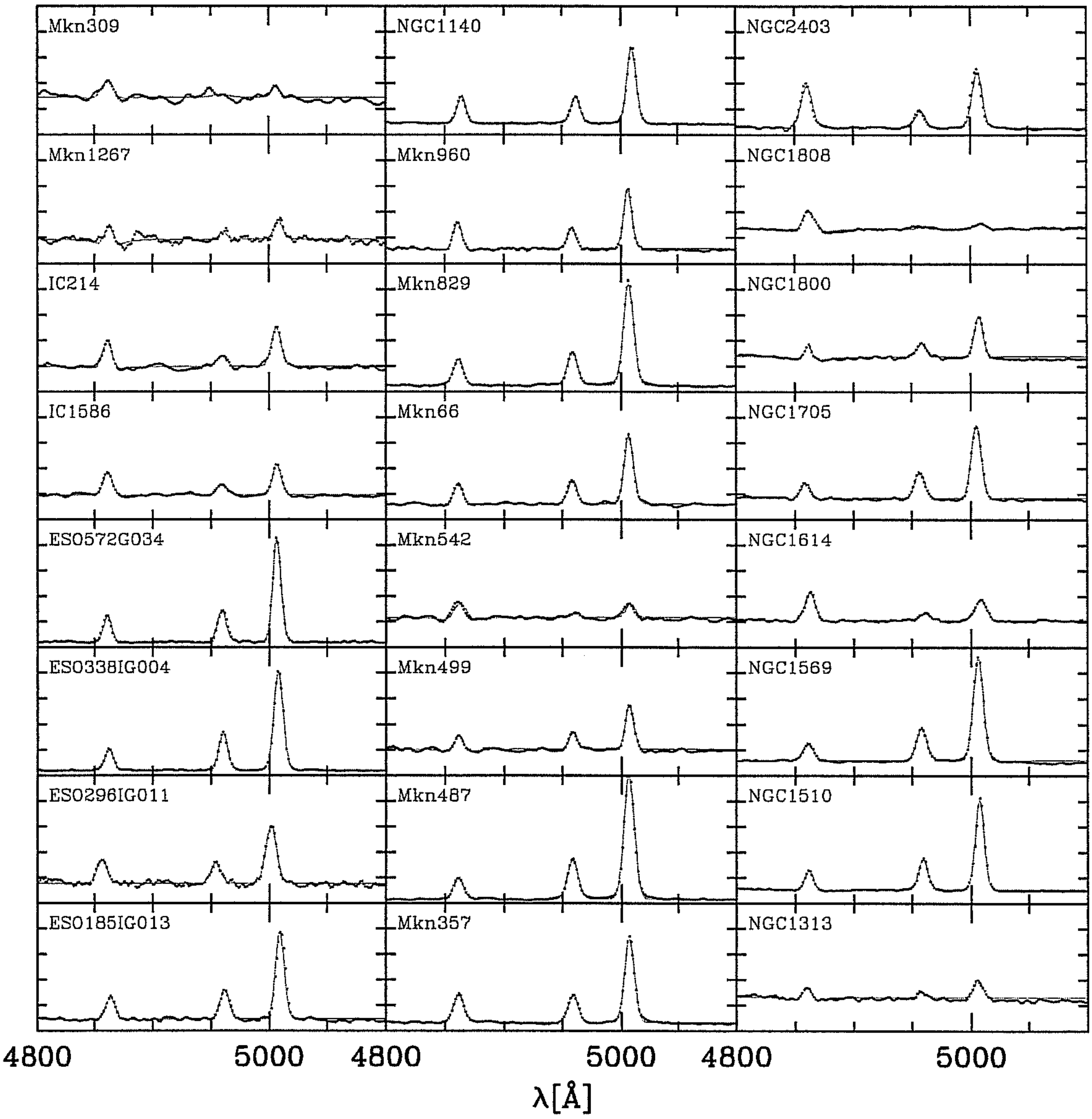

Figure A.5: As fig. A.3 but for the spectral region around Hβ.

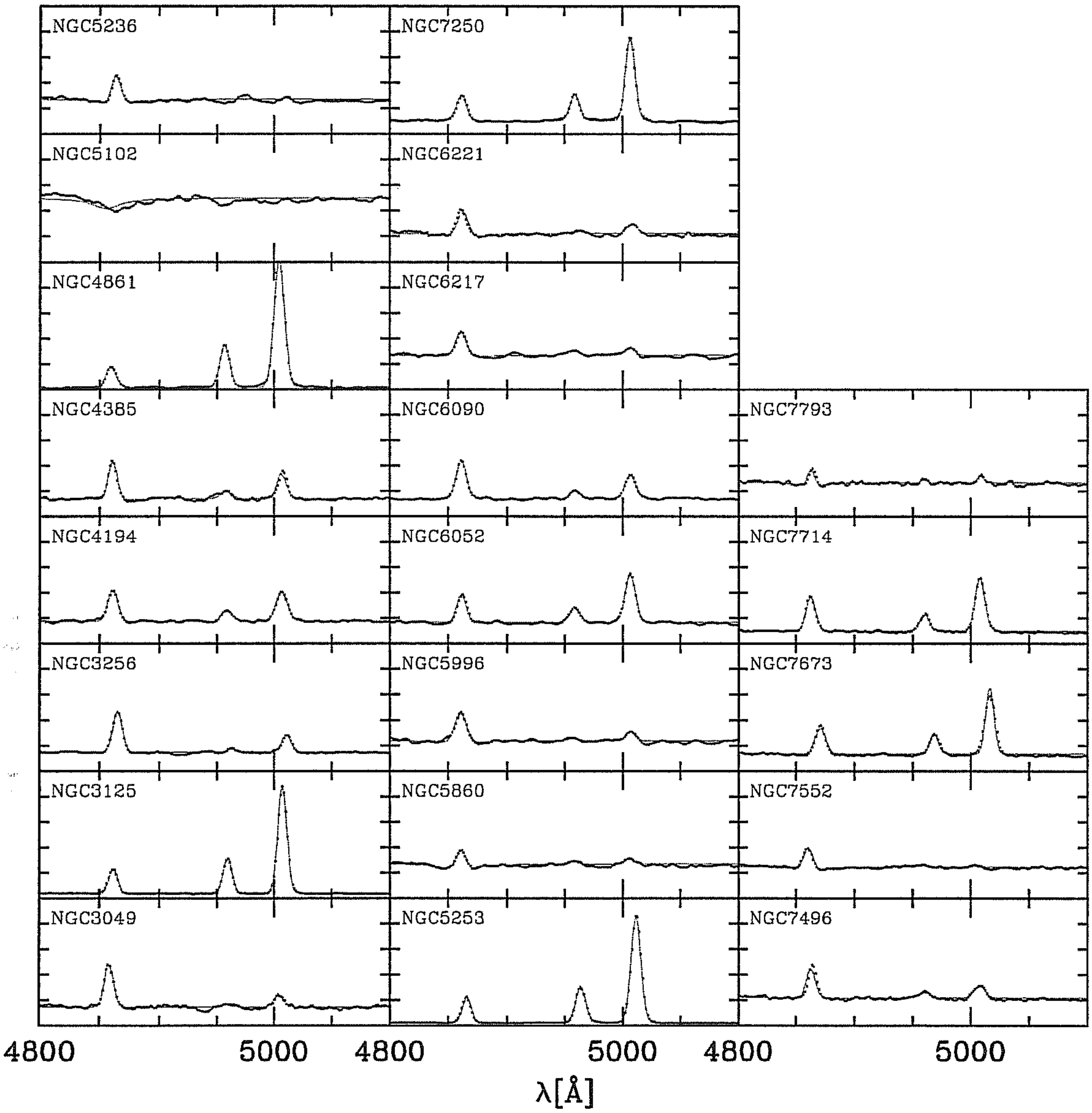
NGC5236
NGC5102
NGC4861
NGC4385
NGC4194
NGC3256
NGC3125
NGC3049
NGC7250
NGC6221
NGC6217
NGC6090
NGC6052
NGC5996
NGC5860
NGC5253
NGC7793
NGC7714
NGC7673
NGC7552
NGC7496
4800
5000
4800
5000
4800
5000
λ[Å]

Figure A.6:

Table A.2: Luminosity of optical lines for the Wu's sample. The luminosities are expressed in logaritmic scale, in unit of 10^{30} W.

Object	Hα	Hβ	[O II]3727	[O III]4960	[O III]5007	[N II]6549	[N II]6585
ESO185IG013	4.42	3.86	4.35	3.94	4.39	2.88	3.33
ESO296IG011	4.14	3.49	4.06	3.39	3.90	3.08	3.26
ESO338IG004	4.49	4.02	4.38	4.27	4.72	2.77	3.15
ESO572G034	3.31	2.56	2.99	2.64	3.14	1.28	2.22
IC1586	4.41	3.79	4.26	3.32	3.76	3.35	3.77
IC214	4.61	3.83	3.99	3.42	4.00	3.62	4.14
Mkn1267	4.33	3.88	4.01	3.17	3.62	3.48	3.84
Mkn309	4.86	4.19	3.72	3.30	3.69	4.16	4.67
Mkn357	5.35	4.78	5.05	4.75	5.24	4.05	4.53
Mkn487	3.01	2.43	2.53	2.74	3.24	1.89	1.92
Mkn499	4.36	3.76	4.14	3.60	4.05	3.43	3.80
Mkn542	4.70	4.35	4.54	3.42	3.92	4.13	4.42
Mkn66	4.13	3.80	4.23	3.74	4.23	3.48	3.49
Mkn829	3.61	3.04	3.46	3.16	3.67	2.53	2.64
Mkn960	4.57	3.99	–	3.83	4.30	3.29	3.67
NGC1140	3.95	3.39	3.88	3.42	3.88	2.87	2.98
NGC1313	1.62	1.12	1.67	0.36	0.96	0.76	0.90
NGC1510	3.02	2.42	2.87	2.61	3.08	1.88	2.04
NGC1569	2.55	2.03	2.36	2.32	2.82	1.55	1.63
NGC1614	4.94	4.02	4.15	3.36	3.89	4.27	4.65
NGC1705	2.52	1.98	2.36	2.18	2.63	0.89	1.44
NGC1800	2.24	1.66	2.48	1.68	2.13	1.19	1.42
NGC1808	3.73	2.82	2.50	1.67	2.15	2.85	3.56
NGC2403	1.56	1.06	1.36	0.61	1.13	0.41	0.80
NGC3049	3.67	3.05	3.16	1.85	2.52	2.84	3.25
NGC3125	3.67	3.14	3.46	3.31	3.80	2.11	2.49
NGC3256	4.83	4.05	4.14	2.94	3.68	4.06	4.46
NGC4194	4.64	3.78	4.02	3.36	3.83	3.83	4.33
NGC4385	4.21	3.46	3.68	2.86	3.30	3.49	3.92
NGC4861	3.58	3.01	–	3.34	3.85	2.10	2.34
NGC5102	0.55	–	1.41	–	–	–	–
NGC5236	3.08	2.48	2.37	–	1.01	2.45	2.78
NGC5253	2.79	2.33	2.62	2.55	3.01	1.53	1.63
NGC5860	4.34	3.67	3.50	2.73	2.99	3.24	4.01
NGC5996	4.29	3.58	3.51	2.48	2.96	3.33	3.90
NGC6052	4.67	4.03	4.60	3.81	4.34	3.80	3.92
NGC6090	5.15	4.40	4.55	3.73	4.22	4.30	4.82
NGC6217	3.79	3.04	3.00	2.36	2.46	3.13	3.61
NGC6221	3.91	3.26	3.08	2.15	2.68	3.18	3.70
NGC7250	3.63	3.05	3.60	3.07	3.56	2.42	2.91
NGC7496	3.58	2.86	1.89	2.19	2.53	2.94	3.27
NGC7552	4.12	3.43	3.29	2.22	1.88	3.45	3.88
NGC7673	4.50	4.02	4.41	3.80	4.30	3.52	3.78
NGC7714	4.69	4.08	4.42	3.79	4.29	3.81	4.25
NGC7793	2.00	1.49	1.71	0.49	0.81	1.27	1.55

Table A.3: Equivalent width (in Å) of optical lines for the Wu's sample. Negative values mean net emissions.

Object	EW(Hα+[N II])	EW(Hβ)	EW(Hδ)	EW([O II]3727)	EW([O III]5007)
ESO185IG013	-142.55	-13.04	1.94	-52.62	-78.93
ESO296IG011	-101.57	-6.99	6.88	-48.35	-35.52
ESO338IG004	-191.47	-34.11	-6.95	-75.29	-200.89
ESO572G034	-387.90	-33.21	-2.38	-107.25	-189.10
IC1586	-85.54	-5.81	1.98	-41.35	-13.08
IC214	-92.30	-7.39	5.72	-18.27	-18.17
Mkn1267	-70.59	-4.57	4.22	-24.21	-6.41
Mkn309	-105.18	-1.72	1.27	-2.39	-4.34
Mkn357	-343.68	-37.20	-2.29	-40.05	-95.63
Mkn487	-278.82	-45.98	-5.71	-55.82	-245.69
Mkn499	-58.42	-2.08	3.94	-20.29	-16.69
Mkn542	-56.42	-4.36	1.11	-28.25	-6.49
Mkn66	-78.57	-7.91	3.17	-46.10	-42.56
Mkn829	-278.55	-30.28	-8.97	-108.98	-146.83
Mkn960	-124.52	-10.24	2.60	–	-40.71
NGC1140	-142.13	-18.28	2.09	-65.28	-67.04
NGC1313	-47.52	0.28	5.32	-25.44	-6.67
NGC1510	-90.22	-6.89	5.34	-46.07	-66.39
NGC1569	-100.74	-7.84	2.00	-13.46	-75.10
NGC1614	-170.98	-8.54	4.28	-20.68	-10.20
NGC1705	-44.17	-2.10	4.22	-14.78	-41.06
NGC1800	-22.75	1.56	6.59	-29.49	-12.54
NGC1808	-98.15	-2.84	4.09	-10.84	-1.96
NGC2403	-479.03	-60.07	-7.51	-59.20	-78.43
NGC3049	-194.94	-20.13	0.26	-30.24	-9.08
NGC3125	-231.92	-37.62	-3.59	-70.94	-233.76
NGC3256	-248.11	-19.23	1.11	-27.53	-10.77
NGC4194	-161.13	-14.70	0.18	-30.67	-16.11
NGC4385	-165.96	-14.95	0.13	-49.27	-17.42
NGC4861	-845.99	-41.71	–	–	-378.82
NGC5102	0.84	7.29	8.39	-4.35	-0.07
NGC5236	-75.25	-2.48	3.88	-7.29	-0.71
NGC5253	-466.36	-76.16	-8.86	-120.14	-347.18
NGC5860	-68.82	1.06	5.22	-8.74	-3.21
NGC5996	-121.88	-8.20	-0.82	-10.26	-2.73
NGC6052	-99.73	-9.41	0.85	-50.77	-26.67
NGC6090	-225.56	-21.91	-1.24	-33.87	-16.12
NGC6217	-87.13	-5.22	2.01	-8.38	-2.18
NGC6221	-98.64	-2.88	1.72	-15.88	-4.58
NGC7250	-140.77	-16.35	-0.80	-60.16	-64.14
NGC7496	-95.70	-8.28	0.85	-1.48	-7.28
NGC7552	-89.91	-2.09	5.71	-10.62	-0.07
NGC7673	-100.16	-14.36	2.04	-51.71	-35.60
NGC7714	-232.16	-27.63	-2.45	-61.24	-50.34
NGC7793	-37.38	-0.21	5.61	-16.94	-1.55

Bibliography

Achtermann, J. M. & Lacy, J. H., 1995, *Structures and kinematics within the starburst nucleus of M82: searching for a bar*, *ApJ*, **439**, 163

Aller, L. H., 1984, *Physics of Thermal Gaseous Nebulae*, Vol. 112, Astrophysics & Space Science Library

Balzano, V. A., 1983, *Star-burst galactic nuclei*, *ApJ*, **268**, 602

Bell, E., 2003, *Estimating Star Formation Rates from Infrared and Radio Luminosities: The Origin of the Radio-Infrared Correlation*, *ApJ*, **586**, 794

Binette, L., Magris, C. G., Stasińska, G., & Bruzual, A. G., 1994, *Photoionization in elliptical galaxies by old stars*, *A&A*, **292**, 13

Boselli, A., Gavazzi, G., Donas, J., & Scodeggio, M., 2001, *1.65 micron (H band) surface photometry of galaxies. VI. The history of star formation in normal late-type galaxies*, *AJ*, **121**, 753

Bressan, A., Chiosi, C., & Fagotto, F., 1994, *Spectrophotometric evolution of elliptical galaxies. 1: Ultraviolet excess and color-magnitude-redshift relations*, *ApJS*, **94**, 63

Bressan, A., Silva, L., & Granato, G. L., 2002, *Far infrared and radio emission in dusty starburst galaxies*, *A&A*, **392**, 377

Buat, V., Boselli, A., Gavazzi, G., & Bonfanti, C., 2002, *Star formation rate and dust extinction in nearby star-forming and starburst galaxies*, *A&A*, **383**, 801

Buat, V., Donas, J., Millard, B., & Xu, C., 1999, *Far infrared and Ultraviolet emissions of individual galaxies at z=0: selection effects on the estimate of the dust extinction*, *A&A*, **352**, 371

Burgess, A. & Summers, H. P., 1976, *The recombination and level populations of ions. I - Hydrogen and hydrogenic ions*, *MNRAS*, **174**, 345

Calzetti, D., 1997, *Reddening and star formation in starburst galaxies*, *AJ*, **113**, 162

Calzetti, D., Armus, L., Bohlin, R. C., Kinney, A. L., Koornneef, J., & Storchi-Bergmann, T., 2000, *The dust content and opacity of actively star-forming galaxies*, *ApJ*, **533**, 682

Calzetti, D. & Heckman, T. M., 1999, *The evolution of dust opacity in galaxies*, *ApJ*, **519**, 27

Calzetti, D., Kinney, A. L., & Storchi-Bergmann, T., 1994, *Dust extinction of the stellar continua in starburst galaxies: the ultraviolet and otical extinction law*, *ApJ*, **429**, 582

Calzetti, D., Kinney, A. L., & Storchi-Bergmann, T., 1996, *Dust obcuration in starburst* *galaxies from near-infrared spectroscopy*, *ApJ*, **458**, 132

Cardelli, J. A., Clayton, G. C., & Mathis, J. S., 1989, *The relationship between infrared, optical, and ultraviolet extinction*, *ApJ*, **345**, 245

Carilli, C. L., 2002, *Radio observations of high redshift star forming galaxies*, *American Astronomical Society Meeting*, **200**, 5113

Chabrier, G., 2003, *Galactic Stellar and Substellar Initial Mass Function*, *PASP*, **115**, 763

Charlot, S. & Fall, S. M., 2000, *A simple model for the absorption of starlight by dust in galaxies*, *ApJ*, **539**, 718

Charlot, S. & Longhetti, M., 2001, *Nebular emission from star-forming galaxies*, *MNRAS*, **323**, 887

Cimatti, A., Andreani, P., Rottgering, H., & Tilanus, R., 1998, *Vigorous star formation hidden by dust in a galaxy at a redshift of 1.4*, *Nature*, **392**, 895

Code, A. D. & Welch, G. A., 1982, *Ultraviolet photometry from the Orbiting Astronomical Observatory. XL. The energy distributions of spiral and irregular galaxies*, *ApJ*, **256**, 1

Colbert, J. W., Malkan, M. A., Clegg, P. E., Cox, P., Fischer, J., Lord, S. D., Luhman, M., Satyapal, S., Smith, H. A., Spinoglio, L., Stacey, G., & Unger, S. J., 1999, *ISO LWS spectroscopy of M82: a nuified evolutionary model*, *ApJ*, **511**, 721

Condon, J. J., 1974, *Confusion and Flux-Density Error Distributions*, *ApJ*, **188**, 279

Condon, J. J., 1992, *Radio emission from normal galaxies*, *ARA&A*, **30**, 575

Conti, P. S., 1991, *Wolf-Rayet galaxies - an introduction and a catalog*, *ApJ*, **377**, 115

Contini, M. & Viegas, S. M., 2001, *A Grid of Composite Models for the Simulation of Starburst Galaxy and H II Region Spectra*, *ApJS*, **137**, 75

de Grijs, R., O'Connell, R. W., & Gallagher, J. S., 2001, *The Fossil Starburst in M82*, *AJ*, **121**, 768

DeGioia-Eastwood, K., 1992, *IRAS observations and the stellar content of HII regions in the large magellanic cloud*, *ApJ*, **397**, 542

Dessauges-Zavadsky, M., Pindao, M., Maeder, A., & Kunth, D., 2000, *Spectral classification of emission-line galaxies*, *A&A*, **355**, 89

Dey, A., Graham, J. R., Ivison, R. J., Smail, I., Wright, G. S., & Liu, M. C., 1999, *Observations of a Z = 1.44 Dusty, Ultraluminous Galaxy and Implications for Deep Submillimeter Surveys*, *ApJ*, **519**, 610

Doane, J. S. & Mathews, W. G., 1993, *Stellar evolution in the starburst galaxy M82: evidence for a top-heavy initial mass function*, *ApJ*, **419**, 573

Draine, B. T. & Lee, H. M., 1984, *Optical propreties of interstellar graphite and silicate grain*, *ApJ*, **285**, 89

Dressler, A., Smail, I., Poggianti, B. M., Butcher, H., Couch, W. J., Ellis, R. S., & Oemler, A., 1999, *A spectroscopic catalog of 10 distant rich clusters of galaxies*, *ApJS*, **122**, 51

Evans, A. S., Sanders, D. B., Cutri, R. M., Radford, S. J. E., Surace, J. A., Solomon, P. M., Downes, D., & Kramer, C., 1998, *Near-Infrared Spectroscopy and a Search for CO Emission in Three Extremely Luminous IRAS Sources: IRAS F09105+4108,* *IRAS F15307+3252, and PG 1634+706*, *ApJ*, **506**, 205

Ferland, G. J., 1980, *Hydrogenic emission and recombination coefficients for a wide range of temperature and wavelength*, *PASP*, **92**, 596

Ferland, G. J., 2003, *Quantitative spectroscopy of photoionized clouds*, *ARA&A*, **41**, 517

Fioc, M. & Rocca-Volmerange, B., 1997, *PEGASE: a UV to NIR spectral evolution model of galaxies*, *A&A*, **326**, 950

Franceschini, A., Silva, L., Fasano, G., Granato, G. L., Bressan, A., Arnouts, S., & Danese, L., 1998, *Early-type galaxies in the hubble deep field: the star formation history*, *ApJ*, **506**, 600

Fuente, A., Neri, R., Martín-Pintado, J., Bachiller, R., Rodríguez-Franco, A., & Palla, F., 2001, *Disks and outflows around intermediate-mass stars and protostars*, *A&A*, **366**, 873

García-Vargas, M. L., Bressan, A., & Díaz, A. I., 1995a, *Evolutionary models for giant extragalactic HII regions at different metallicities*, *A&AS*, **112**, 13

García-Vargas, M. L., Bressan, A., & Díaz, A. I., 1995b, *Predicted emission line from giant HII regions ionized by aging star clusters*, *A&AS*, **112**, 35

Gavazzi, G., Bonfanti, C., Sanvito, G., Boselli, A., & Scodeggio, M., 2002, *Spectrophotometry of Galaxies in the Virgo Cluster. I. The Star Formation History*, *ApJ*, **576**, 135

Genzel, R., Lutz, D., Sturm, E., Egami, E., Kunze, D., Moorwood, A. F. M., Rigopoulou, D., Spoon, H. W. W., Sternberg, A., Tacconi-Garman, L. E., Tacconi, L., & Thatte, N., 1998, *What powers ultraluminous IRAS galaxies?*, *ApJ*, **498**, 579

Giveon, U., Sternberg, A., Lutz, D., Feuchtgruber, H., & Pauldrach, A. W. A., 2002, *The excitation and metallicity of galactic HII regions from Infrared Space Observatory SWS observations of mid-infrared fine-structure lines*, *ApJ*, **566**, 880

Goldader, J. D., Meurer, G., Heckman, T. M., Seibert, M., Sanders, D. B., Calzetti, D., & Steidel, C. C., 2002, *Far-Infrared galaxies in the far ultraviolet*, *ApJ*, **568**, 651

Gordon, K. D., Clayton, G. C., Witt, A. N., & Misselt, K. A., 2000, *The flux ratio method for determining the dust attenuation of starburst galaxies*, *ApJ*, **533**, 236

Graham, J. R. & Dey, A., 1996, *The Redshift of an Extremely Red Object and the Nature of the Very Red Galaxy Population*, *ApJ*, **471**, 720

Granato, G. L. & Danese, L., 1994, *Thick Tori around Active Galactic Nuclei - a Comparison of Model Predictions with Observations of the Infrared Continuum and Silicate Features*, *MNRAS*, **268**, 235

Granato, G. L., De Zotti, G., Silva, L., Bressan, A., & Danese, L., 2003, *A physical model for the co-evolution of QSOs and their spheroidal hosts*, *ApJ*, , submitted (GDS03)

Granato, G. L., Lacey, C. G., Silva, L., Bressan, A., Baugh, C. M., Cole, S., & Frenk, C. S., 2000, *The infrared side of galaxy formation. I. The local universe in the semi-analytical framework*, *ApJ*, **542**, 710

Granato, G. L., Silva, L., Monaco, P., Panuzzo, P., Salucci, P., Zotti, G. D., & Danese, L., 2001, *Joint formation of QSOs and spheroids: QSOs as clocks of star formation in spheroids*, *MNRAS*, **324**, 757

Gu, Q. S., Huang, J. H., de Diego, J. A., Dultzin-Hacyan, D., Lei, S. J., & Benítez, E., 2001, *The nuclear starburst activity in the Seyfert 2 galaxy NGC 7679*, *A&A*, **374**, 932

Guhathakurta, P. & Draine, B. T., 1989, *Temperature fluctuations in interstellar grains. I. Computational method and sublimation of small grains*, *ApJ*, **345**, 230

Guiderdoni, B. & Rocca-Volmerange, B., 1987, *A model of spectrofotometric evolution for high-redshift galaxies*, *A&A*, **186**, 1

Haarsma, D. B., Partridge, R. B., Windhorst, R. A., & Richards, E. A., 2000, *Faint Radio Sources and Star Formation History*, *ApJ*, **544**, 641

Heiles, C., 1994, *On the origin of the diffuse C^+ 158 micron line emission*, *ApJ*, **436**, 720

Helou, G., Khan, I. R., Malek, L., & Boehmer, L., 1988, *IRAS observations of galaxies in the Virgo cluster area*, *ApJS*, **68**, 151

Hirashita, H., Buat, V., & Inoue, A. K., 2003, *Star formation rate in galaxies from UV, IR, and H-alpha estimators*, *A&A*, , accepted

Hopkins, A. M., Connolly, A. J., Haarsma, D. B., & Cram, L. E., 2001, *Toward a resolution of the discrepancy between different estimators of star formation rate*, *AJ*, **122**, 288

Houck, J. R., Shure, M. A., Gull, G. E., & Herter, T., 1984, *The electron density in M82 from the SIII mid-infrared line ratio*, *ApJ*, **287**, L11

Huang, Z. P., Thuan, T. X., Chevalier, R. A., Condon, J. J., & Yin, Q. F., 1994, *Compact radio sources in the starburst galaxy M82 and the Sigma-D relation for supernova remnants*, *ApJ*, **424**, 114

Jacoby, G. H., Hunter, D. A., & Christian, C. A., 1984, *A library of stellar spectra*, *ApJS*, **56**, 257

Jansen, R. A., Franx, M., & Fabricant, D., 2001, *[O II] as a tracer of current star formation*, *ApJ*, **551**, 825

Jarrett, T. H., Chester, T., Cutri, R., Schneider, S. E., & Huchra, J. P., 2003, *The 2MASS Large Galaxy Atlas*, *AJ*, **125**, 525

Kaufman, M. J., Wolfire, M. G., Hollenbach, D. J., & Luhman, M. L., 1999, *Far-infrared and submillimeter emission from galatic and extragalactic photodissociation regions*, *ApJ*, **527**, 795

Kennicutt, R. C., 1984, *Struttural properties of giant HII regions in nearby galaxies*, *ApJ*, **287**, 116

Kennicutt, R. C., 1992, *A spectrophotometric atlas of galaxies*, *ApJS*, **79**, 255

Kennicutt, R. C., 1998, *Star formation in galaxies along the Hubble sequence*, *ARA&A*, **36**, 189

Kennicutt, R. C., Tamblyn, P. T., & Congdon, C. W., 1994, *Past and future star formation in disk galaxies*, *ApJ*, **435**, 22

Kewley, L. J., Dopita, M. A., Sutherland, R. S., Heisler, C. A., & Trevena, J., 2001, *Theoretical modeling of starburst galaxies*, *ApJ*, **556**, 121

Kim, D. C., Sanders, D. B., Veilleux, S., Mazzarella, J. M., & Soifer, B. T., 1995, *Optical Spectroscopy of Luminous Infrared Galaxies. I. Nuclear Data*, *ApJS*, **98**, 129

Kinney, A. L., Bohlin, R. C., Calzetti, D., Panagia, N., & Wyse, R. F. G., 1993, *An atlas* *of ultraviolet spectra of star-forming galaxies*, *ApJS*, **86**, 5

Kurucz, R., 1992, *"Finding" the "Missing" solar ultraviolet opacity*, *Rev. Mex. Astron. Astrofis.*, **23**, 181

Kurucz, R., 1993, *Stellar Atmosphere Programs and 2 km/s grid*, Technical report, Smithsonian Astrophysical Observatory, Cambridge, Mass.

Lada, C. J. & Lada, E. A., 2003, *Embedded clusters in molecular clouds*, *ARA&A*, **41**, 57

Lancon, A., Goldader, J. D., & Leitherer, C., 2001, *Multiwavelength study of the starburst galaxy NGC 7714. II. The balance between young, intermediate-age, and old stars*, *ApJ*, **552**, 150

Leitherer, C. & Heckman, T. M., 1995, *Synthetic properties of starburst galaxies*, *ApJS*, **96**, 9

Lejeune, T., Cuisinier, F., & Buser, R., 1998, *A standard stellar library for evolutionary synthesis. II. The M dwarf extension*, *A&AS*, **130**, 65

Lennon, D. J. & Burke, V. M., 1994, *Atomic data from IRON project. II. Effective collision strengths for infrared transitions in carbon-like ions*, *A&AS*, **103**, 273

Lord, S. D., Hollenbach, D. J., Haas, M. R., Rubin, R. H., Colgan, S. W. J., & Erickson, E. F., 1996, *Interstellar Properties of a Dual Nuclear Starburst: Far-Infrared Spectroscopy of M82*, *ApJ*, **465**, 703

Magliocchetti, M., Moscardini, L., Panuzzo, P., Granato, G. L., De Zotti, G., & Danese, L., 2001, *Theoretical predictions on the clustering of SCUBA galaxies and implications for small-scale fluctuations at sub-mm wavelengths*, *MNRAS*, **325**, 1553

Malhotra, S., Kaufman, M. J., Hollenbach, D., Helou, G., Rubin, R. H., Brauher, J., Dale, D., Lu, N. Y., Lord, S., Stacey, G., Contursi, A., Hunter, D. A., & Dinerstein, H., 2001, *Far-infrared spectroscopy of normal galaxies: physical conditions in the interstellar medium*, *ApJ*, **561**, 766

Mayya, Y. D., Bressan, A., Rodríguez, M., Valdes, J. R., & Chavez, M., 2003, *Star formation history and extinction in central kpc of M82-like starbursts*, *ApJ*, , in press

McCarthy, P. J., 1987, *Evidence for large-scale winds from starburst galaxies. I. The nature of the ionized gas in M82 and NGC 253*, *AJ*, **93**, 264

McGaugh, S. S., 1991, *HII region abundances: model oxigen line ratios*, *ApJ*, **380**, 140

McLeod, K. K., Rieke, G. H., Rieke, M. J., & Kelly, D. M., 1993, *M82: the saga continues*, *ApJ*, **412**, 111

Meurer, G. R., Heckman, T. M., & Calzetti, D., 1999, *Dust absorption and the ultraviolet luminosity density at* $z \approx 3$ *as calibrated by local starburst galaxies*, *ApJ*, **521**, 64

Moy, E., Rocca-Volmerange, B., & Fioc, M., 2001, *Evolution of photoionization and star formation in starburst and HII galaxies*, *A&A*, **365**, 347

Nussbaumer, H. & Schmutz, W., 1984, *The hydrogenic 2s-1s two-photon emission*, *A&A*, **138**, 495

O'Connell, R. W., Gallagher, J. S., Hunter, D. A., & Colley, W. N. H., 1995, *Hubble Space Telescope Imaging of Super Star Clusters in M82*, *ApJL*, **446**, L10

O'Connell, R. W. & Mangano, J. J., 1978, *The central regions of M82*, *ApJ*, **221**, 620

Osterbrock, D. E., 1989, *Astrophysics of gaseous nebulae and active galactic nuclei*, University Science Books, Mill Valley, CA

Pauldrach, A. W. A., Hoffmann, T. L., & Lennon, M., 2001, *Radiation-driven winds of hot luminous stars. XIII. A description of NLTE line blocking and blanketing towards realistic models for expanding atmospheres*, *A&A*, **375**, 161

Peng, J. F. & Pradhan, A. K., 1995, *Theoretical diagnostics of ultraviolet and infrared spectral emission from boron-like ions*, *A&AS*, **112**, 151

Perez-Olea, D. E. & Colina, L., 1995, *Evolutionary models of the radio emission in compact starbursts*, *MNRAS*, **227**, 857

Petuchowski, S. J., Bennet, C. L., Haas, M. R., Erickson, E. F., Lord, S. D., Rubin, R. H., Colgan, S. W. J., & Hollenbach, D. J., 1994, *The [N] 205 micron line in M82: the warm ionized medium*, *ApJ*, **427**, L17

Pickles, A. J., 1998, *A stellar spectral flux library: 1150-25000 Å*, *PASP*, **110**, 863

Poggianti, B. M., Bressan, A., & Franceschini, A., 2001, *Star formation and selective dust extinction in luminous starburst galaxies*, *ApJ*, **550**, 195

Poggianti, B. M., Smail, I., Dressler, A., Couch, W. J., Barger, A. J., Butcher, H., Ellis, R. S., & Oemler, A., 1999, *A spectroscopic catalog of 10 distant rich clusters of galaxies*, *ApJ*, **518**, 576

Poggianti, B. M. & Wu, H., 2000, *Optical spectral signatures of dusty starburst galaxies*, *ApJ*, **529**, 157

Portinari, L., Chiosi, C., & Bressan, A., 1998, *Galactic chemical enrichment with new metallicity dependent stellar yields*, *A&A*, **334**, 505

Portinari, L., Sommer-Lancer, J., & Tantalo, R., 2003, *On the Mass-to-Light ratio and the Initial Mass Function in galactic discs*, *MNRAS*, , Submitted, astro-ph/0303190

Rigopoulou, D., Lawrence, A., & Rowan-Robinson, M., 1996, *Multiwavelength energy distributions of ultraluminous IRAS galaxies - I. Submillimetre and X-ray observations*, *MNRAS*, **278**, 1049

Rodighiero, G., Granato, G. L., Franceschini, A., Fasano, G., & Silva, L., 2000, *Spiral and irregular galaxies in the Hubble Deep Field North. Comparison with early types and implications for the global SFR density*, *A&A*, **364**, 571

Rosa-gonzález, D., Terlevich, E., & Terlevich, R., 2002, *An empirical calibration of star formation rate estimators*, *MNRAS*, **332**, 283

Rubin, R. H., Dufour, R. J., Geballe, T. R., Colgan, S. W. J., Harrington, J. P., Lord, S. D., Liao, A. L., & Levine, D. A., 2001, in G. Ferland and D. Wolf (eds.), *Spectroscopic Challenges of Photoionized Plasmas*, Vol. 247, p. 479, Astronomical Society of the Pacific

Rubin, R. H., Simpson, J. P., Lord, S. D., Colgan, S. W. J., Erickson, E. F., & Haas, M. R., 1994, *Nebular properties from Far-Infrared spectroscopy*, *ApJ*, **420**, 772

Sanders, D. B. & Mirabel, J. F., 1996, *Luminous infrared galaxies*, *ARA&A*, **34**, 749

Satyapal, S., Watson, D. M., Pipher, J. L., Forrest, W. J., Coppenbarger, D., Raines, S. N., Libonate, S., Piché, F., Greenhouse, M. A., Smith, H. A., Thompson, K. L., Fischer, J., Woodward, C. E., & Hodge, T., 1995, *High spatial resolution Fabry-Perot imaging of M82: Near-Infrared recombination line observations*, *ApJ*, **448**, 611

Schaerer, D., Contini, T., & Kunth, D., 1999, *Populations of WC and WN stars in*

Wolf-Rayet galaxies, *A&A*, **341**, 399

Schaerer, D., de Koter, A., Schmutz, W., & Maeder, A., 1996, *Combined stellar structure and atmosphere models for massive stars. II. Spectral evolution on the main sequence*, *A&A*, **312**, 475

Schlegel, D. J., Finkbeiner, D. P., & Davis, M., 1998, *Maps of Dust Infrared Emission for Use in Estimation of Reddening and Cosmic Microwave Background Radiation Foregrounds*, *ApJ*, **500**, 525

Schmidt, M., 1959, *The Rate of Star Formation*, *ApJ*, **129**, 243

Schmutz, W., Leitherer, C., & Gruenwald, R., 1992, *Theoretical continuum energy distributions for Wolf-Rayet stars*, *PASP*, **104**, 1164

Silva, L., 1999, *Modelling the SED Evolution of Dusty Galaxies and Applications*, *Ph.D. thesis*, SISSA

Silva, L., Granato, G. L., Bressan, A., & Danese, L., 1998, *Modeling the effects of dust on galactic spectral energy distributions from the ultraviolet to the millimeter band*, *ApJ*, **509**, 103

Soifer, B. T., Boehmer, L., Neugebauer, G., & Sanders, D. B., 1989, *The IRAS bright galaxy sample. IV. complete IRAS observations*, *AJ*, **98**, 766

Soifer, B. T., Cohen, J. G., Matthews, L. A. K., Neugebauer, G., & Oke, J. B., 1995, *Near-infrared and optical spectroscopy of FSC 10214+4724*, *ApJ*, **443**, L65

Soifer, B. T., Sanders, D. B., Neugebauer, G., Danielson, G. E., Lonsdale, C. J., Madore, B. F., & Persson, S. E., 1986, *The luminosity function and space density of the most luminous galaxies in the IRAS survey*, *ApJ*, **303**, L41

Stasińska, G., 1990, *A grid of model HII regions for extragalactic studies*, *A&AS*, **83**, 501

Stasińska, G. & Leitherer, C., 1996, *H II Galaxies versus Photoionization Models for Evolving Starbursts*, *ApJS*, **107**, 661

Stasińska, G., Schaerer, D., & Leitherer, C., 2001, *The evolution of emission lines in HII galaxies*, *A&A*, **370**, 1

Steidel, C. C., Adelberger, K. L., Giavalisco, M., Dickinson, M., & Pettini, M., 1999, *Lyman-break galaxies at* $z \geq 4$ *and the evolution of the ultraviolet luminosity density at high redshift*, *ApJ*, **519**, 1

Storey, G. J. & Hummer, D. G., 1995, *Recombination line intensities for hydrogenic ions IV. Total recombination coefficients and machine-readable tables for Z=1 to 8*, *MNRAS*, **272**, 41

Sullivan, M., Mobasher, B., Chan, B., Cram, L., Ellis, R. S., Treyer, M. A., & Hopkins, A., 2001, *A comparison of indipendent star formation diagnostics for an ultraviolet-selected sample of nearby galaxies*, *ApJ*, **558**, 72

Sullivan, M., Treyer, M. A., Ellis, R. S., Bridges, T. J., Milliard, B., & Donas, J., 2000, *An ultraviolet-selected galaxy redshift survey - II. The physical nature of starformation in an enlarged sample*, *MNRAS*, **312**, 442

Telesco, C. M. & Harper, D. A., 1980, *Galaxies and far-infrared emission*, *ApJ*, **235**, 392

Terlevich, R., Melnick, J., Masegosa, M., Moles, M., & Copetti, M. V., 1991, *A spec-*

trophotometric catalogue of HII galaxies, *A&AS*, **91**, 285

Thornley, M. D., Förster Schreiber, N. M., Lutz, D., Genzel, R., Spoon, H. W. W., & Kunze, D., 2000, *Massive star formation and evolution in starburst galaxies: mid-infrared spectroscopy with the ISO Short Wavelength Spectrometer*, *ApJ*, **539**, 641

Veilleux, S. & Osterbrock, D. E., 1987, *Spectral classification of emission-line galaxies*, *ApJS*, **63**, 295

Verma, A., Lutz, D., Sturm, E., Sternberg, A., Genzel, R., & Vacca, W., 2003, *A mid-infrared spectroscopic survey of starburst galaxies: Excitation and abundances*, *A&A*, **403**, 829

Willner, S. P., Soifer, B. T., Russell, R. W., Joyce, R. R., & Gillet, F. C., 1977, *2 to 8 micron spectrophotometry of M82*, *ApJ*, **217**, L121

Wu, H., Zou, Z. L., Xia, X. Y., & Deng, Z. G., 1998a, *A statistical study of the spectra of very luminous IRAS galaxies. I. Data*, *A&AS*, **127**, 521

Wu, H., Zou, Z. L., Xia, X. Y., & Deng, Z. G., 1998b, *A statistical study of the spectra of very luminous IRAS galaxies. II. Spectral and environmental analysis*, *A&AS*, **132**, 181

Wu, W., Clayton, G. C., Gordon, K. D., Misselt, K. A., Smith, T. L., & Calzetti, D., 2002, *A New Database of Observed Spectral Energy Distributions of Nearby Starburst Galaxies from the Ultraviolet to the Far-Infrared*, *ApJS*, **143**, 377